

# **Light scattering by cometary dust particles with sizes large compared to the wavelength of light**

Dissertation  
zur Erlangung des Doktorgrades  
der Mathematisch-Naturwissenschaftlichen Fakultäten  
der Georg-August-Universität zu Göttingen

vorgelegt von  
**Yevgen Grynko**  
aus Zaporozhye / Ukraine

Göttingen 2005

## **Bibliografische Information Der Deutschen Bibliothek**

Die Deutsche Bibliothek verzeichnet diese Publikation in der Deutschen Nationalbibliografie; detaillierte bibliografische Daten sind im Internet über <http://dnb.ddb.de> abrufbar.

D7

Referent: Prof. Dr. U.R. Christensen

Korreferent: Prof. Dr. K. Jockers

Tag der mündlichen Prüfung: 19.04.2005

Copyright © Copernicus GmbH 2005

ISBN 3-936586-37-3

Copernicus GmbH, Katlenburg-Lindau

Druck: Schaltungsdienst Lange, Berlin

Printed in Germany

# Contents

<b>Summary</b>	<b>5</b>
<b>1 Introduction</b>	<b>7</b>
1.1 Photopolarimetric observations of cometary dust . . . . .	7
1.2 Light scattering by dust-like particles: Theoretical modeling and experiments . . . . .	12
1.2.1 Concepts and terms . . . . .	12
1.2.2 Exact solutions . . . . .	13
1.2.3 Geometric optics approximation . . . . .	16
1.2.4 Experimental study . . . . .	18
1.3 Outline . . . . .	21
<b>2 General study of light scattering by semitransparent particles</b>	<b>23</b>
2.1 Model description . . . . .	23
2.1.1 Method of generation and description of irregular shapes . . . . .	24
2.1.2 Ray tracing . . . . .	26
2.2 Testing the model and comparison with Mie and DDA results . . . . .	29
2.3 Results of modeling . . . . .	33
2.3.1 Faceted spheres . . . . .	34
2.3.2 Binary spheres and faceted ellipsoids . . . . .	39
2.3.3 Perfect and "spoiled" cubes . . . . .	48
2.3.4 RGF particles . . . . .	53
2.3.5 Spectral properties of particles with different shapes . . . . .	60
2.4 Conclusions . . . . .	64
<b>3 SOHO LASCO C3 observations of comets 96P/Machholz 1 and C/2004 F4 Bradfield</b>	<b>67</b>
3.1 The SOHO spacecraft and LASCO C3 telescope . . . . .	67
3.2 Available SOHO data and the orbits of the two comets . . . . .	70
3.2.1 96P/Machholz 1 . . . . .	70
3.2.2 C/2004 F4 Bradfield . . . . .	70
3.3 Data reduction . . . . .	72
3.4 Results and discussion . . . . .	74
3.4.1 Contribution of gas and plasma to our images . . . . .	74
3.4.2 Polarization of comet 96P/Machholz 1 . . . . .	75
3.4.3 Phase function of intensity. 96P/Machholz 1 . . . . .	76

## Contents

---

3.4.4	Phase function of intensity. C/2004 F4 Bradfield . . . . .	81
3.5	Conclusions . . . . .	96
	<b>Outlook</b>	<b>99</b>
	<b>Acknowledgements</b>	<b>111</b>
	<b>Curriculum Vitae</b>	<b>113</b>

# Summary

In this thesis we present the results of observations of cometary dust at large phase angles and general theoretical study of light scattering by the dust particles with sizes large as compared to the wavelength of light.

Our computer model of light scattering by semitransparent particles with arbitrary shape in the geometric optics approximation allows calculations of the scattering angle dependences of all elements of the scattering matrix  $F_{ik}$ . The studies of several classes of shape, including a special class of irregular particles generated with an auxiliary random gaussian field (RGF), at different values of the complex refractive index

showed the following:

- The scattering properties of roughly faceted spheres differ significantly from those of perfectly spherical particles. The optical properties of individual spheres strongly dominate the total scattering by binary touching spheres.
- Highly irregular random gaussian field particles do not show backscattering at all at incoherent scattering. As the degree of non-sphericity grows the maximum of the polarization curve decreases. The RGF particles are able to provide strong depolarization.
- In general, strongly irregular particles of all studied classes reveal qualitative similarity of the scattering angle curves of all scattering matrix elements and much more resemblance in scattering properties, than their perfect representatives.

The analysis of the observational data for comet 96P/Machholz 1 showed that the brightness of the comet increases linearly by almost two orders of magnitude in the range of phase angles  $112^\circ$ - $167^\circ$ . The gradient is independent of wavelength. The forward scattering diffraction spike is absent on the phase curve, therefore the grains mainly contributing to the scattered light must have a size parameter larger than  $x \approx 20$ , i. e. have a radius larger than  $1 \mu\text{m}$ . The best fit refractive index of the data is  $m = 1.2 + i0.004$ . If a particle porosity  $P = 0.5$  is assumed and the mixing rules are applied a complex refractive index of particles  $m = 1.43 + i0.009$  is obtained.

The brightness of comet C/2004 F4 Bradfield was measured in the range of phase angles  $130^\circ$ - $164^\circ.5$ . Analysis of the motion of the dust grains reveals a broad size distribution of the particle sizes with a significant number of sub-micron particles. The discrete dust emissions noticeably influenced the brightness phase curve and made unambiguous interpretation difficult. The gradient of the brightness decrease points to the similarity of the dust of the comet C/2004 F4 to that of 96/P. But theoretical fitting of the phase curve corresponding to the growing phase angle gives the complex refractive index of the dust typical for absorbing silicates or carbonaceous materials.



# 1 Introduction

In this thesis we are interested in photopolarimetric observations of solar radiation scattered by cometary dust and in the theoretical modeling of light scattering by dust particles, necessary for the interpretation of the observational data and understanding of the physics of light scattering. In the introductory chapter we briefly review the general knowledge on the scattering characteristics of cometary dust and the existing theoretical approaches for the solution of the light scattering problem.

## 1.1 Photopolarimetric observations of cometary dust

Measurements of the light scattering by cometary dust indirectly provide information about the composition and physical properties of the dust particles. An obvious way of the characterization of their scattering properties is to consider how the brightness and polarization of the scattered light depend on the geometry of observations determined by the phase angle  $\alpha$ , which is defined as the Sun-comet-Earth angle. Instead of  $\alpha$  the scattering angle  $\theta = \pi - \alpha$  is used sometimes. Another angle specifying the geometry is called solar elongation and is defined as the Earth-Sun-comet angle. The plane defined by the Sun, comet and Earth is called scattering plane.

The only photometric observations of a comet with direct measurements of the dust brightness were made with TKS instrument onboard VEGA-2 (Krasnopolsky et al. 1987). In this experiment the light scattering was measured nearly simultaneously in a wide range of phase angles. The rest of the existing data is obtained from ground-based observations. From Fig. 1.1 one can get a general idea of the phase dependence of brightness of light scattered by comets. In this plot we present the phase functions of 3 comets taken from the data published by Gehrz and Ney (1992). In order to show a pure angular dependence independent of the changing number of particles in the cometary coma the values measured in the visible are normalized by the corresponding values from the infrared, as the thermal radiation has negligible phase dependence. In general the cometary phase curve can be characterized by a small backscattering enhancement, an almost flat and isotropic part at intermediate angles, and a strong forward scattering peak.

At phase angles  $30^\circ \lesssim \alpha \lesssim 90^\circ$  the phase function of brightness is flat, depends only weakly on the particle properties, and does not contain information about their physical characteristics. Observations in the backscattering range  $\alpha \lesssim 30^\circ$  are more interesting as at small phase angles such effects as shadowing and coherent enhancement of intensity can take place, which characterize the size, external and internal structure of particles and can be used as diagnostic tools. The data for several comets published by Meech and Jewitt (1987) give information on the backscattering properties of the cometary dust par-

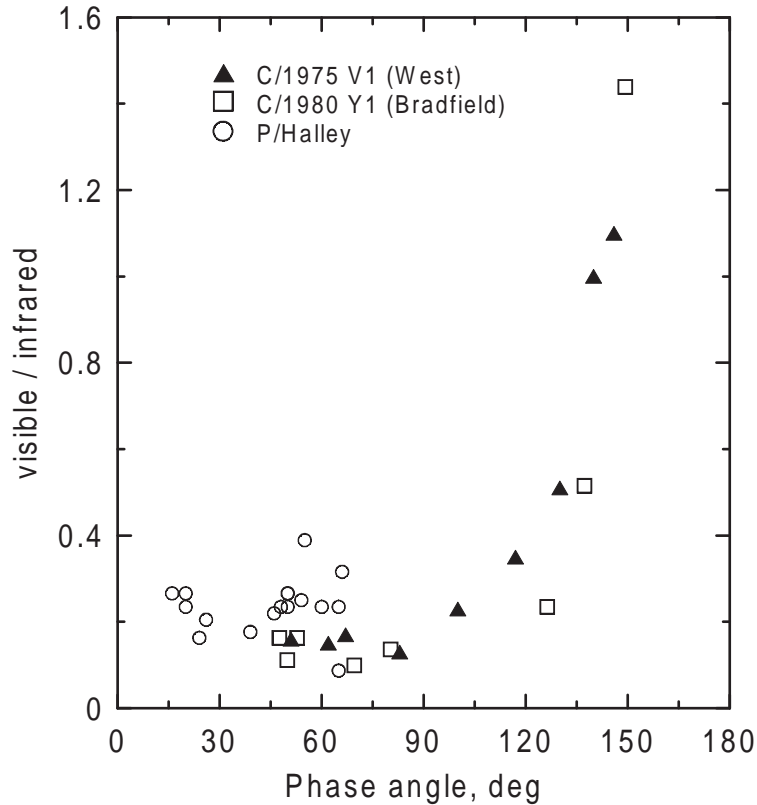


Figure 1.1: Brightness phase functions of 3 comets (Gehrz and Ney 1992).

ticles. At small phase angles the phase curves do not have an opposition surge (Fig. 1.2), typical for many atmosphereless bodies. Some rise of brightness towards  $\alpha = 0^\circ$  with linear phase coefficient  $\beta = 0.02 \pm 0.01$  mag/deg is observed, however. At  $\alpha > 90^\circ$  a forward scattering peak is present. It is sensitive to the complex refractive index and the size of particles. At very large angles the diffraction of light dominates and according to the diffraction theory it is directly connected with the particle sizes. Therefore, the optical properties at forward scattering can also be exploited for diagnostics of the physical properties of cometary dust. Besides, such kind of observational data would be useful for making the theoretical dust scattering models more accurate, as they are built mostly on the basis of observations of dust at small and intermediate phase angles. Unfortunately observations of comets at large phase angles are almost nonexistent. If a comet is seen from the Earth at large  $\alpha$ , most often its solar elongation is very small and observations are impossible. Up to now the largest phase angle at which the brightness of a comet was measured was equal to  $149^\circ$  (comet C/1980 Y1 (Bradfield) = 1980 XV (Gehrz and Ney 1992)). The second comet observed at a similar angle is C/1975 V1 West (Ney and Merrill 1976).

More such observations became possible after the SOHO solar observatory had been placed into orbit. A lot of sungrazing comets from the Kreutz family were observed with LASCO telescopes mounted on SOHO (Biesecker et al. 2002, Sekanina 2002). These comets, however, are not interesting for analysis of their phase functions, because they are observed at very small heliocentric distances and, therefore, can reach large phase angles only at extremely small elongations. Among the periodic comets with known orbits comet

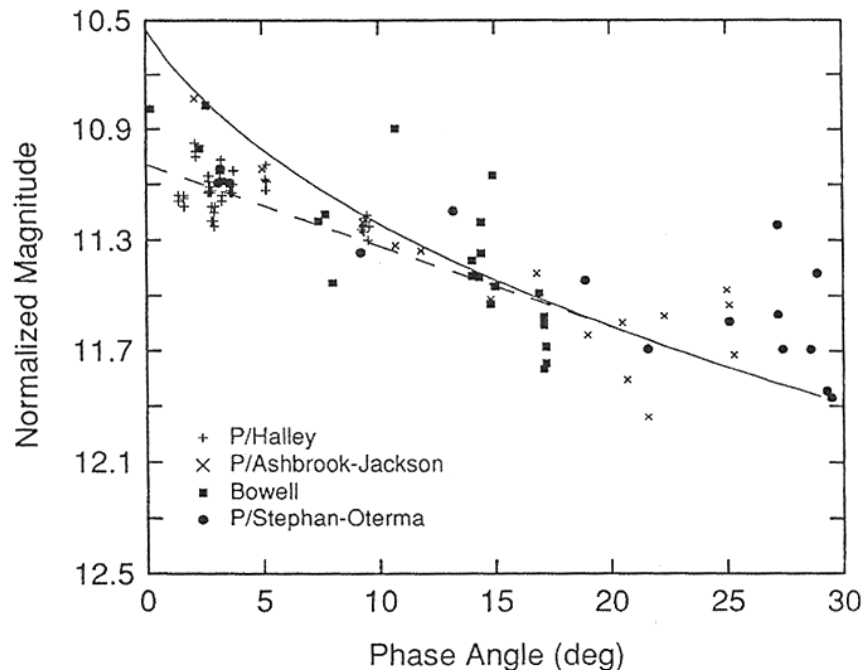


Figure 1.2: Normalized magnitude versus phase angle for four comets (Meech and Jewitt 1987). Solid line represents theoretical fit for a typical dark asteroid. The dashed line indicates a linear coefficient of 0.03 mag/deg.

2P/Encke was observed at small  $\alpha$  (Lamy et al. 2003) and 96P/Machholz 1 (Grynko et al. 2004) and Bradfield C/2004 F4 at large phase angles in the forward scattering regime. The photometric data of the last two ones are presented in this thesis.

The major problem of the determination of the phase functions of cometary dust is the influence of the number of dust particles on the observed brightness. In particular, near perihelion at small heliocentric distances the dust production rate may quickly change. This kind of nucleus activity is difficult to be taken into account. To overcome this problem additional measurements are needed. One can measure the brightness in the visible and infrared range simultaneously. Then, under the assumption that the absorbed energy is isotropically reradiated in the infrared, one can normalize the intensity in visible wavelength range (e.g. Gehrz and Ney (1992)). Another method consists in the normalization of the visible brightness to the gas production rate, as the ratio of the dust to gas production should be approximately constant (see Meech and Jewitt (1987)). But this requires an additional measurement which is not always available.

The degree of linear polarization is a relative quantity and therefore is independent of the dust production rate. It is defined as

$$P = (I_{\perp} - I_{\parallel}) / (I_{\perp} + I_{\parallel}), \quad (1.1)$$

where  $I_{\perp}$  and  $I_{\parallel}$  are the intensity components perpendicular and parallel to the plane of scattering. Thus  $P$  can be either positive, if the electric vector of the electromagnetic wave oscillates predominantly perpendicular to the scattering plane, or negative if it oscillates in that plane.

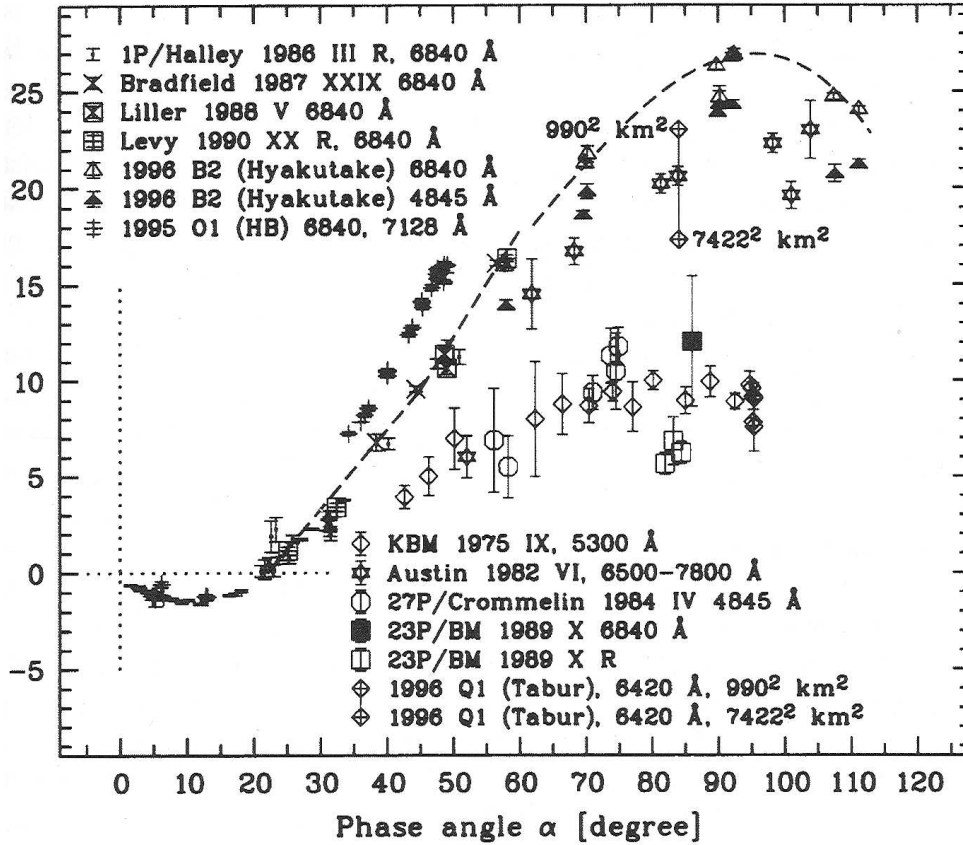


Figure 1.3: Polarization measurements of the Kiselev group (Dushanbe, Kharkov). The dashed line shows the "common" phase curve for the dusty comets.

Fig. 1.3 shows polarization measurements of a number of comets taken from the review of Jockers (1997). A detailed review of the progress and problems in the polarimetry of comets is also presented by Kiselev and Rosenbush (2004). Almost all dust-rich comets show similar phase angle dependences. They include a negative polarization branch at backscattering with minimum polarization  $P_{min} = -1.5\%$  at phase angle  $\alpha_{min} = 10^\circ$  and a positive polarization maximum of  $P_{max} = 25 - 30\%$  at  $\alpha_{max} \approx 95^\circ$ . The polarization inversion angle  $\alpha_{inv}$  is close to  $21^\circ$ .

Cometary polarization measurements suffer from the effect of "gas contamination", which even up to now is not widely acknowledged in the literature. The radiation received from comets is the sum of the light scattered by dust grains and a rich spectrum of lines of the molecules present in the gas coma. As has been discussed in (Chernova et al. 1993, Jockers 1997, Kiselev et al. 2004) even filters with pass-bands centered on spectral regions which are free of major emission lines transmit an amount of molecular emission of low polarization, which is sufficient to significantly affect the measured value of the polarization. It is obvious that the measured polarization is more strongly affected in the so-called gas-rich comets with weak continuum. As the predominantly two-atomic molecules in the cometary coma have always positive polarization the effect of "gas contamination" lowers the positive branch and makes the negative more shallow. Since comets have larger heliocentric distances when they are observed at small phase an-

gles and the dust emission is more predominant at larger heliocentric distances (A'Hearn et al. 1995), the effect of "gas contamination" affects the negative branch of polarization to a lesser extent. It is likely that the large scatter of polarization values at medium phase angles is to a large part caused by the "gas contamination" effect, i.e. at medium phase angles the true polarization of cometary dust does not vary strongly from comet to comet. The negative polarization observed at small phase angles is clearly caused by cometary dust. Note, that the origin of negative polarization of cometary dust and its phase dependence are still not clear, although a lot of theoretical papers concerning the backscattering cometary dust grains have been published in recent years.

The maximum phase angle for existing polarization measurements is smaller than that for the measurements of brightness. For comets C/1989 X1 (Austin) = 1990 V and C/1996 B2 (Hyakutake) (Kiselev and Velichko 1998) the degree of polarization was measured at  $\alpha = 111^\circ$ . Polarization data of comet C/1999 S4 exist at a maximum phase angle of  $121^\circ$  (Kiselev et al. 1998, Hadamcik and Lvasseur-Regourd 2003a), but these data were obtained during the disruption of the nucleus and therefore are not representative. Thus, in order to have a complete idea of the polarization of light scattering by cometary dust, observations at larger phase angles are necessary.

Most of the polarimetric data are obtained by aperture photometry and are related to the integral properties of the entire coma. This limits the possibility of the determination of the intrinsic properties of the dust particles. The results of the imaging polarimetry show that the the degree of polarization of different details in the coma can be different at the same phase angle, which indicates different scattering properties of particles and there evolution in time (Renard et al. 1996, Jockers et al. 1997, Hadamcik and Lvasseur-Regourd 2003a). There is also an evidence of the multiple scattering at distances  $\leq 1000$  km from the nucleus, expressed in the polarization decrease towards the center of the coma. Hadamcik and Lvasseur-Regourd (2003b) observed comet C/1995 O1 (hale-Bopp) over a wide range of the phase angles by the imaging polarimetric method. They presented polarization maps and phase curves of polarization for different regions with minimum phase angle  $\alpha_{min} = 6.9^\circ$ . The parameters of the negative polarization branch appeared to be different if measured for the whole coma or certain parts of the coma. In the jets and central arc of the coma the negative polarization is absent. At the same time the circumnucleus halo produced strong negative branch. Theoretical calculations show that the negative polarization branch is sensitive to the internal structure of scatterers. Therefore these results indicate a difference of the scattering properties of particles and confirms that the observed integral negative branch is a result of the superposition of contributions from particles of different kinds.

Extraction of the physical parameters of particles from the scattering data is an "ill-posed" inverse problem. At present it is not solved and any interpretation of the observations is uncertain. This is because of the two main reasons:

- There is a lack of observational data: from all known comets only a small portion was studied using polarimetry. Observations at large phase angles and imaging polarimetry with high spatial resolution and narrowband filters are needed.

- There is no universal theoretical model of light scattering by cometary dust because of the complexity of the problem and the great variety of properties of natural particles.

In order to adequately interpret the observational data one must conduct exhaustive observations and have an exact idea of the nature of light scattering by an arbitrary scatterer.

Otherwise all existing photopolarimetric observations of comets will remain inefficient from the diagnostic point of view. Thus, it is very important to develop a rigorous model or at least examine the applicability of the existing approaches. In the following section we briefly discuss the theoretical and experimental methods to investigate scattering by dust particles.

## 1.2 Light scattering by dust-like particles: Theoretical modeling and experiments

### 1.2.1 Concepts and terms

Consider the scattering of a monochromatic ( $\exp(-i\omega t)$ ) plane electromagnetic wave

$$\mathbf{E}_0 = \mathbf{e}_0 \exp(i\mathbf{k}_0 \mathbf{r}), \quad |\mathbf{e}_0| = 1, \quad (1.2)$$

by a particle. Because of the linearity of Maxwell's equations, the scattered field  $\mathbf{E}_s$  in the direction  $\mathbf{s} = \mathbf{k}_s/k$  must be always linearly connected with the incident field through the corresponding *amplitude scattering matrix* (Mishchenko et al. 2002)

$$\begin{Bmatrix} E_{s1} \\ E_{s2} \end{Bmatrix} = \frac{\exp(ikr)}{kr} \begin{bmatrix} S_{11} & S_{12} \\ S_{21} & S_{22} \end{bmatrix} \begin{Bmatrix} e_{01} \\ e_{02} \end{Bmatrix}, \quad (1.3)$$

where the indices  $1 = \perp$  and  $2 = \parallel$  designate the components transverse to the planes containing an arbitrary axis  $Z$  and the directions of incidence  $\mathbf{s}_0 = \mathbf{k}_0/k$  or scattering  $\mathbf{s} = \mathbf{k}_s/k$ . Usually the direction of incidence coincides with  $Z$  and the transverse components are defined relatively to the scattering plane ( $\mathbf{s}, \mathbf{s}_0$ ). Note, that different authors (Van de Hulst 1957, Bohren and Huffman 1983, Mishchenko et al. 2002) choose different basis vectors for the transversal field components and normalization in the equation (1.3). As a consequence the elements  $S_{ij}$  can differ. It should be emphasized that the amplitude scattering matrix connects the field components defined in different coordinate systems and, therefore, it is not a tensor.

The amplitude scattering matrix provides a full description of the scattered field. However in real experiments the values proportional to the squares of amplitudes are measured. Therefore for the description of a monochromatic wave a column vector of 4 Stokes parameters is introduced (Van de Hulst 1957, Bohren and Huffman 1983):

$$\mathbf{I} = (I, Q, U, V)^T. \quad (1.4)$$

The parameters are defined through the components of the field  $\mathbf{E}$

$$I = \langle E_{s1} E_{s1}^* + E_{s2} E_{s2}^* \rangle \quad (1.5)$$

$$Q = \langle E_{s1} E_{s1}^* - E_{s2} E_{s2}^* \rangle \quad (1.6)$$

$$U = \langle E_{s1} E_{s2}^* + E_{s2}^* E_{s1} \rangle \quad (1.7)$$

$$V = i \langle E_{s1} E_{s2}^* - E_{s2}^* E_{s1} \rangle \quad (1.8)$$

The values  $I, Q, U, V$  characterize the arbitrarily polarized light beam in terms of the intensity, degree of polarization and parameters of the polarization ellipse. The linear

connection between vectors  $\mathbf{I}_s$  for the scattered field at each scattering angle  $\theta$  and  $\mathbf{I}_0$  for incident field is expressed as

$$\mathbf{I}_s(\theta) = \frac{1}{k^2 r^2} F(\theta) \mathbf{I}_0, \quad (1.9)$$

where  $F$  is a  $4 \times 4$  *scattering (Mueller) matrix*. Its elements can be derived from the elements of the  $2 \times 2$  matrix  $S$  (Van de Hulst 1957, Bohren and Huffman 1983). If particles are oriented randomly they depend on the scattering angle but not on azimuthal angle. Matrix  $F$  also contains full information about scattering properties of the particle, although in practice only some of the parameters of the scattered light (for example, intensity  $F_{11}$  or the degree of linear polarization  $-F_{11}/F_{12}$ ) are measured.

The general definition of the scattering problem is simple and consists in the following. A field  $\mathbf{E}_0$  falls on a particle with volume  $V$ . It excites a field  $\mathbf{E}_i$  inside  $V$ . A field of scattering  $\mathbf{E}_s$  is created outside  $V$ . On the basis of Maxwell's equations one must calculate the full field  $\mathbf{E}$  which equals  $\mathbf{E}_i$  inside  $V$  and  $\mathbf{E}_0 + \mathbf{E}_s$  outside. It also must satisfy the boundary conditions on the surface of the particle and the condition of disappearance of the scattered field at infinity. If the elements of the scattering matrix  $F$  are obtained from observations or experiments, an inverse problem can be solved, since  $F$  is defined by the particle properties. Often this problem turns out to be "ill-posed" and in order to minimize the number of solutions, one must fit the matrix elements at all phase angles and wavelengths.

However, in each specific case the solution of the direct and inverse problems depends on the shape, size and structure of the particle. That is why different methods are developed in the scattering theory, which have domains of applicability and different efficiency at different conditions of the problem. Below we briefly discuss the most common approaches.

### 1.2.2 Exact solutions

There are a lot papers devoted to the problem of light scattering by arbitrary dust-like particles. In all of them, starting from the classical work of Mie (1908), a complicated mathematical apparatus is used. Even for such a simple shape like a sphere the solution cannot be expressed by a simple analytical function of such physical properties of a particle as size and refractive index.

#### Mie theory

Mie theory describes the light scattering by homogeneous spherical particles. If the electric field  $\mathbf{E}$  is assumed to be a time-harmonic, it satisfies the Helmholtz equation (Bohren and Huffman 1983)

$$\nabla^2 \mathbf{E} + k^2 \mathbf{E} = 0. \quad (1.10)$$

It can be solved in spherical coordinates using the separation of variables method, i.e. the electromagnetic wave  $\Psi$  can be expressed in the form

$$\Psi(r, \vartheta, \phi) = R(r)\Theta(\vartheta)\Phi(\phi).$$

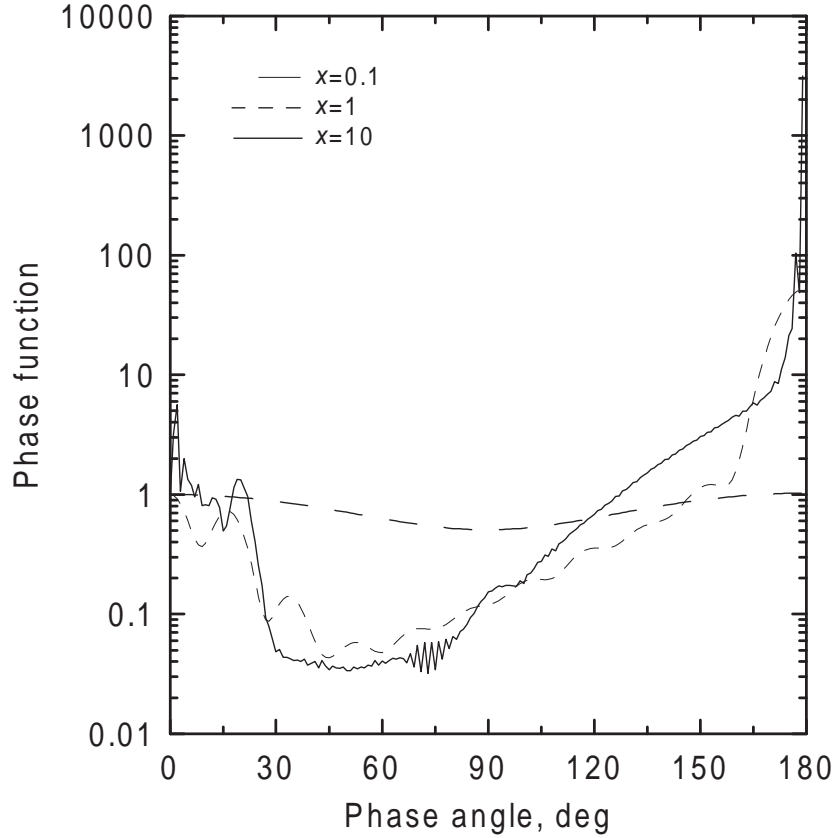


Figure 1.4: Mie phase functions for spheres with complex refractive index  $1.5 + i0.0$  and different size parameters.

The properties of the solution are such that any field that satisfies the scalar wave equation in spherical coordinates may be expanded as an infinite series in vector spherical harmonics (Bohren and Huffman 1983). For example, after additional transformations of these harmonics the amplitude transverse components of the scattered field have the following form

$$\begin{aligned}
 E_{\parallel} &= \sum_{n=1}^{\infty} \frac{2n+1}{n(n+1)} [a_n \pi_n \cos\vartheta + b_n \tau_n \cos\vartheta] \\
 E_{\perp} &= \sum_{n=1}^{\infty} \frac{2n+1}{n(n+1)} [b_n \pi_n \cos\vartheta + a_n \tau_n \cos\vartheta],
 \end{aligned} \tag{1.11}$$

where  $\theta$  is the scattering angle,  $\pi_n$  and  $\tau_n$  are the functions of Legendre polynomials and  $a_n$  and  $b_n$  are related to Bessel and Hankel functions. The theory provides accurate solution for spheres of any size. In practice, however, one has to deal with numerical code and find a compromise between accuracy (the number of terms in the series) and calculation time.

As an example for the angular dependence of scattering by particles, we show in Fig. 1.4 Mie phase functions calculated for spheres with different size parameters. If a particle is much smaller than the wavelength it has a symmetric indicatrix. Larger particles appear to be more forward scattering and at backscattering the glory and rainbow are seen. However, this kind of features is typical for spheroidal shapes only. We note, that scattering at small phase angles is not well understood at present, since rather complicated

wave effects are responsible for this part of the phase function. The forward scattering lobe is followed by a diffraction peak, which depends on the size of a particle. The larger the particle the more narrow and strong this peak is.

Natural dust particles are non-spherical and most of the attempts to apply Mie theory for fitting the observational data were not successful. Only in some special cases the theory can be used to constrain the properties of particles. For example, forward scattering at large phase angles and in the diffraction domain weakly depends on the particle shape and irregular particles can be approximated with equal-volume or equal-projected-area spheres (Grynko et al. 2004). Such an assumption was also used for estimation of thermal emission from cometary dust (see, for example, Mukai (1977), Hanner et al. (1999)), as it provides good accuracy for the absorption efficiency of compact particles.

### Non-spherical particles

If the particle is small compared with the wavelength  $\lambda$  the incident radiation inside and outside of the particle can be studied using the Rayleigh approximation (Rayleigh 1871). It is assumed that

$$x \ll 1, \quad x|m| \ll 1$$

where  $x = 2\pi r/\lambda$  is the size parameter,  $r$  is the radius and  $m = n + ik$  is the complex refractive index of a particle. At such small sizes the electric field inside a particle is constant and in phase with the external field. Hence, a particle can be replaced by a single dipole and the theory of dipole scattering can be applied for solving the problem. An explicit description of this approach can be found in (Van de Hulst 1957) and (Bohren and Huffman 1983).

For non-spherical particles with sizes comparable to the wavelength all approaches can be conventionally divided into two groups: (1) light scattering by non-spherical but regular particles, e.g. by spheroids; (2) light scattering by particles with shapes randomly deviating from sphere.

Analytical solutions in the form of series were obtained only for homogeneous cylinders (Wait 1955) and prolate and oblate spheroids (Asano and Saito 1980, Voshchinnikov 1996). Other shapes require application of different kinds of numerical methods.

One of the general approaches is an approximation of non-spherical particles by clusters of spheres. At first, Bruning and Lo (1971) presented a solution of the scattering problem for two touching spheres. Mackowski (1991) generalized this method for the case of an arbitrary number of spheres. The field scattered by a such system is represented as a superposition of the fields scattered by individual spheres. The field scattered by each individual sphere is determined by means of Mie theory under the assumption that the exciting field is formed by the initial incident field and the fields scattered by the other spheres. This gives some technical difficulties. The solution of Mie theory for individual spheres must be presented in a spherical coordinate system. In order to take into account the interaction between spheres it is necessary to transform the field scattered by one sphere into the coordinate system of the other sphere. This requires a lot of additional calculations and their number grows with the number of monomers. Moreover, it turns out that spheres reveal their individual scattering properties even if grouped in a cluster (Zubko et al. 2004). One should take this into account when applying this method in practice. As applied to the cometary dust the collective effects in systems of spheres were studied,

for example, in (Xing and Hanner 1997, Petrova et al. 2000). Kimura et al. (2003) showed, that all common characteristics in the phase angle and wavelength dependences of intensity (including albedo) and polarization of cometary dust can be reproduced by aggregates, consisting of optically dark submicron spheres.

Discrete Dipole Approximation (DDA) allows consideration of particles with arbitrary shape and structure. It was introduced in the scattering theory by Purcell and Pennypacker (1973), although its physical fundamentals were known and used before (Born and Wolf 1964). The main physical approximation lies in the replacement of the real scatterer by a system of discrete elements with volume  $V_i$ , polarizability  $\alpha_i$  and dipole moments  $\mathbf{d}_i = \mathbf{d}(\mathbf{r}_i)$ ,  $i = 1 - N$ . The rest of calculations such as determination of the amplitudes of dipoles or the scattering matrix can be performed rigorously. After the matrix of discrete elements is generated, the system of  $N$  linear equations describing the  $N$  fields that excite each dipole is solved numerically. The disadvantage of this method is that sizes larger than the wavelength of light require a large number of dipoles in the approximation and, hence, a large number of equations. This leads to the increase of the calculation time and the requirements of large memory. Moreover, in such critical conditions the solution becomes unstable. The maximum size parameter for which the problem can be solved in reasonable time is  $x \approx 30$ . Thanks to the increase of performance of modern computers in recent years DDA has been applied for the calculation of scattering by particles comparable and slightly larger than the wavelength, by porous clusters (Lumme and Rahola 1994, Kimura and Mann 2004, Zubko et al. 2004) and compact irregular particles (Yanamandra-Fisher and Hanner 1999, Zubko and Shkuratov 2001).

Another important method is the T-matrix method. It is popular at present, because fast public-domain codes exist and in such calculations the maximum size limit of a scatterer may exceed  $x = 100$ . The method was known before in quantum theory. Waterman (1971) introduced it in the field of electromagnetic scattering. In this method the incident and scattered fields are expanded into vector spherical harmonics outside of a sphere circumscribing a non-spherical particle. The detailed theoretical background of the method and the description of the analytical orientation-averaging procedure is given in Mishchenko et al. (2002). A great advantage of the T-matrix formulation is that the corresponding T-matrix, depending only on the physical properties of the scatterer, is determined only once. Then it can be used for calculations at any geometry of illumination and observation and for any polarization of the incident light. In principle, the method can be applied to any shape of scatterer, provided its surface is single-valued if represented in spherical coordinates. However the calculations become very complicated if the particle has no rotational symmetry. Therefore in real applications the T-matrix method is used most often for spheroids or clusters of spheres, circular cylinders and rotationally symmetric shapes with polynomial generatrix (Mishchenko et al. 2002). Certainly, it is a strong simplification of the problem, as cometary dust particles have random irregular shape. Petrova et al. (2000) used the T-matrix method for a systematic comparison of observations of cometary dust grains with theoretical studies of aggregates consisting of spheres. In this paper the parameters of the aggregates, needed to reproduce the phase dependence of polarization of cometary dust, were determined. In (Petrova and Jockers 2002) the spectral dependence of polarization was studied. It was shown that an aggregate model correctly describes the observed positive polarimetric color (polarization degree increases with the wavelength). It should be emphasized, however, that aggregates larger

than the wavelength cannot be studied with the presently available codes.

### 1.2.3 Geometric optics approximation

The sizes of particles in natural media can be much larger than the wavelength of incident light. Aerosol components of planetary atmospheres can contain large particles of irregular as well as regular (e.g., transparent ice crystals) shape (Liou 1980). Dust cometary comae (Festou et al. 1994) and the interplanetary dust cloud (zodiacal light) (Schiffer and Thielheim 1982) probably contain a considerable number of large irregular particles.

The methods described above cannot be applied to study the optical properties of large particles. Analytical solutions developed for regular non-spherical shapes are expansions of the parameter  $r/\lambda$ . Thus it is necessary to account for a lot of complex terms in such general solutions for large values of  $r/\lambda$ , which can be realized for spheres only. Such a simple shape as an ellipsoid is already too exacting for modern computers. Numerical techniques, providing exact solutions, also have size limitations.

The only computational method applicable for large particles of any size is the geometric optics (GO) approximation. The basis of this approach is very simple. It is assumed that the energy incident on a particle is split into reflected and refracted components according to Fresnel's equations. They are valid only for size parameters  $x \gg 1$ . The curvature radii of the particle surface also must be large enough. The diffraction component of intensity can be added to the GO solution separately.

However, even with such simplifications the problem remains to be complex enough. There were several attempts of analytical studies of multiple scattering inside large semi-transparent particles with irregular shape, but they all were shown to be inexact. Using shadowing theory, Schiffer and Thielheim (1982) developed simplified analytical forms for some components of scattering: single external reflection, multiple scattering from a rough surface and light transmitted by a particle. Mukai et al. (1982) assumed large absorbing spherical particle with rough surface. Using 1-d radiative transfer theory, they considered multiple scattering by a surface and integrated the result over the sphere.

Computer modeling based on the ray tracing turns out to be the simplest way to study light scattering in the GO approximation. Ray tracing was used for the first time by Descartes in 17th century to understand the formation of the primary and secondary rainbows. A typical ray tracing computer algorithm begins by defining a particle or a spatial arrangement of particles in the computer memory. The particle sizes, shapes, optical constants, and their spatial orientations are given. Then the system is "illuminated" with a large number of rays. These rays are multiply reflected and refracted on their way. Besides, they can be partly absorbed within the particle, if it is semitransparent. Each ray is traced from the first to the last interaction with the particle surface. The interaction is described by means of Fresnel's and Snell's laws, though, in principle, more complicated scattering phenomena, like diffraction on particle facets can also be taken into account. The ray tracing extinction cross-section of the particle is equal to its geometric cross-section  $C_{ext}^{RT} = S$ . Hence, the ray tracing scattering cross-section is equal to  $C_{sca}^{RT} = \omega^{RT} S$ , where  $\omega^{RT}$  is the ray tracing single scattering albedo. What regards diffraction, its extinction cross-section is always equal to the diffraction scattering cross-section  $C_{ext}^D = C_{sca}^D$ . Besides, for isolated particle the diffraction extinction cross-section is equal to the geometric cross-section  $C_{ext}^D = S$ . The diffraction phase function for par-

ticles much larger than the wavelength is given by the following formula (Van de Hulst 1957)

$$\begin{cases} p^D(\theta) = 4x^2 \left( \frac{J_1(x\sin\theta)}{x\sin\theta} \right)^2, & \theta \in [0^\circ, 90^\circ], \quad x \rightarrow \infty \\ p^D(\theta) = 0, & \theta \in [90^\circ, 180^\circ], \end{cases} \quad (1.12)$$

where  $J_1$  is the Bessel function of the first kind and  $x$  is the size parameter. Thus, if  $p^{RT}$  is the ray tracing phase function, the total optical phase function is given by the following formula (Macke et al. 1996b)

$$p(\theta) = \frac{C_{sca}^{RT} p^{RT}(\theta) + C_{sca}^D p^D(\theta)}{C_{sca}^{RT} + C_{sca}^D} = \frac{\omega^{RT} p^{RT}(\theta) + p^D(\theta)}{\omega^{RT} + 1} \quad (1.13)$$

Note, that for large particles the diffraction is important only in the small-angle region ( $\theta \leq \lambda/r$ ).

The great advantage of the GO approximation is that it practically has no limitations on the particle shape. However its range of applicability is limited by the smallest size parameter  $x_{min}$  and requirements to the curvature radii of the surface. This point is considered in section 2.2 in more detail.

The first computer modeling results for the scattering indicatrix of regular crystals were obtained by Jacobowitz (1971), Wendling et al. (1979), Cai and Liou (1982), Liou et al. (1983a), Liou et al. (1983b), Takano and Jayaweera (1985), Whalley and McLaurin (1984), Muinonen et al. (1989). Computer simulations of scattering by particles with irregular shapes have been carried out in (Peltoniemi et al. 1989, Muinonen 2000, Grundy et al. 2000, Grynko et al. 2001a, Grynko and Shkuratov 2002, 2003). In present time investigations of light scattering in the geometric optics approximation by means of computer modeling are actively developed not only for studying of individual particle properties, but also for the simulation of the scattering characteristics of aggregate particles (Muinonen et al. 2001, Stankevich et al. 2003) and particulate surfaces (Shkuratov and Grynko 2005).

In (Macke et al. 1996a, Mishchenko and Macke 1997) large particles with multiple randomly positioned inclusions were considered. In these models the inclusions scatter light isotropically or according to Mie theory, while rays are traced in the usual way. Yang and Liou (1995, 1996) developed a hybrid method for scattering by hexagonal ice crystals, incorporating wave interference in the GO. Their model uses the ray tracing technique to solve the near field on the particle surface. For the traced rays their phases are kept and the phase interference of different trajectories is taken into account. The near field is transformed then to the far field on the basis of the electromagnetic equivalence theorem. The method gives good agreement with exact solution (finite-difference time domain method) for phase function at size parameters larger than  $\approx 20$ , although it is very time consuming and was realized so far only for simple regular shapes.

Geometric optics was also applied to fit experimental measurements of the scattering matrix for some dust samples. In (Volten et al. 2001) scattering angle dependences of non-zero scattering matrix elements of mineral aerosol samples (red clay, quartz, volcanic ash) were fitted with curves calculated in the GO approximation using Gaussian random shapes. Nousiainen et al. (2003) also used the model of Gaussian shapes to fit the experimental data for Saharan dust particles. It was found that the traditional ray tracing provides good fits only if unrealistically spiky shapes are used. To improve the agreement

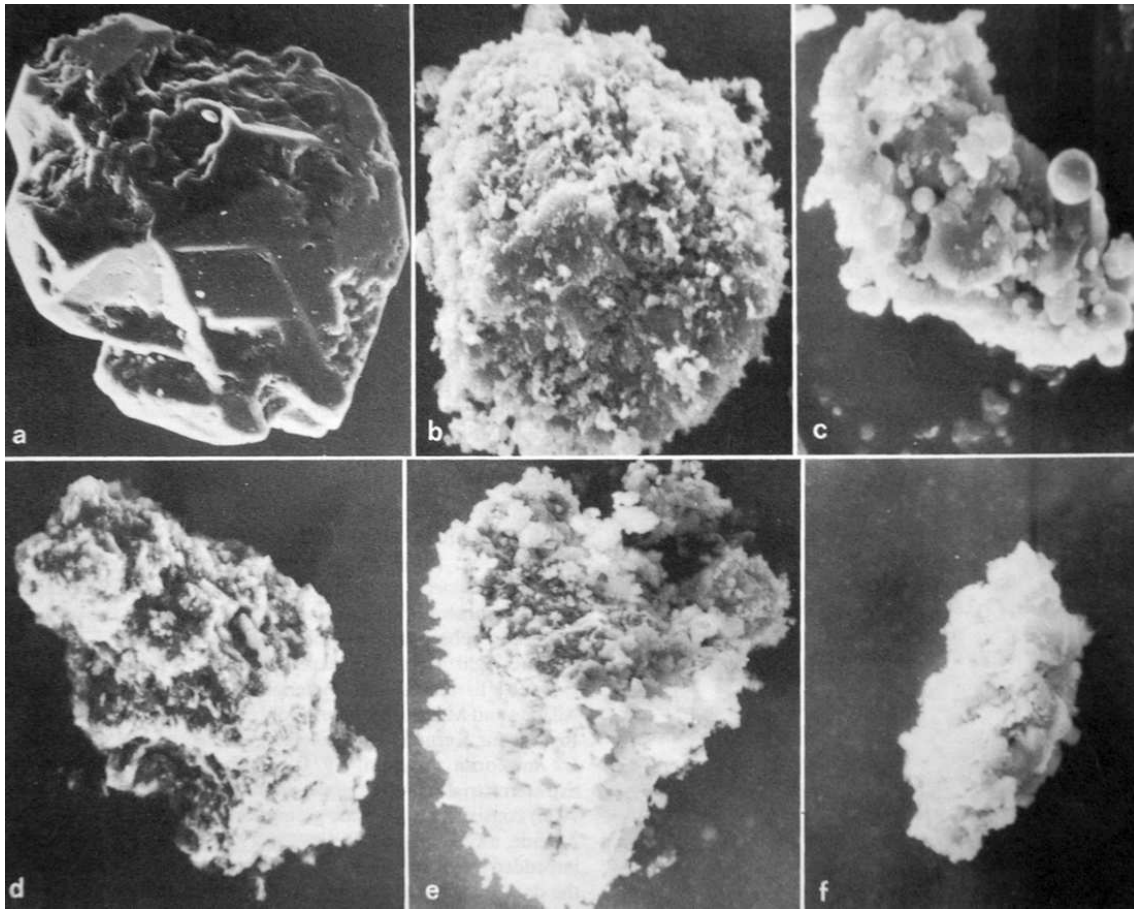


Figure 1.5: SEM photographs of the scattering particles measured in the experiments of Weiss-Wrana (1983): quartz (a), activated charcoal (b), fly-ash (c), meteorite Murchison (d), meteorite Allende matrix (e), meteorite Allende inclusion (f).

for realistic shapes the authors incorporated internal inhomogeneity and the small-scale surface roughness of particles, introducing so called Lambertian surface elements and internal screens. Bonev et al. (2002) used the ray tracing code of Macke et al. (1996b) to interpret the color of the dust of comet C/1994 S4. In this paper a broad distribution of the particle sizes was assumed and for large and small particles GO approximation and T-matrix method were applied, respectively.

#### 1.2.4 Experimental study

Natural dust particles have a great variety of shapes and structures, which often cannot be adequately simulated with theoretical models. For particles much larger than the wavelength only approximate models exist. Thus laboratory experiments are an important way to investigate the light scattering problem.

One of the first extensive experiments on the light scattering by interplanetary dust analogs was made by Weiss-Wrana (1983). In order to deal with isolated particles in the experimental setup electrostatic levitation of single particles was used. The dependence of intensity and polarization on scattering angle was measured for opaque and transparent

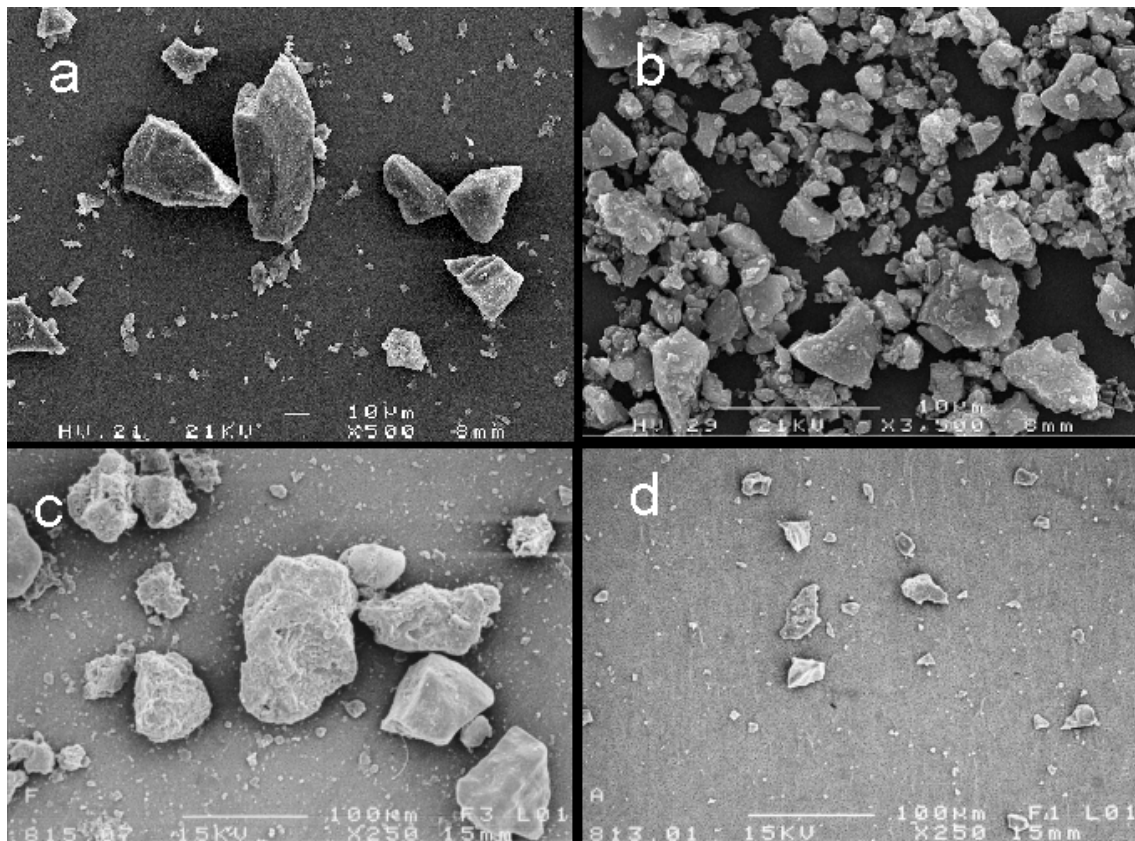


Figure 1.6: Some samples of particles measured in the light scattering experiments of the Amsterdam group: olivine L (a), meteorite Allende (b), Saharan dust sand (c), quartz (d) (<http://www.astro.uva.nl/scatter/>).

particles of terrestrial and meteoritic origin (Fig. 1.5). Their size parameters were of the order of several hundred in order to reproduce the assumed size of interplanetary dust grains. It was shown, that at intermediate and large scattering angles the measured intensity curve differs significantly from Mie theory. The scattering properties of the zodiacal light can be reproduced by opaque irregular particles with the sizes of 20-120  $\mu\text{m}$ .

The Amsterdam group has measured the phase dependence of all non-zero scattering matrix elements for a large number of irregular transparent terrestrial and meteoritic powder samples (Fig. 1.6) (Volten et al. 2001, Muñoz et al. 2000, 2001, 2002). The detailed description of the experimental setup, problems and perspectives of such experiments are discussed by Hovenier et al. (2003). To measure scattering by isolated particles during the experiment they are located in a jet stream produced by a special aerosol generator. The different samples had broad size distributions with the peak effective radii between 0.8 and 8  $\mu\text{m}$  and the wavelength of the laser light source was 635.8 nm and 441.6 nm. It was shown that feldspar and clay particles well reproduce the phase dependence of polarization of cometary dust, in particular the value and location of the positive polarization maximum. In the backscattering region a negative polarization branch produced by isolated compact particles was also discovered. This feature was known before only for powder surfaces and clusters of compact grains and was interpreted as a result of the co-

herent multiple scattering in the media consisting of such particles. All the results of these experiments and detailed description of the samples are available in the Light Scattering Database at <http://www.astro.uva.nl/scatter/>.

Recently Rossi et al. (2004) published experimental measurements of the phase functions of large absorbing carbon and ash samples for which GO is applicable. In their experiments single particles were measured with an electrodynamic levitator and ensembles with a particle feeder. However, the authors concentrate mostly on the description of the experimental device.

Note that laboratory experiments have an important disadvantage. It is very difficult to reach small phase angles and study the regime of backscattering. This is important for the understanding of coherent scattering effects and interpretation of the observational data, since cometary dust is observed sometimes near opposition. The distances between the sample and the light source and the detector that are possible in a laboratory do not allow the arrangement of the the light source and the detector for very small phase angles. The devices must have small apertures and the resulting small light fluxes make the measurements more laborious.

## 1.3 Outline

In theoretical light scattering simulations non-spherical but regular shapes of particles are applied to model the scattering properties of natural irregular particles (Figs. 1.5, 1.6). Bi-spheres, clusters of spheres, spheroids, simple polyhedrons are used most often, since really random shapes are difficult to model. In this situation one should understand when these shapes are applicable and when more rigorous modeling is necessary. For large particle sizes this can be checked only in the geometric optics approximation, which has never been done before. We examine this in chapter 2. We use our computer ray tracing model, which allows calculation of the full scattering matrix for arbitrarily shaped particles. We also present a new method of generation and description of random irregular shapes. We compare scattering matrix elements of regular and irregular particles of different classes of shape and study the change of the scattering properties of regular particles when they are slightly deformed. The proposed model can be used for many applications in astrophysics and geosciences. The model can be considered as a basis on which special cases such as propagation anisotropy inside particles, internal inhomogeneity and inclusions as well as small-scale surface roughness can be studied.

In Chapter 3 we present the LASCO C3 observations of comets 96P/Machholz 1 and Bradfield C/2004 F4. We determine for these comets their brightness and polarization at large phase angles. From their scattering phase functions and dynamics of the dust particles we find constraints for the dust physical properties such as composition and size. To fit the phase curves at the observed phase angles we use Mie theory and the ray tracing technique for large random irregular particles developed in chapter 2.



## 2 General study of light scattering by semitransparent particles with arbitrary shape in the geometric optics approximation

In this chapter we present a new computer model of light scattering by semitransparent particles with arbitrary shape. It allows calculations of albedo and angular dependences of all elements of the scattering matrix  $F_{ik}$  in geometric optics approximation (GO). By means of the model we study in detail the role of the particle shape (five classes of shape are presented) and optical constants in their scattering properties. We also consider the limits of applicability of the ray tracing method.

### 2.1 Model description

Our computer modeling is based on Monte Carlo ray tracing. The main idea used is simple: a particle is generated in the computer memory, then, it is "illuminated" with great enough number of rays. These rays are multiply reflected and refracted on their way. Besides, they can be partly absorbed within the particle, if it is semitransparent. Each ray is traced from the first to last interaction with the particle surface. The interaction is described by means of the Fresnel and Snell's laws.

Generation and quantitative description of arbitrary shaped particles is one of the most important problems in the computer modeling. There are many classes of random shapes. For instance, this can be a sphere "spoiled" with random fluctuations of its radius, or a prism with random lengths of the diagonals, or a roughly faceted ellipsoid, or a particle with a very irregular shape close to an aggregate of a few glued particles, and so on. There is also a class of particles with a regular shape in average, but with the surface complicated by small-scaled ripples defined by a random function. Different random shape classes may show different optical properties. That is why choosing the model for particles in each specific problem, one should be guided by a priori data or, at least, by estimates of the shape class of investigated particles.

Here we study five classes of randomly shaped particles. Examples of such particles are presented in Fig 2.1. The first class is presented with faceted spheres that have a different number of flat facets,  $N$ , which varies in our studies from 100 to 30000. The second class comprises binary faceted spheres (contacting components). The third class is formed by faceted ellipsoids, for which the ratio of their axes varies as well as the value

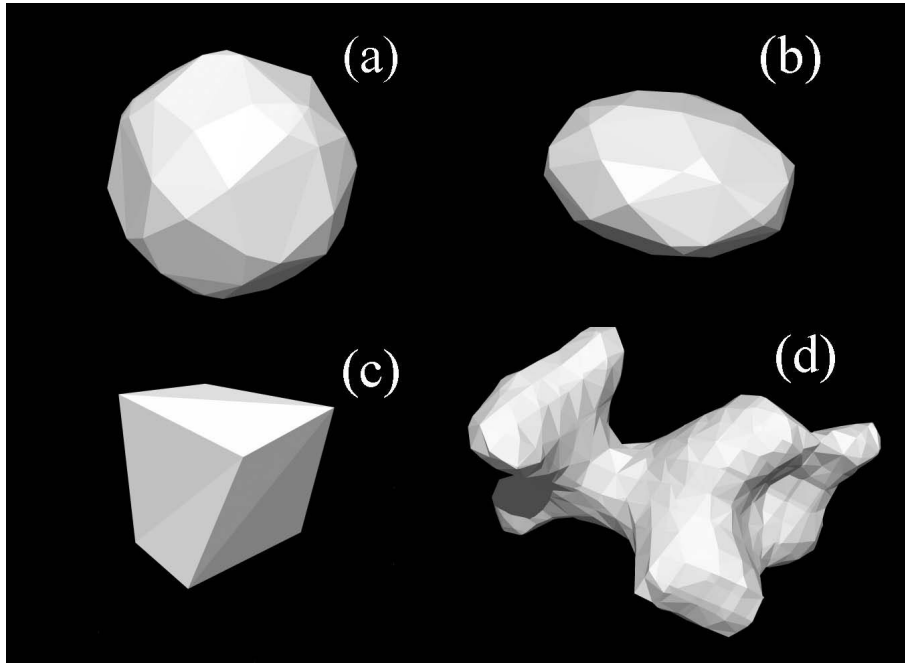


Figure 2.1: Examples of randomly shaped particles used for calculations of scattering matrices. Roughly faceted sphere (a) and ellipsoid (b), irregular cube (c) and irregular RGF particle (d).

*N*. The fourth class consists of cubes of "spoiled" forms, when the length of cube sides slightly varies. And, finally, randomly shaped particles generated by an auxiliary random gaussian field (RGF) form the fifth class .

### 2.1.1 Method of generation and description of irregular shapes

In case of quasi-regular particles, which are close to spheres, ellipsoids, and cubes, the particles can be described analytically and then approximated by a different number of triangular facets. For RGF particles the generating technique is more complicated. We describe this technique below.

At first, a 3-D random field  $h(x, y, z)$  with certain properties, which are characterized by the probability distribution  $W(h)$  and the correlation function  $q(\Delta x, \Delta y, \Delta z)$  is generated in the computer memory. We use Gaussian statistics to generate a field that can be characterized with the following probability density function

$$W = \lim_{m \rightarrow \infty} \frac{1}{\sigma^m \sqrt{2^m \pi^m D}} \exp \left( -\frac{1}{2D\sigma^2} \sum_{k,j=1}^m D_{k,j} h_k h_j \right) \quad (2.1)$$

and the correlation function

$$d_{i,k} = q(l_{i,k}) = \exp(-l_{i,k}^2/l_0^2), \quad (2.2)$$

where  $\sigma$  is the dispersion of values  $h(x, y, z)$ ,  $D$  is the determinant of the covariance matrix of the heights at  $m$  locations,  $d_{i,k}$  is the element of covariance matrix,  $D_{k,j}$  is the signed minor and  $l_{i,k}$  is the distance between the points  $i$  and  $k$ , and  $l_0$  is the correlation radius.

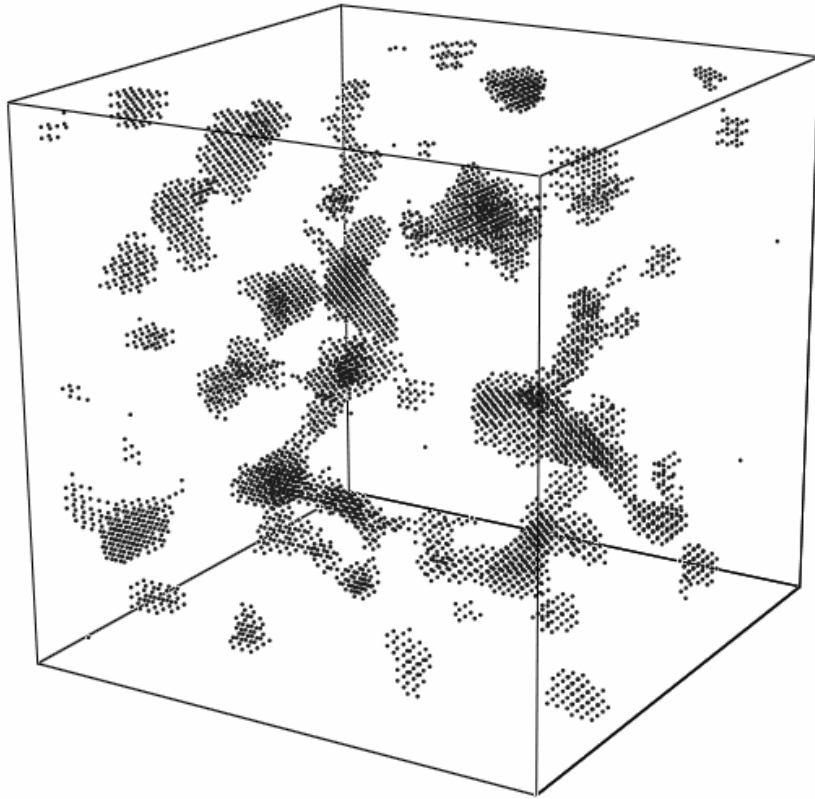


Figure 2.2: A sample of 3-d discrete volume filled with particles.

Such a random field can be considered as a 4-D single-valued relief with the gaussian statistics of hights, correspondingly. Then, this relief is dissected by a 3-D hyperplane at a certain level that is parallel to the relief average plane. It means that the values of the field in every point of the space  $(x, y, z)$  are compared with a constant  $C$ . It is regarded that, if  $h(x, y, z) > C$ , there is substance of a particle in the point  $(x, y, z)$  and emptiness in opposite case. The altitude of the level over the average plane influences the shape of particles and can be considered as an independent parameter. Finally, after such a procedure a 3-D medium is formed, consisting of particles with random shape and different sizes (see Fig. 2.2). Thus we have in the computer memory a realization of a finite volume filled with RGF particles. One can consider the particles as independent realizations of one RGF particle and determine its average scattering matrix elements. The surface of particles is presented by a succession of triangular facets, for which the laws of reflection and refraction and the Fresnel formulas are applicable (Fig. 2.1).

Previously this idea was suggested for the case of 3-D single valued stochastic surface in Shkuratov and Stankevich (1992), Peltoniemi (1993), Shkuratov (1994) and has been implemented, e.g., in Stankevich et al. (2002) to study the shadow-hiding effect in media consisting of randomly shaped particles. The above technique has also been applied to generate surfaces with a random multiple-valued relief (Grynko et al. 2001b). Here we apply this to study individual particles.

To characterize random particles generated as described above we investigated their

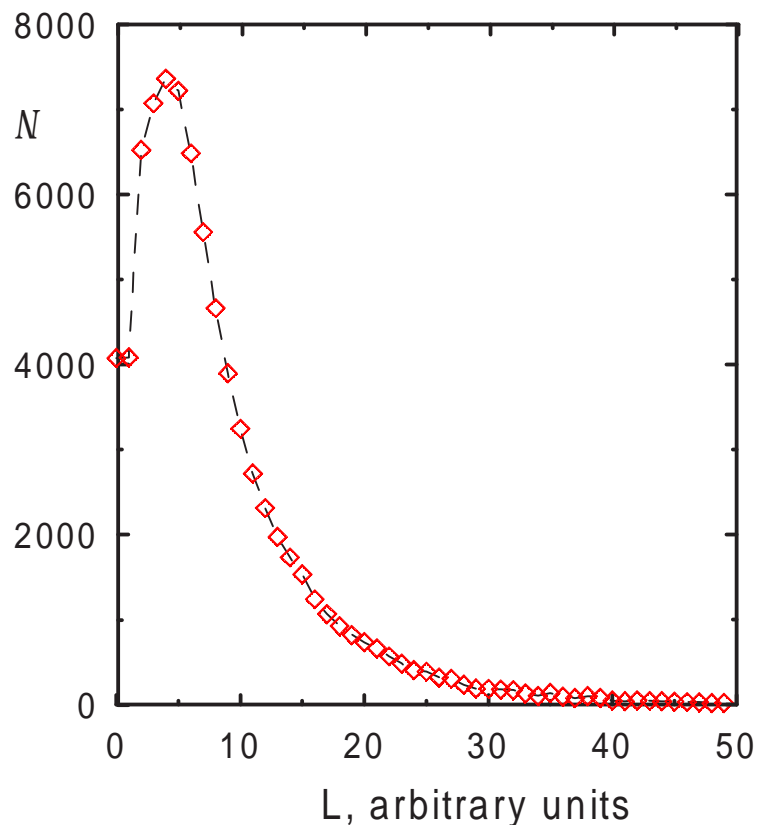


Figure 2.3: Size distribution of particles generated by means of the random gaussian field.

statistical properties, e.g., the size distribution and the deviation of their irregular shape from a spherical one. The maximal elongation has been chosen as a parameter of particle size. Distribution of size follows approximately Poisson's law (Fig. 2.3). To describe the deviation of particles from a sphere we use the characteristic variation of local slopes. To determine this parameter we find the center of a particle, then, put a vector from the center to each facet and calculate the angle between this vector and the normal to the facet. The angle  $\beta$  (it can be called also deviation angle) averaged over all facets of the particle is directly related to the particle shape: it is equal to zero in the case of a spherical particle and approaches to  $90^\circ$  for a complicated shape.

In Fig. 2.4 the distribution of the deviation angle is presented. One can conventionally divide all generated particles into 3 types of shape: spheroidal ( $\beta < 25^\circ$ ), irregular "compact" ( $25^\circ < \beta < 70^\circ$ ) and "fluffy" ( $\beta > 70^\circ$ ). Fig. 2.5 shows samples of each type.

### 2.1.2 Ray tracing

As we deal with a set of small facets constituting the surface of a particle, the procedure of light scattering by a particle consists of: (1) a sequence of reflections and refractions on facets, and (2) light absorption within the particle. The complex refractive index of particles is designated by  $m = n + ik$ , where  $n$  and  $k$  are the real and imaginary parts of  $m$ . The refractive index of the surrounding medium, which is considered as non-absorbing, is taken to be unity. We also assume the imaginary part of the refractive index of particles

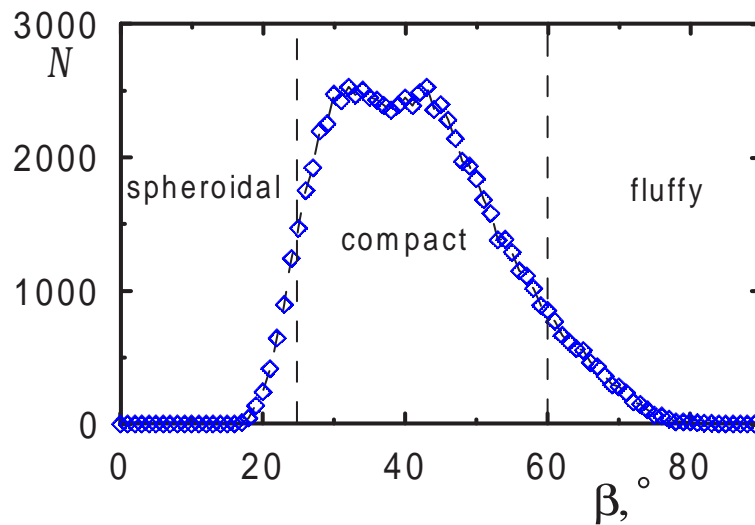


Figure 2.4: Shape distribution over parameter  $\beta$  of particles generated by means of the random gaussian field. Vertical lines show conventional division of particles into 3 types of shape

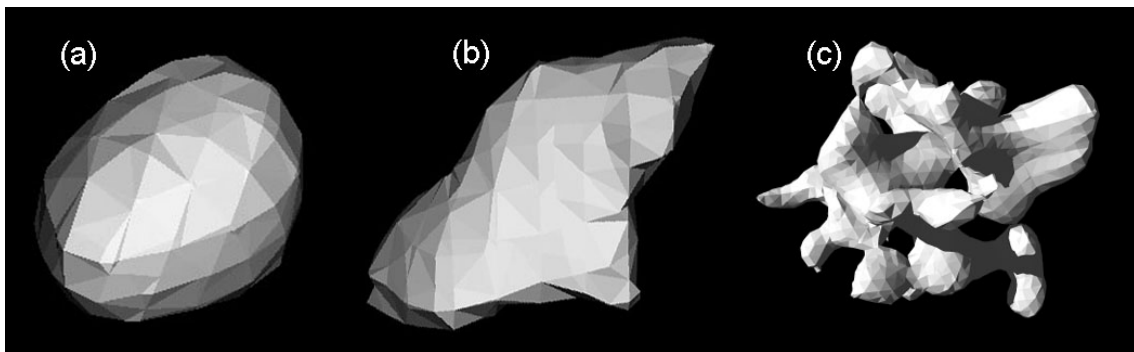


Figure 2.5: Samples of RGF particles of three types of shape: spheroidal (a), irregular "compact" (b) and "fluffy" (c).

to be very small and to have negligible influence on reflection and refraction. Thus the value  $k$  can affect results only through absorption, described by  $\exp(-4\pi lk/\lambda)$ , where  $l$  is the distance traveled by the ray of wavelength  $\lambda$  in the particle.

The second stage of the computer experiment is a Monte Carlo ray tracing. Let us consider it in more detail. A particle is placed at the origin of a coordinate system and is then "illuminated" with a beam of parallel rays propagating in the direction of the axis  $Z$ . The rays are launched from random points uniformly distributed within an area in a plane parallel to the  $XY$  plane with size corresponding to the maximal projection of particles on the plane.

The interaction of a ray with the particle surface results in two new rays: a transmitted and a reflected one. The sum of their intensities is equal to the intensity of the initial ray. The Fresnel formulas give the intensity of each of these rays and Snell's law provides their propagation directions. Splitting rays every time they meet the particle surface would be ineffective, since their number increases in geometrical progression with scattering order.

Therefore we used a more effective technique. We randomly choose between the two possibilities (to be refracted or reflected) and use only one of them, treating intensities as the corresponding choice probability. Similarly, instead of attenuating the ray intensity, when the absorption coefficient  $k$  of the particle is non-zero, the probability of absorption is calculated for a given ray path-length  $l$ . Then we use a random-number generator and make a decision whether the ray has been absorbed. The Stokes parameters of the reflected and refracted rays in the correspondent coordinate system can be obtained from

$$I_r = R \cdot K \cdot I_i, \quad (2.3)$$

$$I_t = T \cdot K \cdot I_i, \quad (2.4)$$

where  $I_i$  is the Stokes vector of the incident ray,  $K$  is the matrix of rotation to the plain of incidence, and  $R$  and  $T$  are Fresnel's reflection and refraction matrices, respectively. In explicit form (Bohren and Huffman 1983)

$$K = \begin{pmatrix} 1 & 0 & 0 & 0 \\ 0 & \cos 2\omega & \sin 2\omega & 0 \\ 0 & -\sin 2\omega & \cos 2\omega & 0 \\ 0 & 0 & 0 & 1 \end{pmatrix}, \quad (2.5)$$

where  $\omega$  is the rotation angle of the scattering plane for transition from one facet to the other and

$$R = \frac{1}{2} \begin{pmatrix} r_{\parallel}r_{\parallel}^* + r_{\perp}r_{\perp}^* & r_{\parallel}r_{\parallel}^* - r_{\perp}r_{\perp}^* & 0 & 0 \\ r_{\parallel}r_{\parallel}^* - r_{\perp}r_{\perp}^* & r_{\parallel}r_{\parallel}^* + r_{\perp}r_{\perp}^* & 0 & 0 \\ 0 & 0 & 2\text{Re}(r_{\parallel}r_{\perp}^*) & 2\text{Im}(r_{\parallel}r_{\perp}^*) \\ 0 & 0 & -2\text{Im}(r_{\parallel}r_{\perp}^*) & 2\text{Re}(r_{\parallel}r_{\perp}^*) \end{pmatrix}, \quad (2.6)$$

$$T = \frac{n_2 \cos \theta_t}{2n_1 \cos \theta_i} \begin{pmatrix} t_{\parallel}t_{\parallel}^* + t_{\perp}t_{\perp}^* & t_{\parallel}t_{\parallel}^* - t_{\perp}t_{\perp}^* & 0 & 0 \\ t_{\parallel}t_{\parallel}^* - t_{\perp}t_{\perp}^* & t_{\parallel}t_{\parallel}^* + t_{\perp}t_{\perp}^* & 0 & 0 \\ 0 & 0 & 2\text{Re}(t_{\parallel}t_{\perp}^*) & 2\text{Im}(t_{\parallel}t_{\perp}^*) \\ 0 & 0 & -2\text{Im}(t_{\parallel}t_{\perp}^*) & 2\text{Re}(t_{\parallel}t_{\perp}^*) \end{pmatrix}, \quad (2.7)$$

where  $n_1, n_2$  are the proper indices of refraction ( $n_1 = 1$  and  $n_2 = n$ , or  $n_2 = 1$  and  $n_1 = n$ ),  $\theta_i$  and  $\theta_t$  are the angles of incidence and refraction,  $r_{\parallel}, r_{\perp}, t_{\parallel}, t_{\perp}$  are the amplitude Fresnel coefficients. The matrix in equation (2.7) is prefixed with the Jacobian of transition from the coordinate system connected with the falling ray to that of the refracted one.

Note that equation (2.6) is also applicable to total internal reflection, the parallel and perpendicular components having different electromagnetic phases (Born and Wolf 1964):

$$tg \frac{\delta_{\parallel}}{2} = -\frac{\sqrt{\sin^2 \theta_i - (n_2/n_1)^2}}{(n_2/n_1)^2 \cos \theta_i}, \quad (2.8)$$

and

$$tg \frac{\delta_{\perp}}{2} = -\frac{\sqrt{\sin^2 \theta_i - (n_2/n_1)^2}}{\cos \theta_i}. \quad (2.9)$$

In this case the matrix  $R$  is simplified to

$$R = \begin{pmatrix} 1 & 0 & 0 & 0 \\ 0 & 1 & 0 & 0 \\ 0 & 0 & \cos(\delta_{\parallel} - \delta_{\perp}) & \sin(\delta_{\parallel} - \delta_{\perp}) \\ 0 & 0 & -\sin(\delta_{\parallel} - \delta_{\perp}) & \cos(\delta_{\parallel} - \delta_{\perp}) \end{pmatrix}. \quad (2.10)$$

The Monte Carlo ray tracing with the matrices  $K$ ,  $R$  and  $T$  lasts until the ray has been absorbed or has left the particle or the number of internal reflections exceeded a certain cutoff value restricting calculations of scattering orders. After that the scattering matrix  $F_{ik}$  for a given trajectory can be determined.

To average the result over all possible orientations, the particle is rotated around different axes on random angles. To calculate the dependence of scattering matrix elements on scattering angle  $\Theta$ , the range  $0^\circ$  to  $180^\circ$  is divided into a number of angular bins counted from the axis  $Z$ . Then, for each bin, elements  $F_{ik}$  corresponding to the ray scattered into this bin are summed. The sum of elements  $F_{11}$  normalized by the solid angle value of the given bin is the intensity  $I$  of scattered light. In this section we study dependences of six parameters expressed by non-zero scattering matrix elements,  $F_{11}$ ,  $-F_{12}/F_{11}$ ,  $F_{22}/F_{11}$ ,  $F_{33}/F_{11}$ ,  $F_{34}/F_{11}$ ,  $F_{44}/F_{11}$ , on scattering angle  $\Theta$ .

The integration over bins in narrow belts of a sphere, which is centered in the origin of the coordinate system, is characterized with unequal accuracy at different  $\Theta$ , because the particle indicatrices are non-isotropic. Besides, the polar regions of the spherical coordinate system have small solid angles and accumulation of rays goes slowly at very small and very large scattering angles  $\Theta$ . As a result, it is necessary to use a large number of initial rays, since we need to get rather high precision for forward and backward scattering. Usually we used in our calculations  $10^7$  rays.

## 2.2 Testing the model and comparison with Mie and DDA results

We have thoroughly tested this model. In particular, the algorithm was verified on the reciprocity principle expressed in the vector form. The quality of averaging-out over particle orientations has been checked by the criterion of smallness of the elements  $F_{13}$ ,  $F_{14}$ ,  $F_{23}$ ,  $F_{24}$ , and by the condition of symmetry  $F_{12} = F_{21}$  and anti-symmetry  $F_{34} = -F_{43}$ . The fulfilment of the symmetry relationships of the scattering matrix elements for exact forward and backward scattering (Mishchenko et al. (2000), table I and II) has also been checked.

In addition we compared ray tracing calculations of intensity ( $F_{11}$ ) and linear polarization ( $-F_{12}/F_{11}$ ) for a well approximated faceted sphere with Mie theory results. Although sphere is not an appropriate shape for approximation with flat facets, there is a simple and rigorous solution which can give data for test of our approximate model. The results of such a test are presented in figure 2.6. The solid line corresponds to Mie calculations

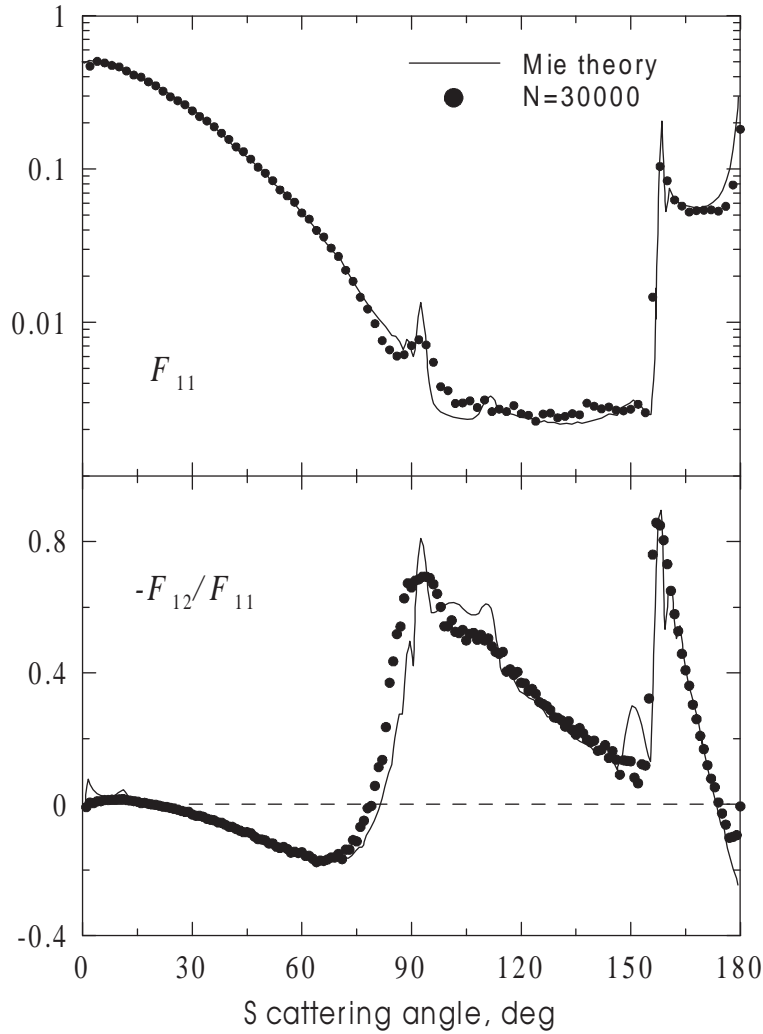


Figure 2.6: The scattering matrix element  $F_{11}$  and ratio  $-F_{12}/F_{11}$  versus scattering angle for a spherical particle approximated with  $N = 30000$  facets and results of Mie theory at  $n = 1.5$  and absorption coefficient  $k = 0$ .

for a sphere with size parameter  $x = 2r/\lambda = 1000$  ( $\lambda$  is the wavelength and  $r$  is the radius of the sphere), at  $n = 1.5$  and  $k = 0$ . Coherent effects are smoothed out here and forward scattering diffraction peak is removed (the Mie curves are taken from Grundy et al. (2000)). Points correspond to the GO results for a sphere with  $N = 30000$  facets. The figure shows good agreement. The GO curves look more smooth and there is a little shift of the main polarization maximum towards small scattering angles. This is explained by the fact that the taken number of facets is still not an ideal approximation for a sphere and small angular errors in the propagation directions of rays are present. Small polarization peak seen at  $\Theta = 150^\circ$  is due to coherent effects which take place even for such large spheres (Grundy et al. 2000).

Besides, we have compared our calculations of  $F_{11}$  and  $-F_{12}/F_{11}$  for a perfect cube with data of the same kind from (Muinonen et al. 1989) which revealed very good agreement.

Now we also consider the problem of the lower particle size limit  $x_{min}$  for geometric

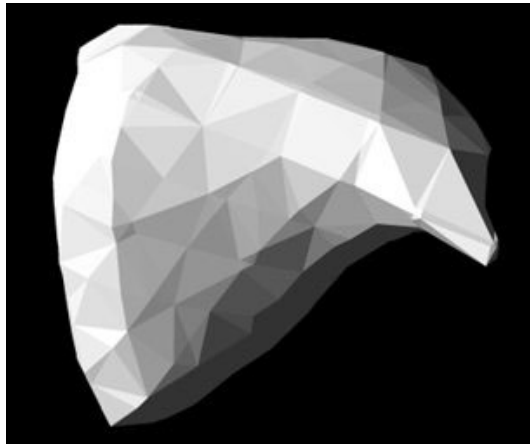


Figure 2.7: Particle sample used in the GO - DDA calculations

optics approximation.

One can easily estimate  $x_{min}$  for perfect spheres by means of Mie theory. For a good agreement of phase functions  $x_{min}$  must be of the order of several hundreds (Hansen and Travis 1974). However, GO appears to be more appropriate for smaller nonspherical than spherical particles. This is because, for spherical or other highly symmetric shapes, interference effects are strong and they are not included in the GO. So far GO approximation has been checked against T-matrix computations of regularly shaped particles: randomly oriented spheroids and circular cylinders.

Macke et al. (1995) considered prolate and oblate spheroids of different sizes from  $x = 10$  to 60 with complex refractive index  $m = 1.394 + i0.00684$ . It was found that for a size parameter of 60, GO and T-matrix phase function agree fairly well over the entire range of scattering angles. At the same time linear polarization appears to be more sensitive to the errors introduced by GO approximation. At  $x = 60$  spheroidal polarization curves show significant difference at intermediate phase angles.

Wielaard et al. (1997) modified T-matrix approach so that efficient computations of scattering by non-spherical particles with size parameters exceeding 100 became possible. With the improved model they considered two types of shape: randomly oriented monodisperse oblate spheroids ( $x = 85$ ) and circular cylinders ( $x = 125$ ). Calculations were made for non-absorbing ( $m = 1.311 + i0.0$ ) and weakly absorbing ( $m = 1.311 + i0.003$ ) particles. The authors conclude that from the phase function point of view the considered particles are already in the GO domain. GO and T-matrix differences in the scattering matrix elements  $F_{22}$ ,  $F_{33}$ ,  $F_{44}$ ,  $F_{12}$  and  $F_{34}$  are noticeably larger than those in the phase function. Introduction of weak absorption at the same value of the size parameter improves agreement. In general, approximate and accurate computations for the cylinders are in better agreement than those for spheroids. This could be explained by the sharp-edged shape of the cylinders, which makes interference effects less pronounced.

One can see that increasing particle irregularity tends to make ray tracing calculations more accurate for smaller particles. Most exact methods for light scattering are restricted to quite simple particle geometries and for truly irregular shapes such a test has not been done yet. Here we make a first attempt to solve this problem.

For accurate calculations we apply the DDA approach as it has no limitations on the

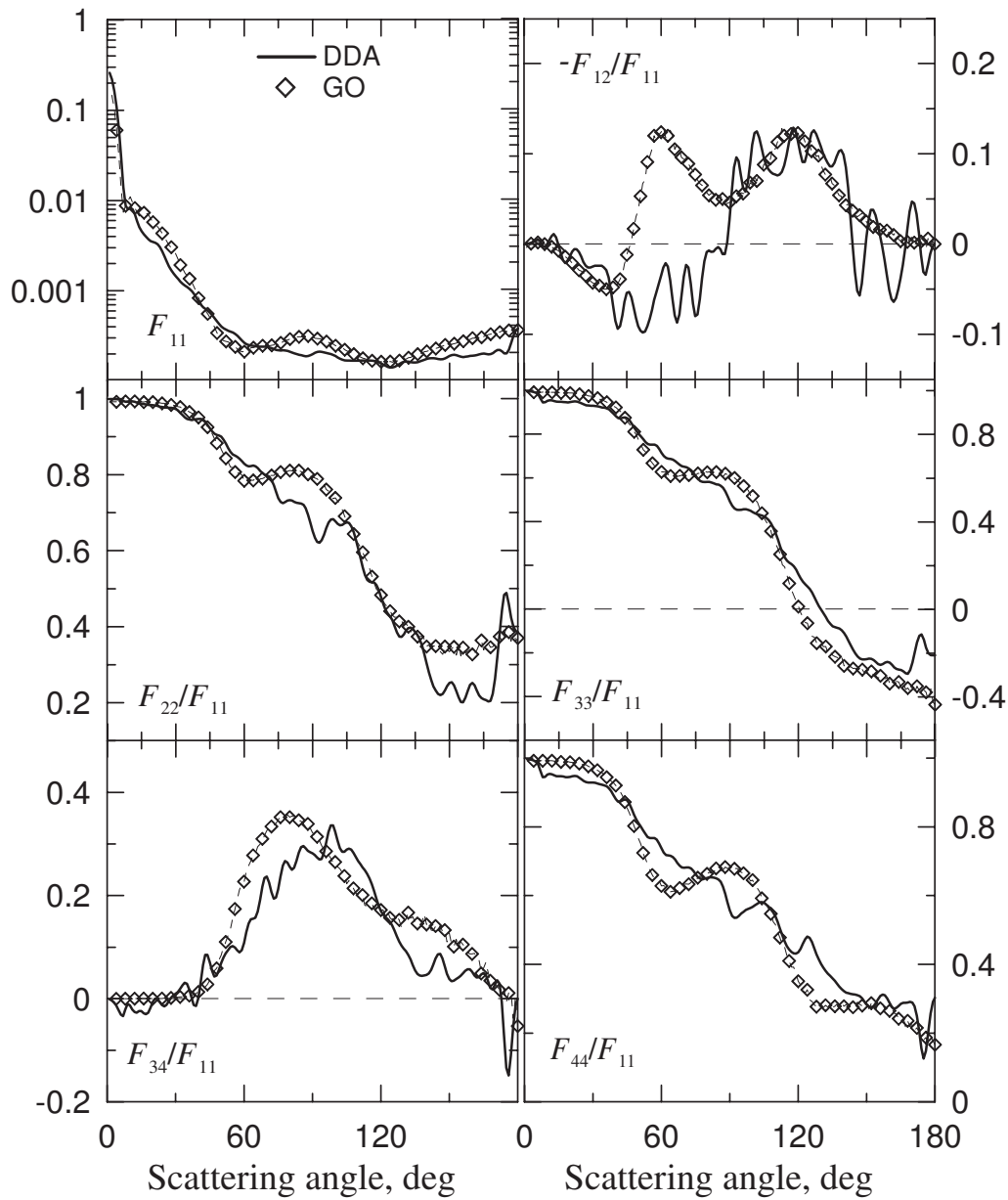


Figure 2.8: The scattering matrix element  $F_{11}$  and ratios  $-F_{12}/F_{11}$ ,  $F_{22}/F_{11}$ ,  $F_{33}/F_{11}$ ,  $F_{34}/F_{11}$ ,  $F_{44}/F_{11}$  versus scattering angle for a sample of random irregular particle with size parameter  $x = 30$ ,  $n = 1.313$  and  $k = 0$  calculated in the geometric optics approach (GO) and discrete dipole approximation (DDA).

particle shape. We use the DDA code developed by E. Zubko. Although it proved to be fast and efficient the maximum size parameter in our experiment was limited by  $x = 30$  and the calculations required parallel work of several PCs for quite long time. The refractive index was taken  $m = 1.313 + i0.0$ . Another limitation is that we were able to make computations for only one sample of irregular particle.

The sample of a faceted particle (Fig. 2.7) was generated using a random gaussian field. To represent the same shape in the form appropriate for DDA calculations we did the following. The generated particle was located in the 3-d cubic lattice with  $128 \times 128 \times 128$  cells. Then all cells (and dipoles correspondingly), which appeared within the volume confined by the surface facets were attributed to matter.

In Fig. 2.8 the scattering angle curves of the element  $F_{11}$  of the scattering matrix and the ratios  $-F_{12}/F_{11}$ ,  $F_{22}/F_{11}$ ,  $F_{33}/F_{11}$ ,  $F_{34}/F_{11}$ ,  $F_{44}/F_{11}$  for both types of calculations are shown. The forward scattering diffraction spike of intensity for the GO curve was calculated using Fraunhofer diffraction formula and added then independently to the phase function according to Macke et al. (1996b). The agreement between approximate and exact solutions is better for intensity ( $F_{11}$ ) than for other parameters. The worst situation is with polarization ( $-F_{12}/F_{11}$ ). At  $x = 30$  GO approach can reproduce only the maximum of positive polarization and partially the negative branch at small scattering angles. The negative branch in DDA continues till  $90^\circ$  whereas GO gives the second positive maximum in this region. In terms of GO the angular dependence of the linear polarization is determined by superposition of positively polarized external reflections (their contribution does not depend on the shape of a particle), negatively polarized forward refractions and multiple internal reflections. Mie calculations show that at  $x = 30$  external reflection produces the same polarization behavior as Fresnel's formulas do. Thus in our case positive polarization produced by external scattering is suppressed by certain internal wave effects which are not taken into account in the GO model. With the possibility of separation of coherent and incoherent mechanisms of scattering in DDA simulations (Zubko and Shkuratov 2005) the problem can be studied in more detail. On the other hand incorporating the interference effects into ray tracing modeling, probably, can further improve the accuracy of GO method for irregular particles as it was realized for hexagonal ice crystals by Yang and Liou (1995, 1996). We plan to study this in the future.

From this brief test we can say that the size parameter evidently cannot be less than 30 even for irregular particles. In case of particles of that size GO can be applied for phase function calculations only.

We also note that for shapes irregular enough there is no point in detailed comparison of the phase functions for single realizations of particles, since in GO phase function changes very little from sample to sample. The general trend remains the same and depends mostly on the complex refractive index. Fine details which appear in DDA calculations for a single sample of a particle, cannot be accurately reproduced in GO by definition. Therefore a more general test must include averaging over realizations and sizes to smooth out the oscillations.

## 2.3 Results of modeling of light scattering by particles with different shapes

Here we present results of calculations for five shape classes of particles: faceted spheres, faceted binary spheres, "spoiled" cubes, faceted ellipsoids, and RGF particles. We show dependences of the parameters  $F_{11}$ ,  $-F_{12}/F_{11}$ ,  $F_{22}/F_{11}$ ,  $F_{33}/F_{11}$ ,  $F_{34}/F_{11}$ ,  $F_{44}/F_{11}$ , on  $\Theta$  for different values of optical constants and parameters of the particle shape.

### 2.3.1 Faceted spheres

We start our modeling with spheres of different numbers of facets. In Fig. 2.9 the element  $F_{11}$  of scattering matrix and the ratios  $-F_{12}/F_{11}$ ,  $F_{22}/F_{11}$ ,  $F_{33}/F_{11}$ ,  $F_{34}/F_{11}$ ,  $F_{44}/F_{11}$  versus  $\Theta$  are presented for such spheres with the refractive index  $n = 1.5$  and absorption coefficient  $k = 0$ . Sums over all significant orders of scattering are taken; usually this includes a few hundreds of orders. As one can see, the curves corresponding to  $N = 10000$  and  $30000$  are similar for all studied parameters. I.e. on average a spherical particle formed with more than 10000 flat facets, can be considered as a rather perfect sphere. When  $N$  is smaller, changes are observed. Thus, for  $F_{11}$  at  $N = 1000$  the glory surge disappears and, moreover, instead of the surge an opposition "anti-spike" is developed. At  $N = 100$ , neither the glory nor the first rainbow are observed. Weakening of oscillations with the decrease of  $N$  is clearly seen for the ratio  $-F_{12}/F_{11}$ . This ratio corresponds to the definition of linear polarization degree of scattered radiation, when particles are illuminated with unpolarized light. So, as one can see in Fig. 2.9, the small negative polarization branch, which is observed for the perfect spheres near the backscatter direction,  $\Theta = 180^\circ$ , disappears for roughly faceted particles. The surge of positive polarization corresponding to the first rainbow goes down quickly with decreasing  $N$ . The negative polarization branch at small scattering angles weakens for roughly faceted spheres too.

Spheres do not depolarize the incident light at all (Bohren and Huffman 1983, Born and Wolf 1964). The curves of the ratio  $F_{22}/F_{11}$  presented in Fig. 2.9 are in agreement with this. Thus, at  $N = 10000$  and  $30000$  the ratio  $F_{22}/F_{11}$  is almost equal 1. There are deviations only at very large and very small scattering angles that are probably due to poor statistics at these angles. For non-perfect spheres,  $N = 1000$  and  $100$ , the ratio  $F_{22}/F_{11}$  varies rather strongly. These particles depolarize light noticeably. The ratio  $F_{33}/F_{11}$  is related to orientation of the linear polarization plane of scattered light. We see in Fig. 2.9 that the angle dependences of this ratio correlate with the corresponding curves  $-F_{12}/F_{11}$ . The ratio  $F_{34}/F_{11}$  is responsible for mutual transformation of linear and circular polarization. Our calculations show that this transformation is not observed in the range  $0^\circ - 60^\circ$  and the backscattering direction. The ratio  $F_{44}/F_{11}$  describes the change of circular polarization. It has different signs for perfect and roughly faceted spheres near the backscattering direction. The  $F_{33}/F_{11}$  and  $F_{44}/F_{11}$  curves are similar; noticeable difference is observed only at large  $\Theta$ .

We studied contributions of different orders of scattering to the described functions. First of all note that here and below we do not show data for the first order of scattering, as this is the well-known single Fresnel reflection from the external surface of particle. We investigate the next three orders of scattering: (1) the forward refraction and the single (2)

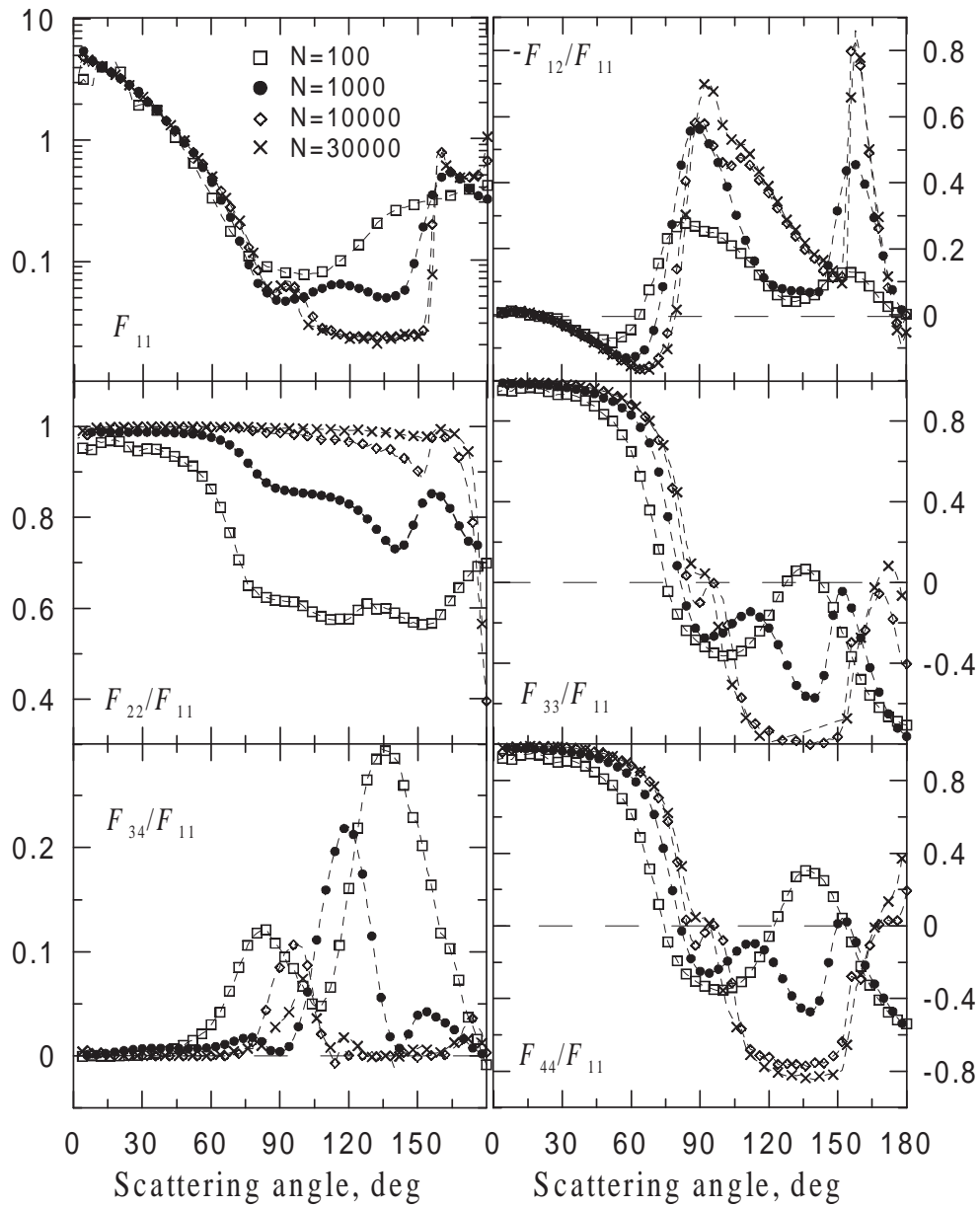


Figure 2.9: The scattering matrix element  $F_{11}$  and ratios  $-F_{12}/F_{11}$ ,  $F_{22}/F_{11}$ ,  $F_{33}/F_{11}$ ,  $F_{34}/F_{11}$ ,  $F_{44}/F_{11}$  versus scattering angle (sums over all significant orders of scattering) for spherical particles approximated by different number of facets  $N$  with the refractive index  $n = 1.5$  and absorption coefficient  $k = 0$ .

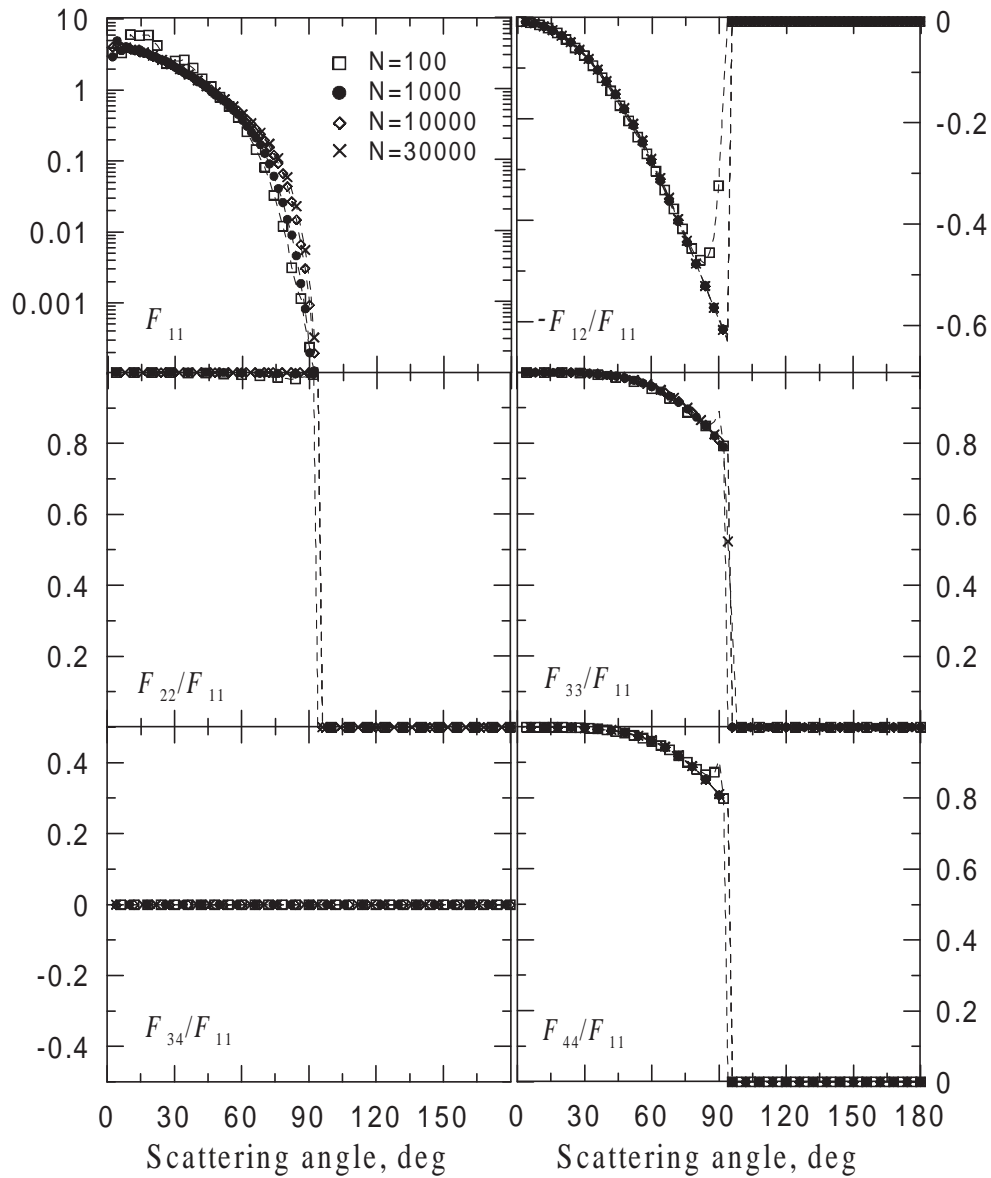


Figure 2.10: The scattering matrix element  $F_{11}$  and ratios  $-F_{12}/F_{11}$ ,  $F_{22}/F_{11}$ ,  $F_{33}/F_{11}$ ,  $F_{34}/F_{11}$ ,  $F_{44}/F_{11}$  versus scattering angle for the forwardly refracted component for spherical particles approximated by different number of facets  $N$  with the refractive index  $n = 1.5$  and absorption coefficient  $k = 0$ .

and double (3) internal reflection. It should be emphasized that these three components dominate the total scattered light flux, even if the absorption coefficient  $k$  equals zero. We stress that each of these three orders of scattering imply a different kind of light interaction with the particle boundary; for instance, the second order includes only two refractions, the third one includes two refractions and one reflection, and so on.

Looking at Fig. 2.10 one can see that the forwardly refracted component contributes to scattering only in the range  $0^\circ - 95^\circ$ . Rays, going through particles without internal reflections, cannot be refracted to larger  $\Theta$  at  $n = 1.5$ . This component has very strong negative linear polarization in the range  $0^\circ - 95^\circ$ , if incident light is initially unpolarized. Judging the behavior of  $F_{22}/F_{11}$ , depolarization does not take place for this component even for roughly faceted spheres. No surprising features are observed in this case at variations of  $N$ .

Fig. 2.11 shows data for the component corresponding to single internal reflection, when rays refracted into a particle are reflected inside and then refracted out. This component dominates mainly the first rainbow centered near  $160^\circ$ . This feature is quickly relaxed in the parameter  $F_{11}$  with decreasing  $N$ . The component gives a prominent backscattering effect for roughly faceted spheres at  $N = 100$ . This effect can be seen in total intensity in Fig. 2.9. It is interesting that at  $N = 100$  the rainbow is absent in  $F_{11}$ , but seen very well in  $-F_{12}/F_{11}$ . Fig. 2.11 shows that the intensity of the single reflection is very low at  $\Theta < 120^\circ$ . Thus the details observed for the other parameters in the range  $0^\circ - 120^\circ$  are perhaps caused by poor statistics. Fig. 2.11 clearly shows that the component can strongly be depolarized at the backscattering direction if particles are roughly faceted. Comparing the functions  $F_{44}/F_{11}$  in Figs. 2.9 and 2.114 at  $\Theta > 150^\circ$ , one can deduce that the difference in the behavior of the perfectly ( $N = 30000$  and  $10000$ ) and roughly ( $N = 1000$  and  $100$ ) faceted spheres is due to the single internal reflection.

The dependence for the component of double reflection inside particles on scattering angle are presented in Fig. 2.12. The component for perfect spheres forms the second rainbow at approximately  $90^\circ$ . In the parameter  $F_{11}$  this feature shifts toward large  $\Theta$  with decreasing  $N$ . For perfect spheres the component cannot contribute to angles close to  $\Theta = 180^\circ$ . This becomes possible only for roughly faceted spheres. In case of  $N = 1000$ , a strong negative branch of the parameter  $-F_{12}/F_{11}$  is observed near  $\Theta = 180^\circ$ . This corresponds to a negative polarization effect, if particles are illuminated with unpolarized light. Nevertheless, in the total dependence of  $-F_{12}/F_{11}$  on scattering angle this negative branch is not observed, as it is entirely compensated by positive polarization of the single internal reflection. The case  $N = 100$  is also very interesting. The detail corresponding to the second rainbow shifts to  $\Theta = 180^\circ$  and provides a strong backscatter effect. The negative polarization is also observed, though this is less prominent than in case of  $N = 1000$ . At  $\Theta$  close to  $140^\circ$  roughly faceted particles provide for this component an effective transformation of linear polarization in circular and vice versa (see in Fig. 2.12 curves corresponding to  $F_{34}/F_{11}$ ).

Fig. 2.13 shows element  $F_{11}$  of scattering matrix and ratios  $-F_{12}/F_{11}$ ,  $F_{22}/F_{11}$ ,  $F_{33}/F_{11}$ ,  $F_{34}/F_{11}$ ,  $F_{44}/F_{11}$  vs.  $\Theta$  for a spherical particle approximated by  $N = 100$  facets with different values of the refractive indices  $n$  and absorption coefficient  $k = 0$ . As one can see all curves on each panel are more or less similar to each other; the main details of the curves shifts toward small  $\Theta$  with decreasing  $n$ . We note a very conspicuous backscattering effect for all studied refractive index values. The variation of  $n$  gives nothing for

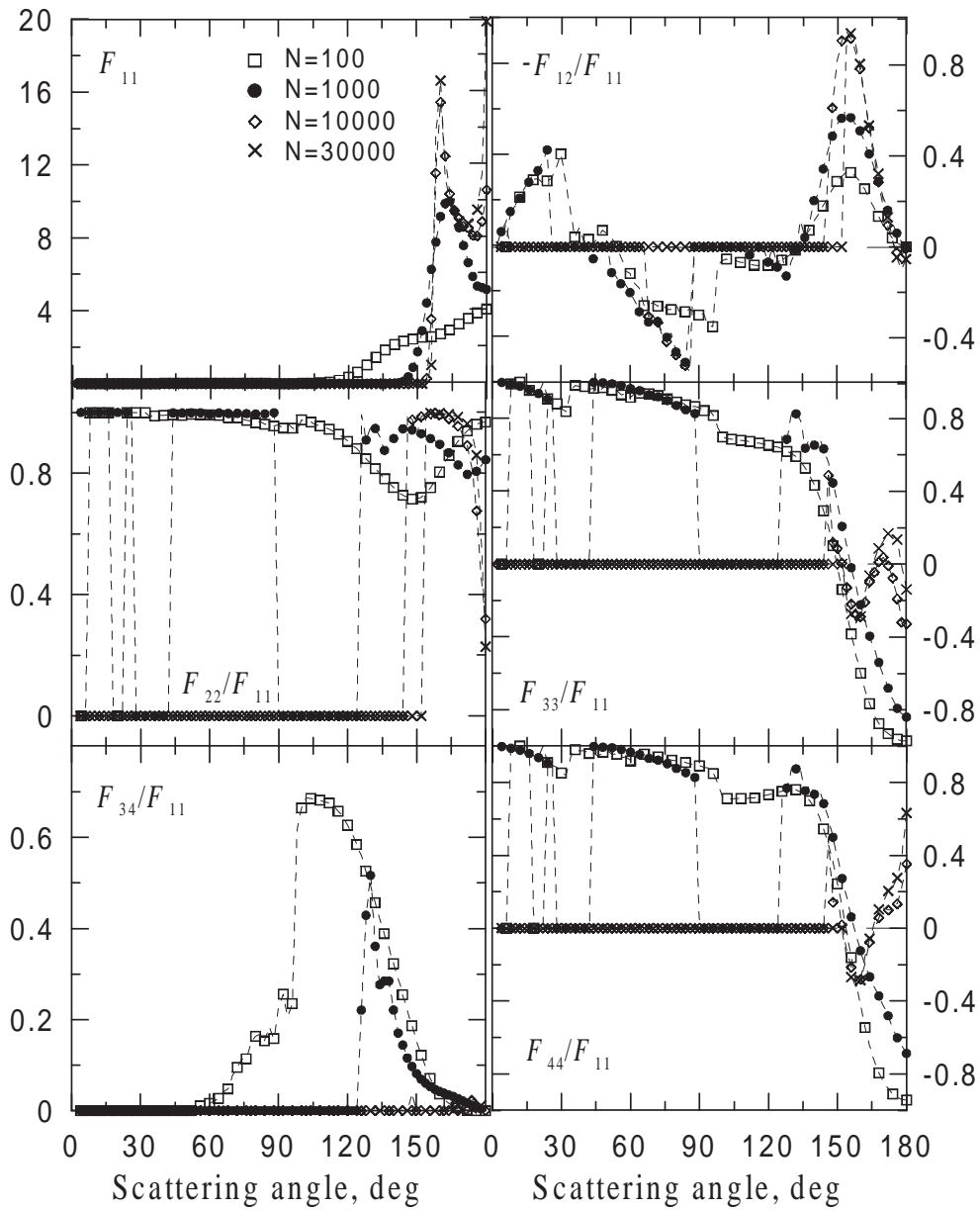


Figure 2.11: The scattering matrix element  $F_{11}$  and ratios  $-F_{12}/F_{11}$ ,  $F_{22}/F_{11}$ ,  $F_{33}/F_{11}$ ,  $F_{34}/F_{11}$ ,  $F_{44}/F_{11}$  versus scattering angle for the component of scattered radiation corresponding to single internal reflection for spherical particles approximated by different number of facets  $N$  with the refractive index  $n = 1.5$  and absorption coefficient  $k = 0$ .

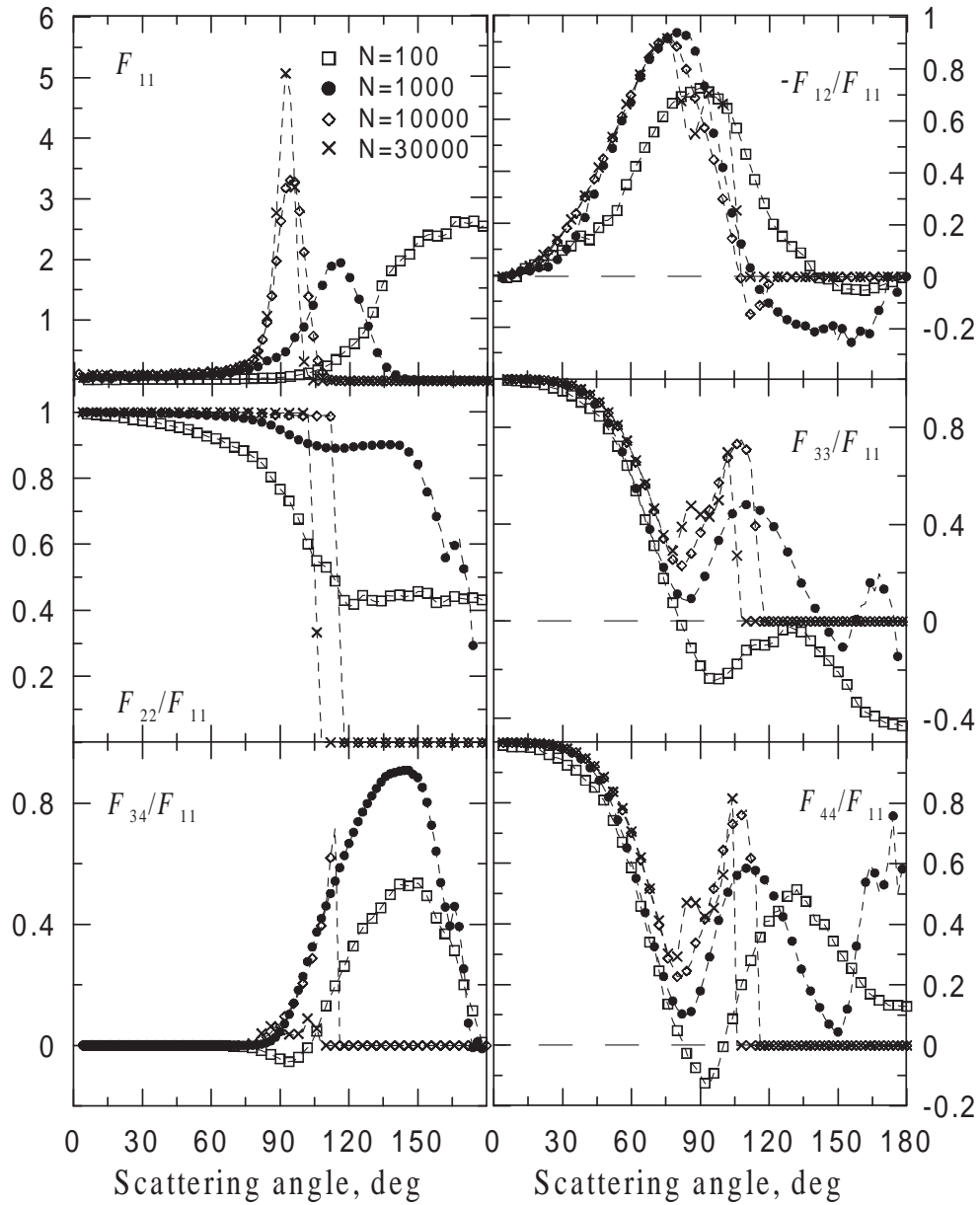


Figure 2.12: The scattering matrix element  $F_{11}$  and ratios  $-F_{12}/F_{11}$ ,  $F_{22}/F_{11}$ ,  $F_{33}/F_{11}$ ,  $F_{34}/F_{11}$ ,  $F_{44}/F_{11}$  versus scattering angle for the component of scattered radiation corresponding to double internal reflection for spherical particles approximated by different number of facets  $N$  with the refractive index  $n = 1.5$  and absorption coefficient  $k = 0$ .

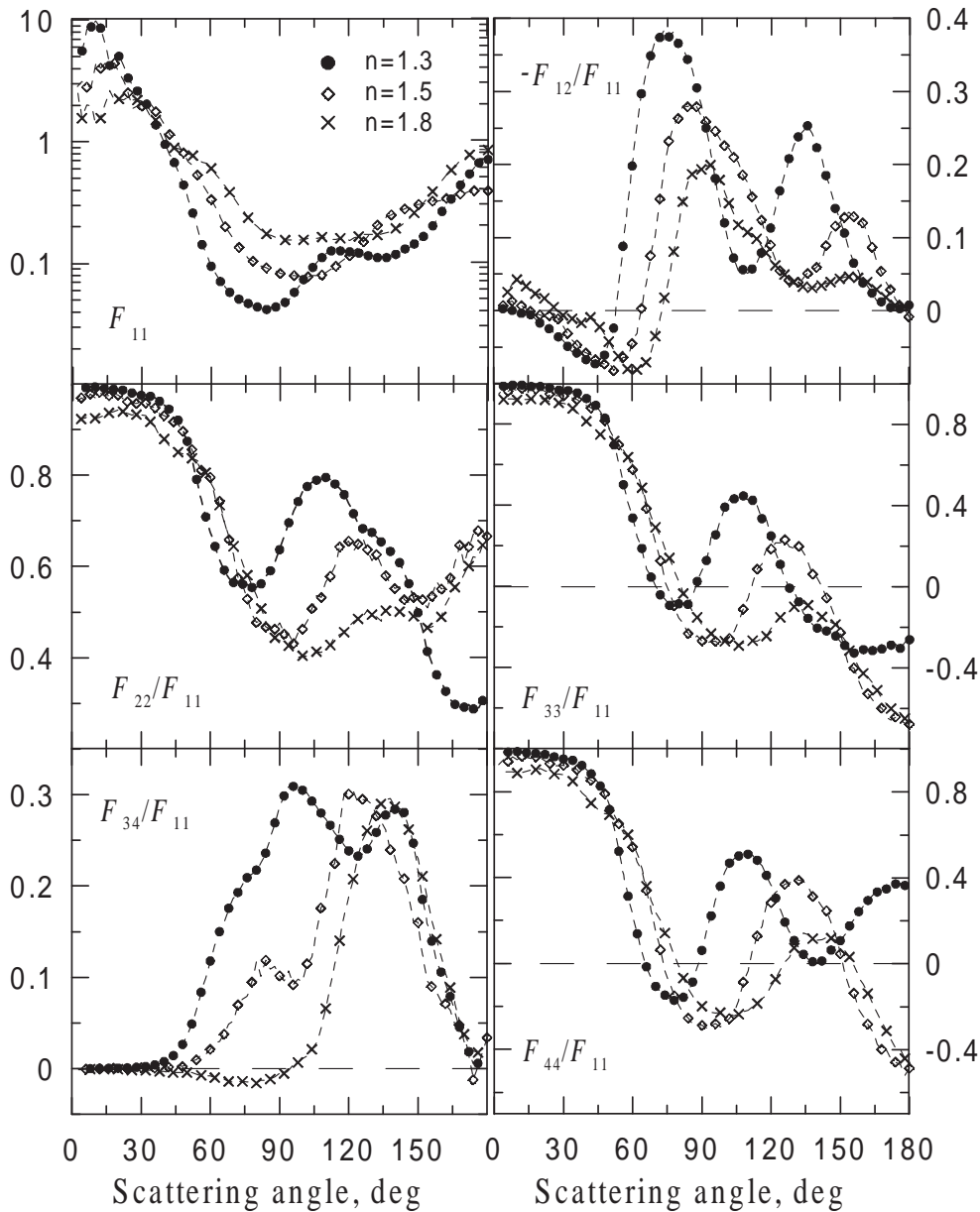


Figure 2.13: The scattering matrix element  $F_{11}$  and ratios  $-F_{12}/F_{11}$ ,  $F_{22}/F_{11}$ ,  $F_{33}/F_{11}$ ,  $F_{34}/F_{11}$ ,  $F_{44}/F_{11}$  versus scattering angle for spherical particles with different values of  $n$  at  $k = 0$  and  $N = 100$ .

appearance of the negative polarization branch at large  $\Theta$  (see  $-F_{12}/F_{11}$ ), which is present for perfect spheres. In Fig. 2.14 the data of the same kind is presented at  $n = 1.5$ , when  $k$  varies. In this case an additional parameter should be used,  $L/\lambda$ , where  $L$  is the mean ray path-length within the particle. For the data given in Fig. 2.14  $L/\lambda = 31$ . With growth of  $k$  the intensity of scattered light decreases significant especially in backward direction. The curves for the ratio  $-F_{12}/F_{11}$  are almost coincident in the backscattering part, but they show noticeable differences in the forward scattering part. For example, the negative polarization branch corresponding to forward scattering disappears with growing  $k$ . The depolarizing ability of the particles decreases sharply at large  $\Theta$  with growing  $k$ .

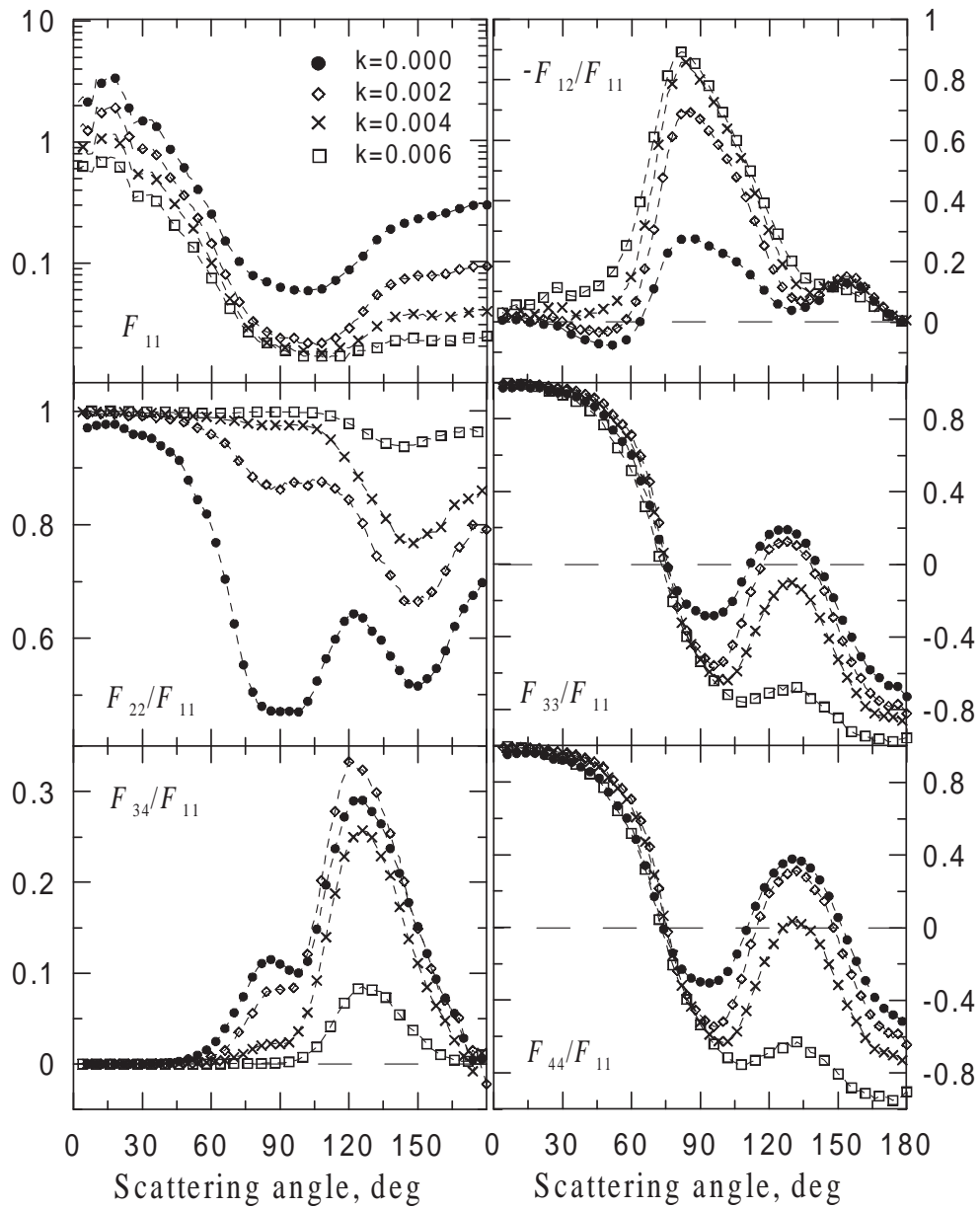


Figure 2.14: The scattering matrix element  $F_{11}$  and ratios  $-F_{12}/F_{11}$ ,  $F_{22}/F_{11}$ ,  $F_{33}/F_{11}$ ,  $F_{34}/F_{11}$ ,  $F_{44}/F_{11}$  versus scattering angle for spherical particles with different values of  $k$  at  $n = 1.5$  and  $N = 100$ . Ratio of the mean ray path length within the sphere to the wavelength  $L/\lambda = 31$ .

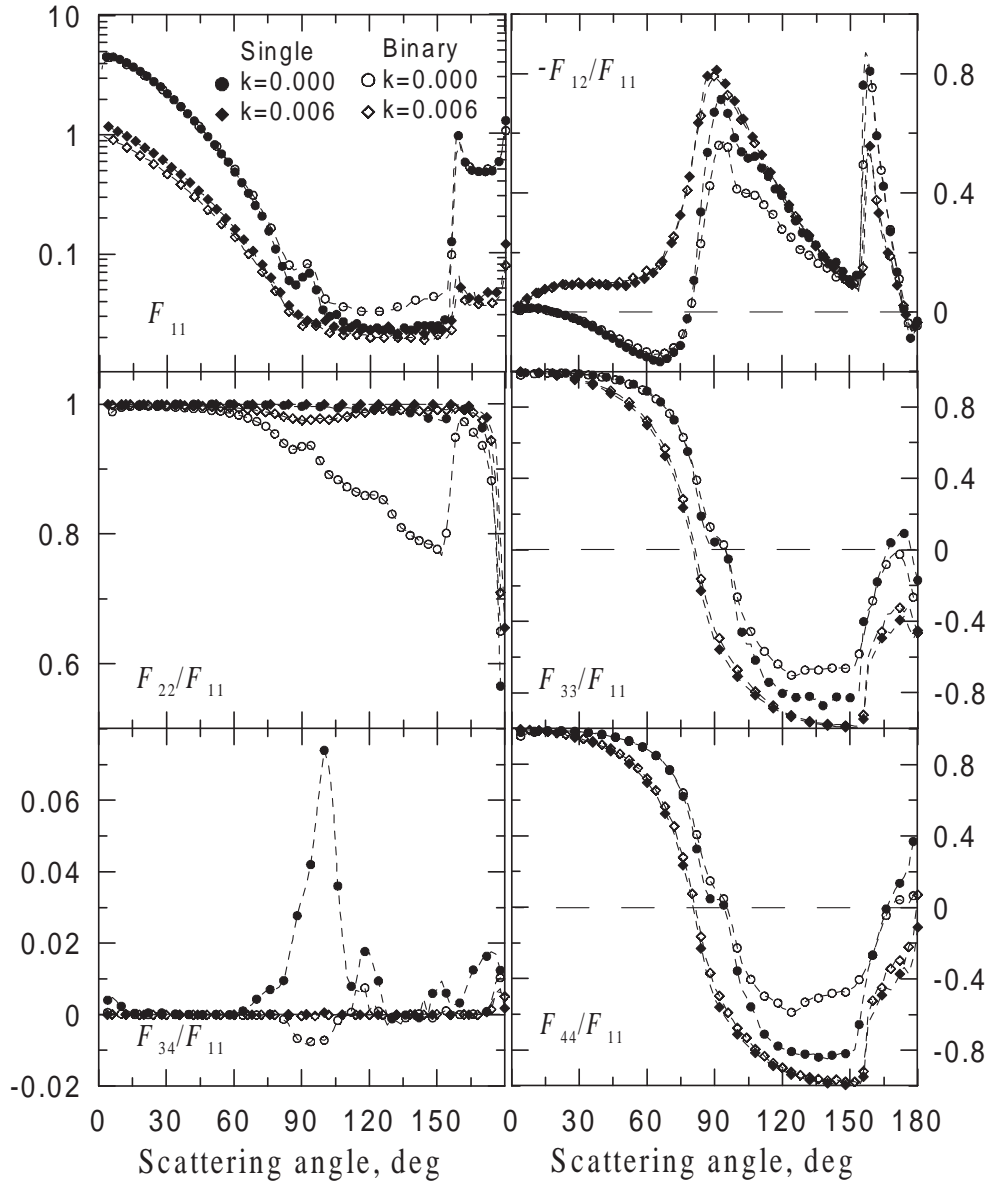


Figure 2.15: The scattering matrix element  $F_{11}$  and ratios  $-F_{12}/F_{11}$ ,  $F_{22}/F_{11}$ ,  $F_{33}/F_{11}$ ,  $F_{34}/F_{11}$ ,  $F_{44}/F_{11}$  versus scattering angle (sums over all significant orders of scattering) for single sphere and two similar touching spheres approximated by  $N = 30000$  facets with different values of  $k$  at  $n = 1.5$ . Ratio of the mean ray path length within the sphere to the wavelength  $L/\lambda = 41$ .

### 2.3.2 Binary spheres and faceted ellipsoids

Light scattering by arbitrary shaped particles comparable in size to the wavelength of incident radiation, are often simulated by ellipsoids and aggregates of spheres (Mishchenko et al. 2000). We study here this approximation in the geometric optics approach.

We use binary touching spheres (bispheres) as a model of an irregular particle. We generate bispheres with the same size and optical constants, though there are no difficulties in making them different. Touching spheres have perfect shape and they are approx-

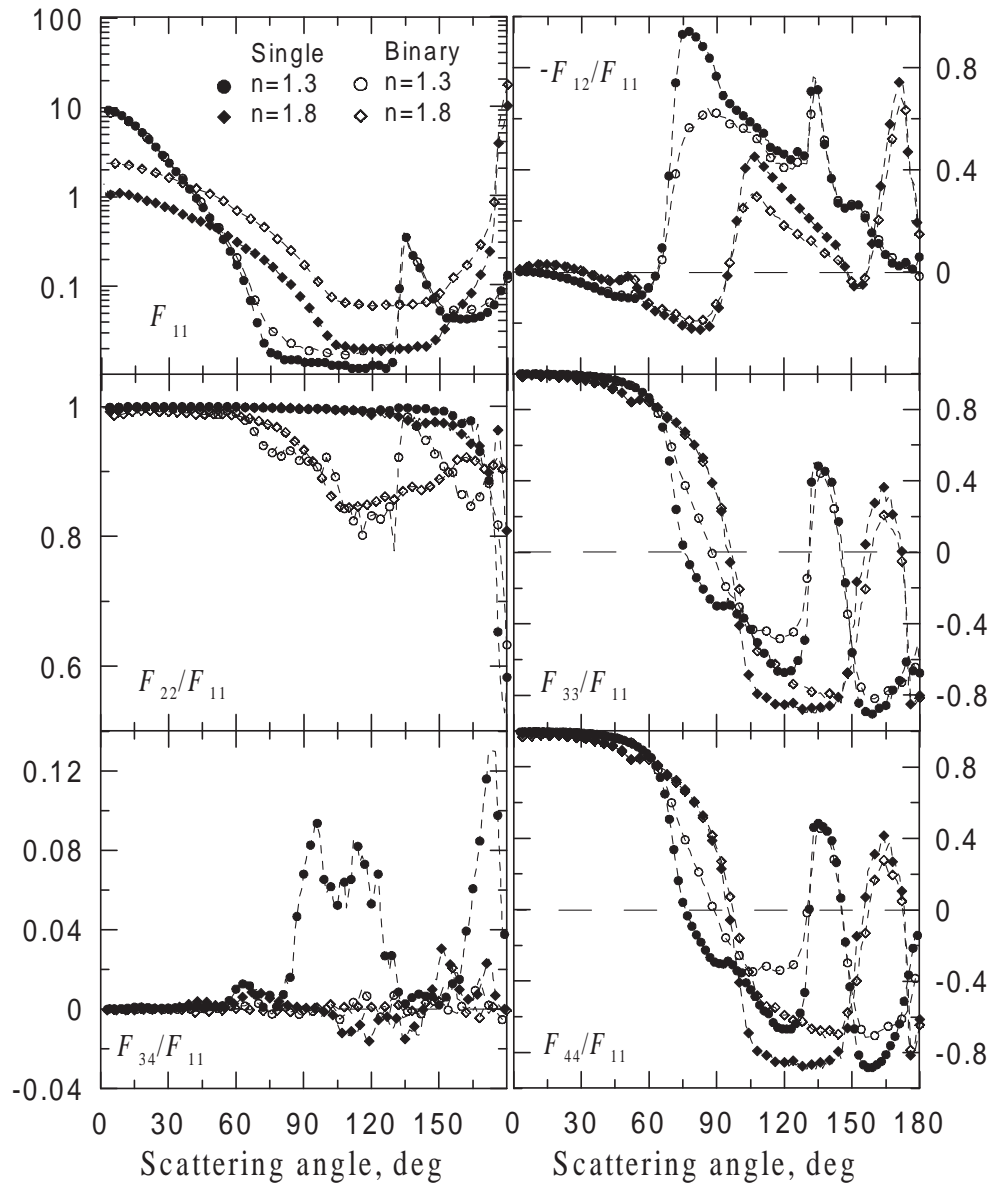


Figure 2.16: The scattering matrix element  $F_{11}$  and ratios  $-F_{12}/F_{11}$ ,  $F_{22}/F_{11}$ ,  $F_{33}/F_{11}$ ,  $F_{34}/F_{11}$ ,  $F_{44}/F_{11}$  versus scattering angle (sums over all significant orders of scattering) for single sphere and two similar touching spheres approximated by  $N = 30000$  facets with different values of  $n$  at  $k = 0$ .

imated by  $N = 30000$  facets. Results of our calculations for the element  $F_{11}$  and ratios  $-F_{12}/F_{11}$ ,  $F_{22}/F_{11}$ ,  $F_{33}/F_{11}$ ,  $F_{34}/F_{11}$  vs.  $\Theta$  for single and binary spheres with  $n = 1.5$ ,  $L/\lambda = 41$ , and different  $k$  are presented in Fig. 2.15. The same is shown in Fig. 2.16 for different refractive indices  $n$  at  $k = 0$ . In both cases the compared curves are very similar, this indicates showing that the contribution of the inter-particle scattering component to the total flux of scattered light is small. An exception is observed for the ratio  $F_{22}/F_{11}$ , which is related to the depolarization ability of scattering objects. This ratio noticeably deviates from unity (as it should be) at large  $\Theta$ . Thus we generally confirm the result obtained with the DDA approximation for small particles (Zubko et al. 2001) that it is not sufficiently good approach to model irregular particles with spheres, as the optical properties of the spheres substantially dominate the total scattering.

Fig. 2.17 shows results of our calculations for the same set of the studied parameters for scattering only by both spheres. This characterizes interaction (inter-particle scattering) between spheres. We present in Fig. 2.17 four curves that correspond to the following cases, which practically exhaust interactions between these particles:

- (1) externally reflected rays from one particle go to the other particle to reflect externally again (double external reflections between particles);
- (2) externally reflected rays from one particle go to the other particle and then are either externally reflected or forwardly refracted or internally reflected one and two times;
- (3) either externally reflected or forwardly refracted or internally (once and twice) reflected rays from one particle go to the other one and then are externally reflected;
- (4) either externally reflected or forwardly refracted or internally reflected rays from one particle go to the other one and then are either externally reflected or forwardly refracted or internally reflected.

As can be seen in Fig. 2.17 inter-particle scattering (curve 4) is responsible for a very small portion of total scattering from binary spheres (solid line). Double external reflections (curve 1) provide a relatively small contribution to inter-particle scattering. This component reveals a narrow negative polarization branch at small scattering angles (see  $-F_{12}/F_{11}$ ), but definitely not at large  $\Theta$ . The presence of the negative polarization branch at large  $\Theta$  was predicted by some theories based on Fresnel reflections (Wolff 1975, Steigmann 1978, Kolokolova 1990). The considered component produces also a high depolarization effect (see  $F_{22}/F_{11}$ ). The components (2) and (3) listed above are similar and show noticeable difference only for  $-F_{12}/F_{11}$ . The resemblance is a manifestation of the reciprocity principle; the difference in polarization degree is not restricted by the principle.

Another example of irregularly shaped particles is faceted ellipsoids. In this case we have two parameters to describe the particle shape: the ratio of ellipsoid axes  $d$  and number of facets  $N$ . An ellipsoid is oblate if  $d < 1$  and prolate if  $d > 1$ . In Fig. 2.18 the element  $F_{11}$  and ratios  $-F_{12}/F_{11}$ ,  $F_{22}/F_{11}$ ,  $F_{33}/F_{11}$ ,  $F_{34}/F_{11}$ ,  $F_{44}/F_{11}$  are presented for ellipsoids with different axis ratios  $d$  at  $N = 30000$ ,  $n = 1.5$ , and  $k = 0$ . The oblate ellipsoids have relatively small values of the parameter  $-F_{12}/F_{11}$  in the full angle range. The capability of ellipsoids to depolarize incident light increases with growing  $\Theta$ . In Fig. 2.19 the same parameters are given for ellipsoids approximated by different number of facets  $N$  with axis ratio  $d = 4/5$  at  $n = 1.5$ , and  $k = 0$ . In Fig. 2.18 and 2.19, sums over all significant orders of scattering are presented. Different tenuous features in the intensity and polarization dependences are blurred as  $N$  decreases. At  $N = 1000$  they

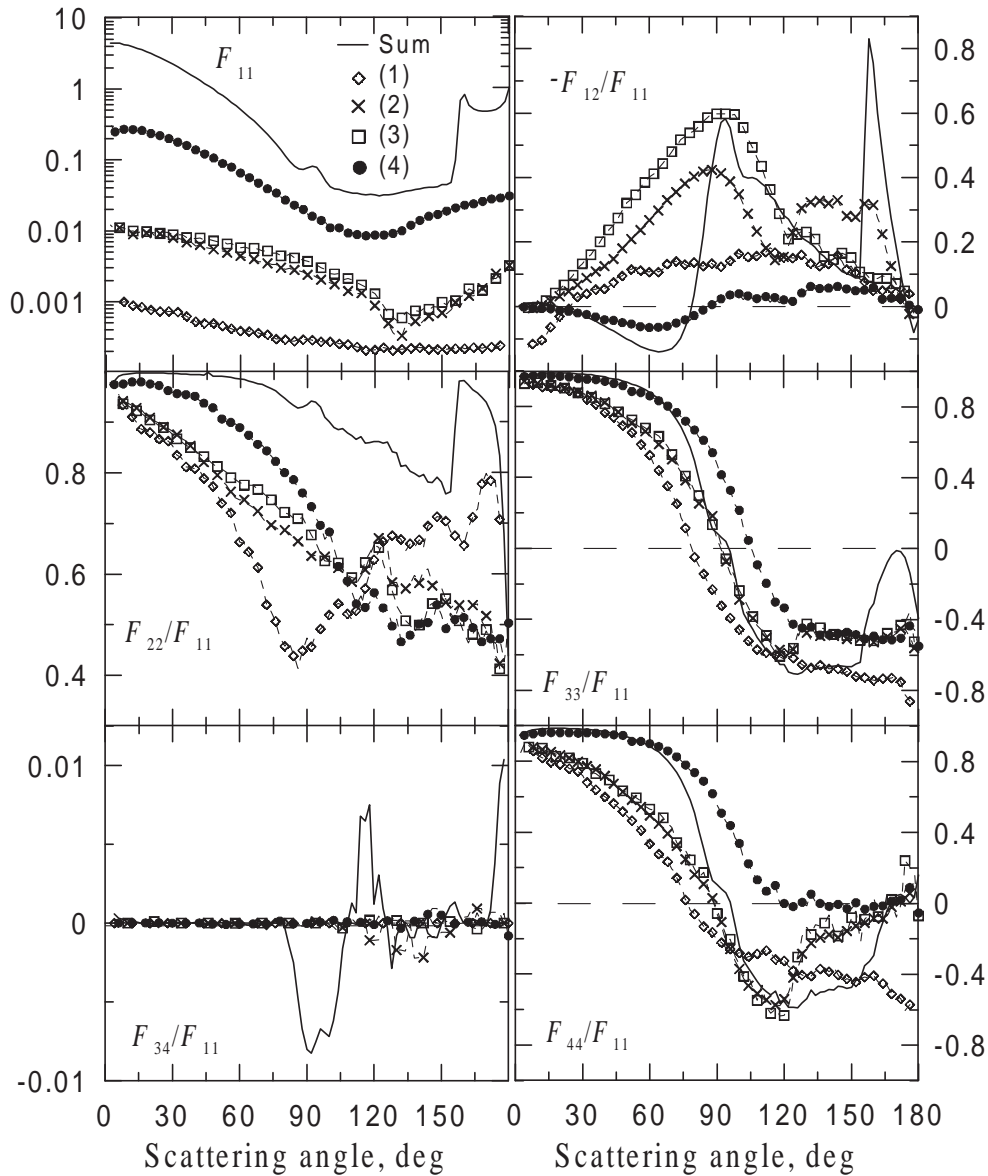


Figure 2.17: The scattering matrix element  $F_{11}$  and ratios  $-F_{12}/F_{11}$ ,  $F_{22}/F_{11}$ ,  $F_{33}/F_{11}$ ,  $F_{34}/F_{11}$ ,  $F_{44}/F_{11}$  versus scattering angle for inter-particle components of two similar touching spheres approximated by  $N = 30000$  facets at  $n = 1.5$  and  $k = 0$ . The numbers correspond to the cases: (1) externally reflected rays from one particle go to the other particle to reflect externally again (double reflection between particles); (2) externally reflected rays from one particle go to the other particle and then are externally reflected, forwardly refracted, and internally reflected one and two times; (3) externally reflected, forwardly refracted, and internally (once and twice) reflected rays from one particle go to the other one and then are externally reflected; (4) externally reflected, forwardly refracted, and internally reflected rays from one particle go to the other one and then are externally reflected, forwardly refracted, and internally reflected. Solid line shows total scattering including in-particle as well as inter-particle components.

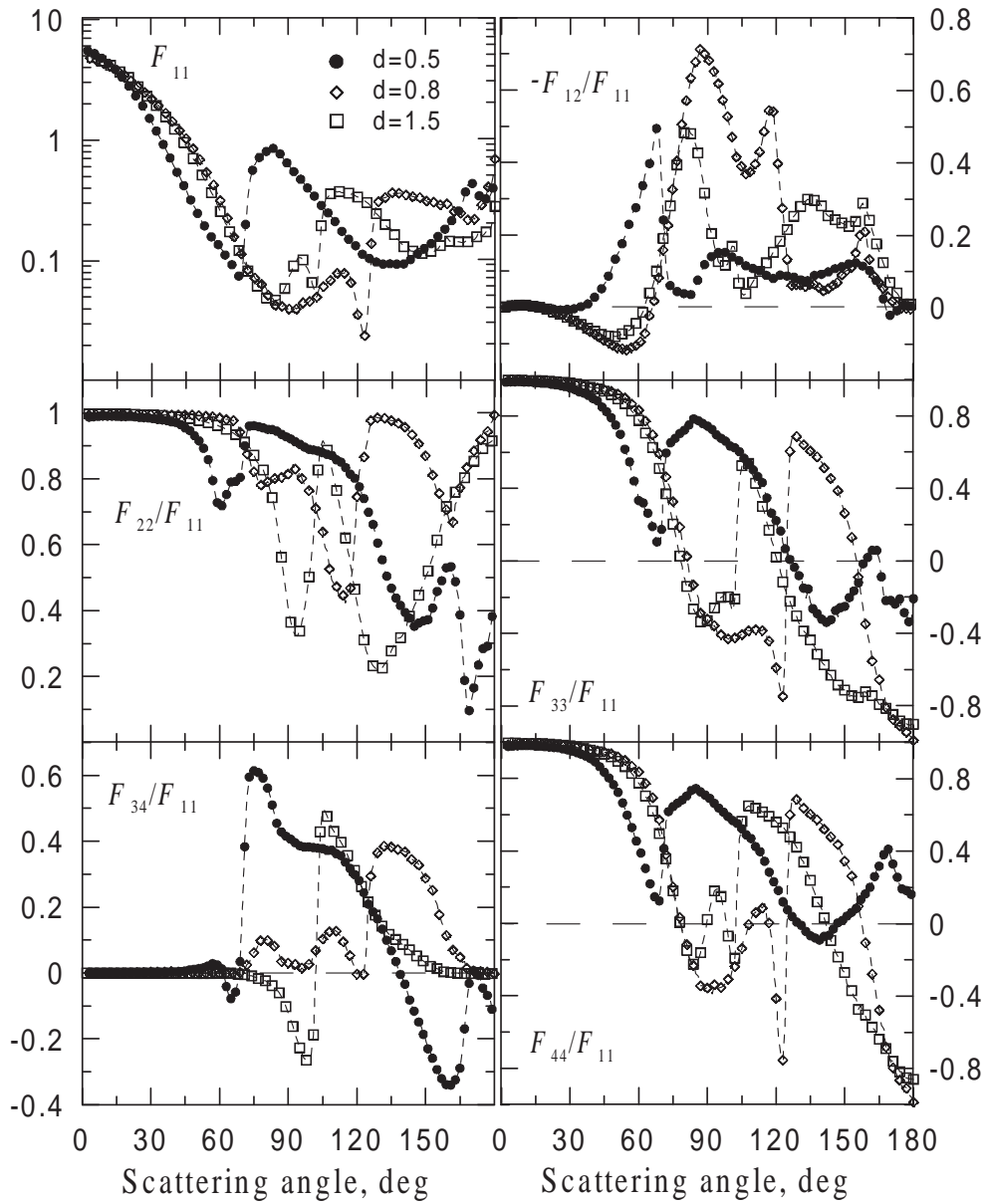


Figure 2.18: The scattering matrix element  $F_{11}$  and ratios  $-F_{12}/F_{11}$ ,  $F_{22}/F_{11}$ ,  $F_{33}/F_{11}$ ,  $F_{34}/F_{11}$ ,  $F_{44}/F_{11}$  versus scattering angle (sums over all significant orders of scattering) for faceted ellipsoids with different axis ratios  $d$  at  $n = 1.5$  and  $k = 0$ .

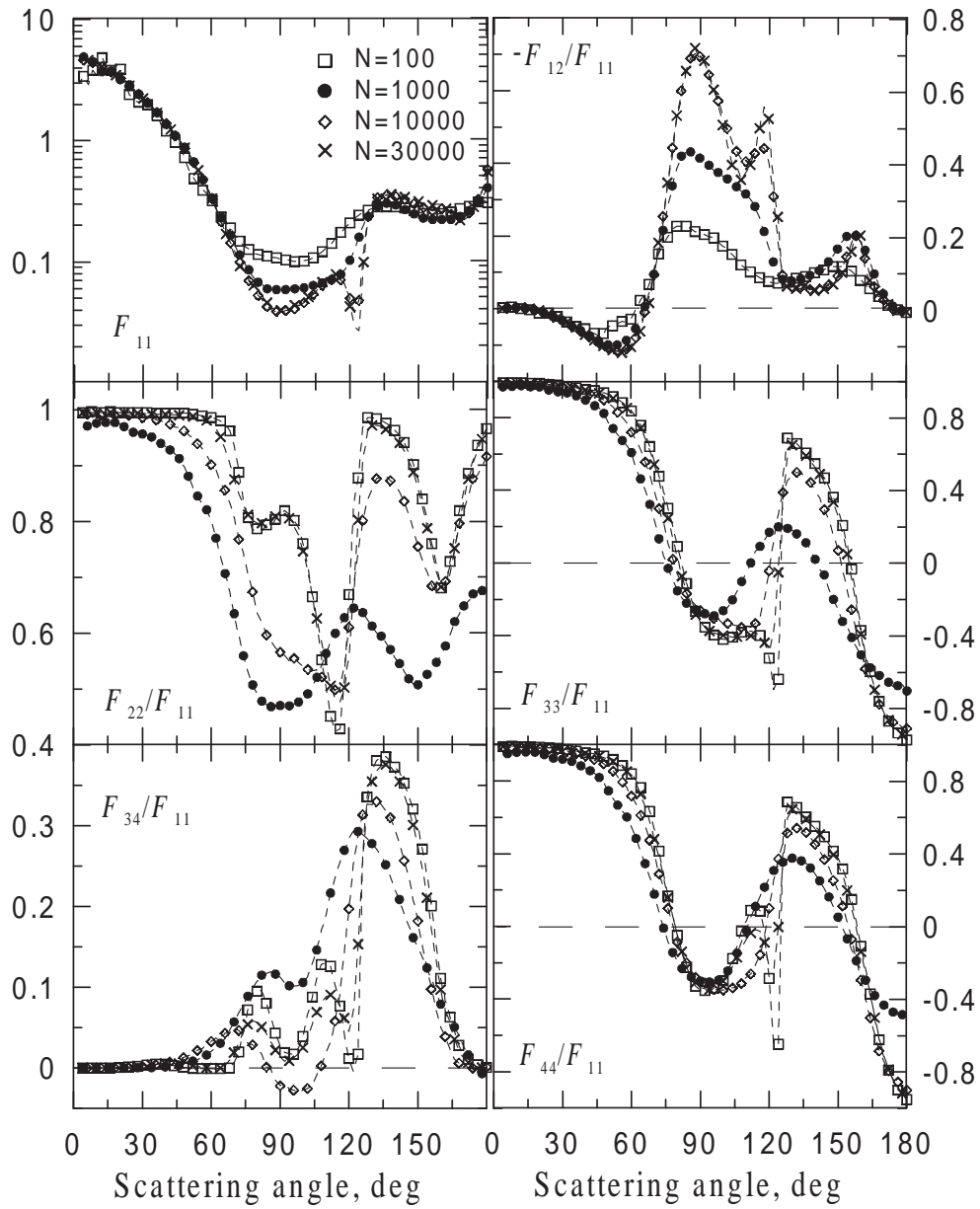


Figure 2.19: The scattering matrix element  $F_{11}$  and ratios  $-F_{12}/F_{11}$ ,  $F_{22}/F_{11}$ ,  $F_{33}/F_{11}$ ,  $F_{34}/F_{11}$ ,  $F_{44}/F_{11}$  versus scattering angle for ellipsoids approximated by different number of facets  $N$  with  $d = 4/5$  at  $n = 1.5$  and  $k = 0$ .

even disappear. In the maximum the ratio  $-F_{12}/F_{11}$  is 3 times lower for roughly faceted ellipsoid with  $N = 100$ , than for well approximated one. Plots for different scattering orders are qualitatively similar to those for spherical particles, and we do not show these here. Unlike binary spheres, as compared with spheres ellipsoids reveal more deviations in scattering properties. We note that all studied parameters, the element  $F_{11}$  and ratios  $-F_{12}/F_{11}$ ,  $F_{22}/F_{11}$ ,  $F_{33}/F_{11}$ ,  $F_{34}/F_{11}$ ,  $F_{44}/F_{11}$ , for roughly faceted spheres and ellipsoids at  $d = 4/5$  are very similar.

### 2.3.3 Perfect and "spoiled" cubes

To obtain particles with irregular shape, we used perfect cubes deforming them in the following way. Each vertex of a cube is randomly moved in a random direction. The shift has zero average and certain amplitude  $\delta$  that is given in the length of the cube edge. We varied  $\delta$  from 0 (perfect cube) to 0.2 (very irregular particle). As in the case of other particles irregular cubes are approximated with triangle facets (see Fig. 2.1). Sums over all significant orders of scattering are presented in Fig. 2.20 that illustrates how  $F_{11}$  and the rest parameters being functions of  $\Theta$  depend on random deviations from cube at  $n = 1.5$  and  $k = 0$ . The ideal cube gives forward and backward scattering brightness spikes as well as a strong negative polarization branch at large  $\Theta$ . These results are in a good quantitative agreement with (Muinonen et al. 1989). Perfect cubes can depolarize incident light, having the maximum of the depolarization ability at  $\Theta = 165^\circ$ . When the cubes are deformed their depolarization ability rapidly grows. For the deformed cubes the forward and backward scattering spikes are reduced and become wider. The negative polarization branch vanishes. Independent of the parameter  $\delta$  the cubes are able to very effectively transform linear polarization into circular one and vice versa at intermediate angles of scattering (see  $F_{34}/F_{11}$  curves in Fig. 2.20). We note that the  $F_{33}/F_{11}$  curves are similar to the values of  $F_{44}/F_{11}$  ones at all  $\delta$  (except  $\delta = 0.2$ ). Close to the backscattering direction the particles with non-zero  $\delta$  can significantly depolarize light, which initially is circularly polarized.

As has been done for faceted spheres, we studied the scattering angle dependences separately of different scattering orders for cube and its shape deviations. In Fig. 2.21 the component of scattered radiation refracted without internal reflection for particles with shapes randomly deviating from cube is presented at  $n = 1.5$  and  $k = 0$ . For the perfect cubes the refracted component is strongly concentrated in the forward scattering direction. If the particles are far from the ideal cube the refracted component is not zero until  $\Theta = 90^\circ$ . For roughly faceted spheres this limit angle is almost the same (see Fig. 2.10). The forwardly refracted component is negatively polarized. Fig. 2.22 presents single internal reflection at the same conditions. Unlike the case of roughly faceted spheres, for cubes this reflection contributes very slightly to backscattering. On the other hand, the single internal reflection reveals a prominent negative polarization at large  $\Theta$  (see  $-F_{12}/F_{11}$ ). This reflection provides also a very effective transformation of linear polarization to circular and vice versa at moderate  $\Theta$  (curves  $F_{34}/F_{11}$  in Fig. 2.22). Besides, this component is responsible for the strong depolarization at large scattering angles (see curves  $F_{22}/F_{11}$ ) when deformation of cubes increases.

Similar data are shown in Fig. 2.23 for double internal reflection. This component contributes very prominently to the backscattering, especially, when the form of the parti-

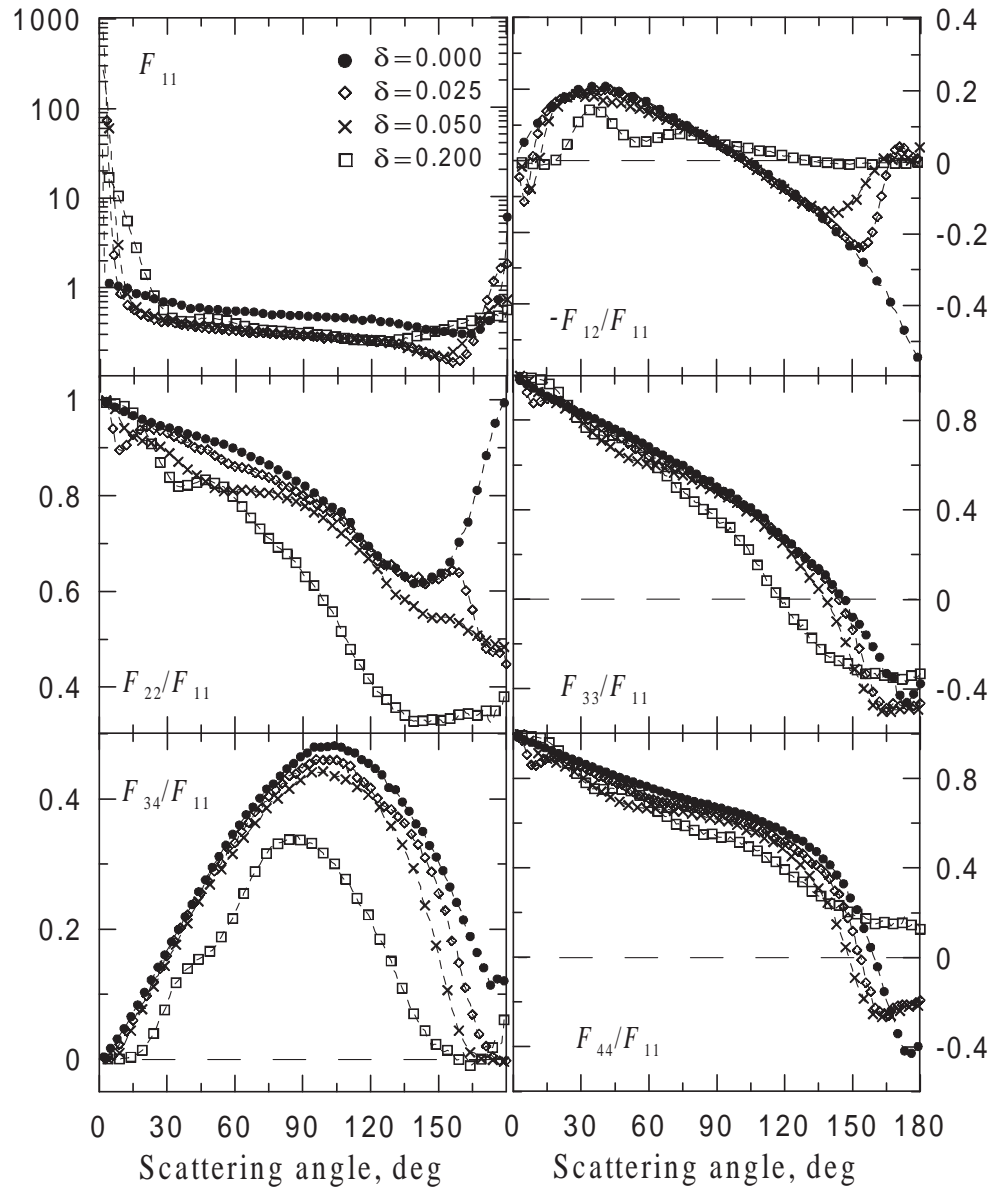


Figure 2.20: The scattering matrix element  $F_{11}$  and ratios  $-F_{12}/F_{11}$ ,  $F_{22}/F_{11}$ ,  $F_{33}/F_{11}$ ,  $F_{34}/F_{11}$ ,  $F_{44}/F_{11}$  versus scattering angle (sums over all significant orders of scattering) for particles with shapes randomly deviating from cube with  $n = 1.5$  and  $k = 0$ .

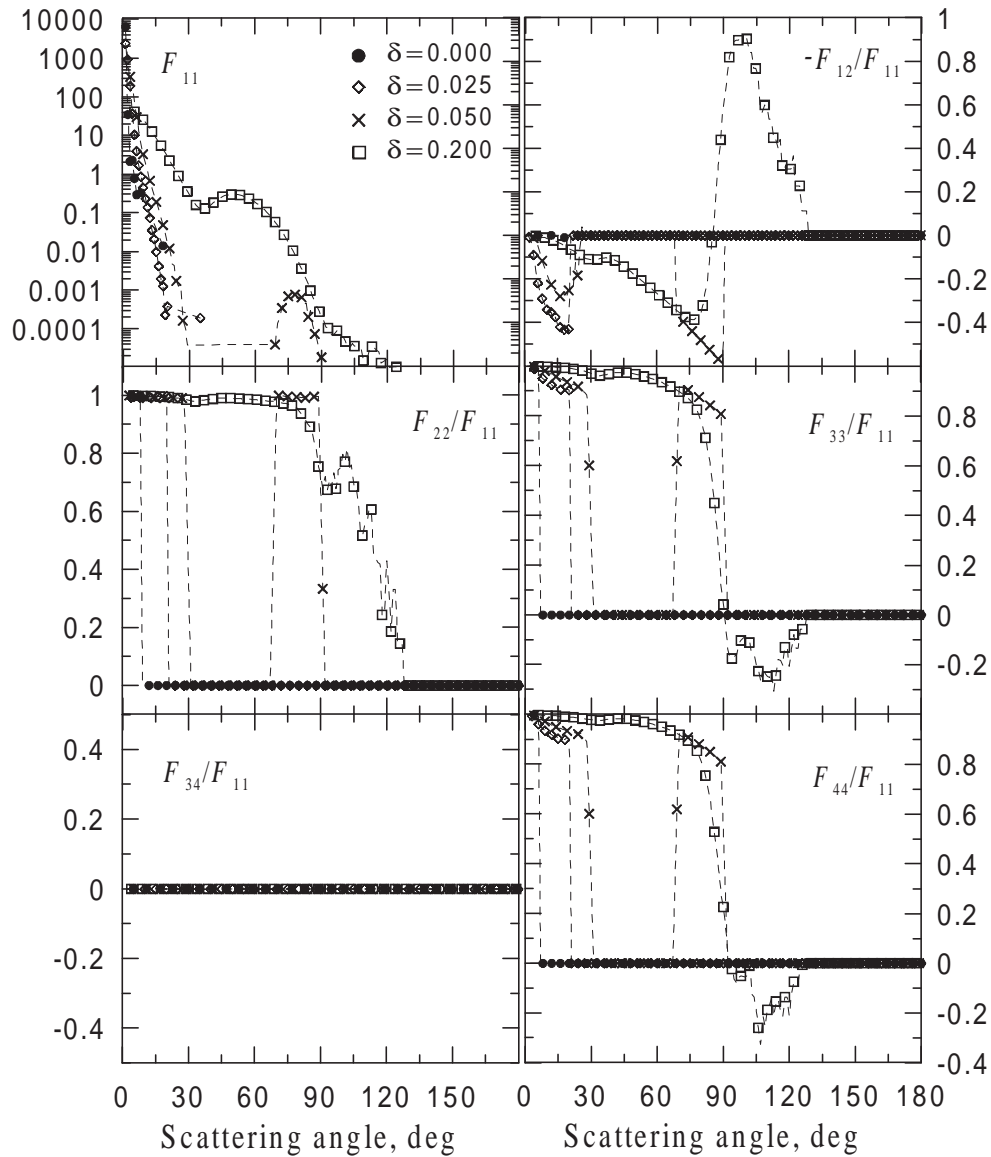


Figure 2.21: The scattering matrix element  $F_{11}$  and ratios  $-F_{12}/F_{11}$ ,  $F_{22}/F_{11}$ ,  $F_{33}/F_{11}$ ,  $F_{34}/F_{11}$ ,  $F_{44}/F_{11}$  versus scattering angle the forwardly refracted component for particles with shapes randomly deviating from cube with  $n = 1.5$  and  $k = 0$ .

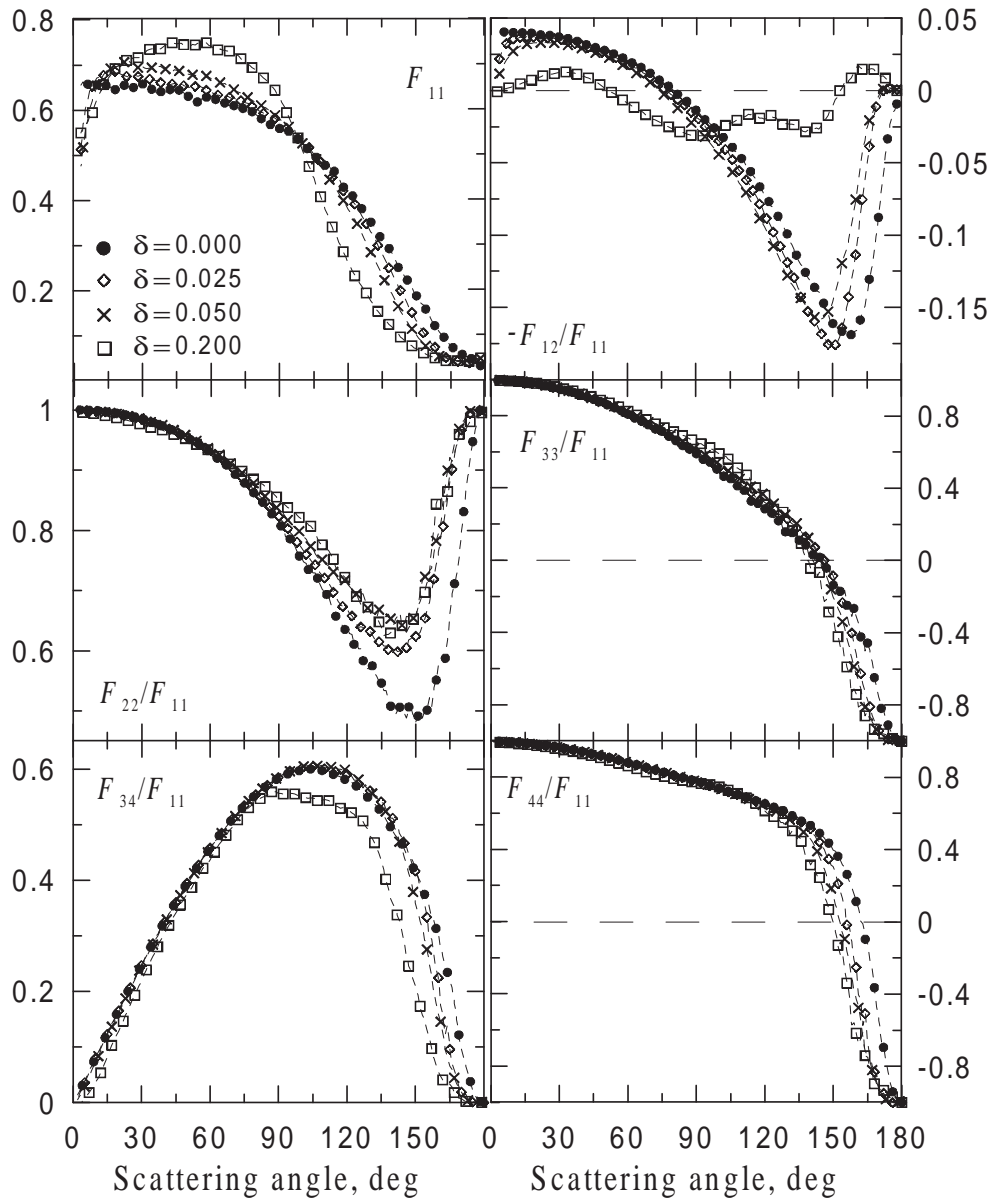


Figure 2.22: The scattering matrix element  $F_{11}$  and ratios  $-F_{12}/F_{11}$ ,  $F_{22}/F_{11}$ ,  $F_{33}/F_{11}$ ,  $F_{34}/F_{11}$ ,  $F_{44}/F_{11}$  versus scattering angle for the component corresponding to single internal reflection for particles with shapes randomly deviating from cube with  $n = 1.5$  and  $k = 0$ .

cles is close to cubic. This is a manifestation of the so-called retro-reflector effect (Trowbridge 1984). The effect is quickly degraded with deviation of particles from cubical shape. This component also contributes very strongly to the negative polarization (curves  $-F_{12}/F_{11}$ ) that is rapidly relaxed with growing  $\delta$ .

Fig. 2.24 presents data for particles with small deviations from cube at different refractive indices  $n$ ,  $\delta = 0.05$ , and  $k = 0$ . As one can anticipate the backscattering effect of such particles increase with increasing  $n$  - transparent particles become good light traps at high values of the refractive index. The particles with small deviations from cubic form

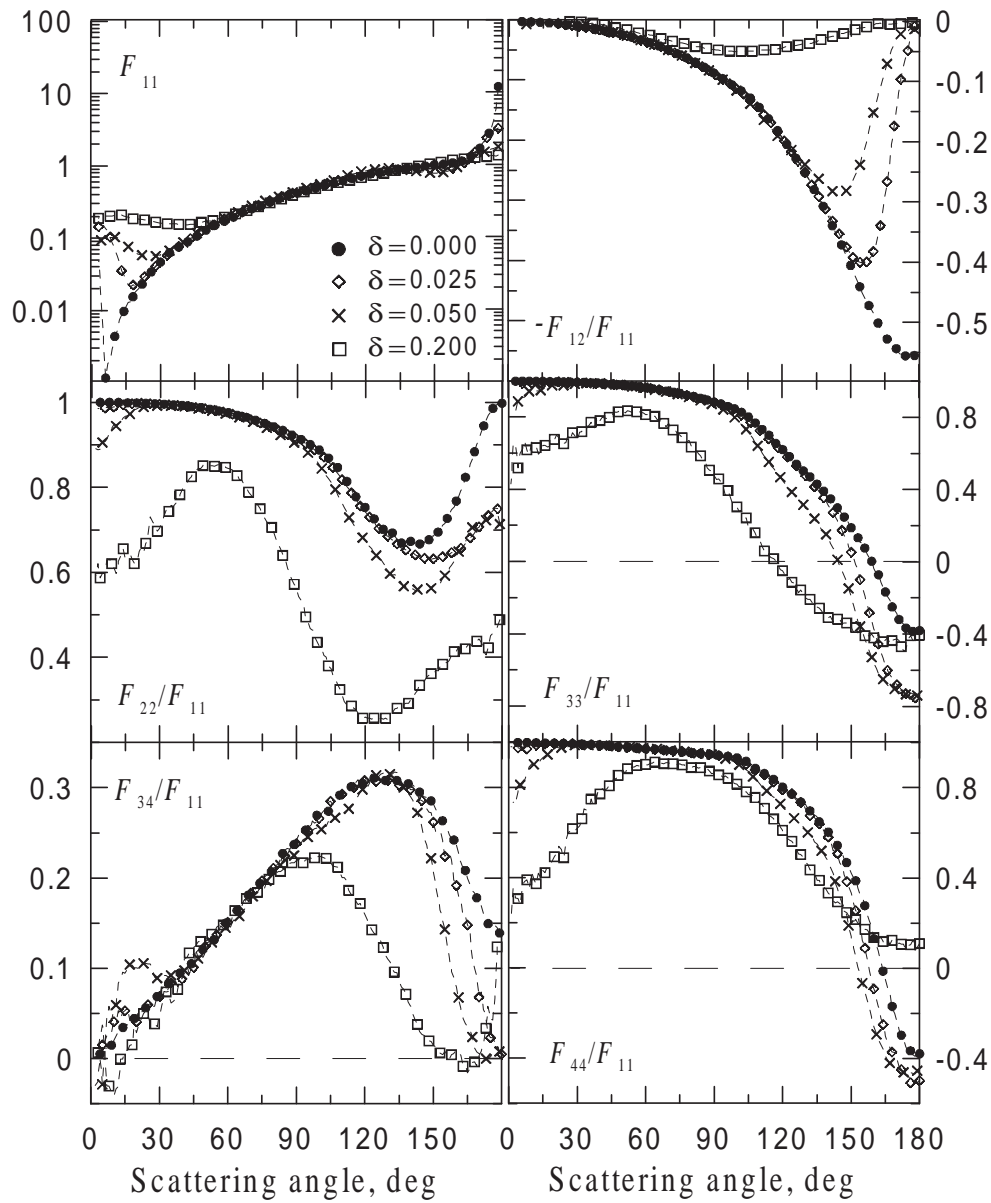


Figure 2.23: The scattering matrix element  $F_{11}$  and ratios  $-F_{12}/F_{11}$ ,  $F_{22}/F_{11}$ ,  $F_{33}/F_{11}$ ,  $F_{34}/F_{11}$ ,  $F_{44}/F_{11}$  versus scattering angle for the component corresponding to double internal reflection for particles with shapes randomly deviating from cube with  $n = 1.5$  and  $k = 0$ .

exhibit an unusual negative polarization branch at large  $\Theta$  (see curves  $-F_{12}/F_{11}$ ) that is strengthened with increasing  $n$ . The branch is unusual, since it goes to the point  $\Theta = 180^\circ$  through a weak surge of positive polarization. Growing  $n$  influences also the forward scattered rays. They become more positively polarized. At  $n = 1.3$  forwardly refracted rays have one more preferred direction of scattering (besides straight forward) from  $30^\circ$  to  $60^\circ$ . These rays are negatively polarized and cause a depression in the correspondent range of polarization curve and different features for other parameters. In Fig. 2.25 the similar data are presented at  $\delta = 0.05$ ,  $n = 1.5$ ,  $L/\lambda = 20$  and different absorption coefficients  $k$ . As one can expect, the increasing  $k$  reduces the backscattering of the particles. At high absorption all the scattered rays tend to be positively polarized (curves  $-F_{12}/F_{11}$ ). The depolarization ability of the particles at large  $\Theta$  (see curves  $F_{22}/F_{11}$ ) decreases with growing  $k$ , as the role of the external reflection, which does not depolarize incident light at all, is enlarged with growth of absorption. In conclusion, we note that for all studied characteristics the roughly faceted spheres and the irregular cube with  $\delta = 0.2$  reveal qualitatively similar dependences on  $\Theta$ , though this similarity is higher for the roughly faceted spheres and ellipsoids with  $d = 4/5$ .

### 2.3.4 RGF particles

Fig. 2.26 shows results of our calculations of the element  $F_{11}$  and ratios  $-F_{12}/F_{11}$ ,  $F_{22}/F_{11}$ ,  $F_{33}/F_{11}$ ,  $F_{34}/F_{11}$  for RGF particles with different degree of non-sphericity  $\beta$  at  $n = 1.5$  and  $k = 0$ ; sums over all main orders of scattering are used. We note that the RGF particles with high  $\beta$  have no backscattering effect. As  $\beta$  grows the maximum of the polarization curve ( $-F_{12}/F_{11}$ ) diminishes; all irregularities are smoothed; the negative branch of polarization in forward scatter direction almost disappears. For perfect spheres the ratio  $F_{22}/F_{11}$  is almost equal to unity at all scattering angles, but for the RGF particles this dependence essentially varies with angle even at small value of  $\beta$ . This means that RGF particles are capable to depolarize light very considerably. The non-spherical shape of particles makes the ratios  $F_{33}/F_{11}$  and  $F_{44}/F_{11}$  unequal, while for spheres they are equal in the whole range of scattering angles. It is interesting to note also that for all parameters scattering angle curves reveal good qualitative resemblance between roughly faceted spheres ( $N = 100$ ) and RGF particles with  $\beta = 18^\circ$ .

Fig. 2.27 shows our data for RGF particles with different  $\beta$  for the forwardly refracted component at  $n = 1.5$  and  $k = 0$ . Rays scattered by more irregular particles penetrate the range of  $\Theta > 90^\circ$  therefore the studied parameters are nonzero in that domain. The similar data for single and double internal reflecting are given in Figs. 2.28 and 2.29, respectively, at the same conditions. For more irregular particles the maximum of intensity ( $F_{11}$ ) of single internal reflecting moves toward smaller  $\Theta$ . This maximum is the remnant of the first rainbow, which is present for particle with  $\beta = 18^\circ$ . The single internal reflecting of the RGF particles demonstrates conspicuous positive polarization in the backscattering lobe; this provides also high depolarization at very small and very large  $\Theta$ . For the double internal reflection for particle with  $\beta = 18^\circ$  the curves of all parameters differ strongly from those for other particles. For instance, at  $\beta = 18^\circ$  the double internal reflection produces only positive polarization, whereas at higher  $\beta$  it gives small negative polarization (see curve  $-F_{12}/F_{11}$  in Fig. 2.29).

Figs. 2.30 and 2.31 present variations of the element  $F_{11}$  and ratios  $-F_{12}/F_{11}$ ,  $F_{22}/F_{11}$ ,

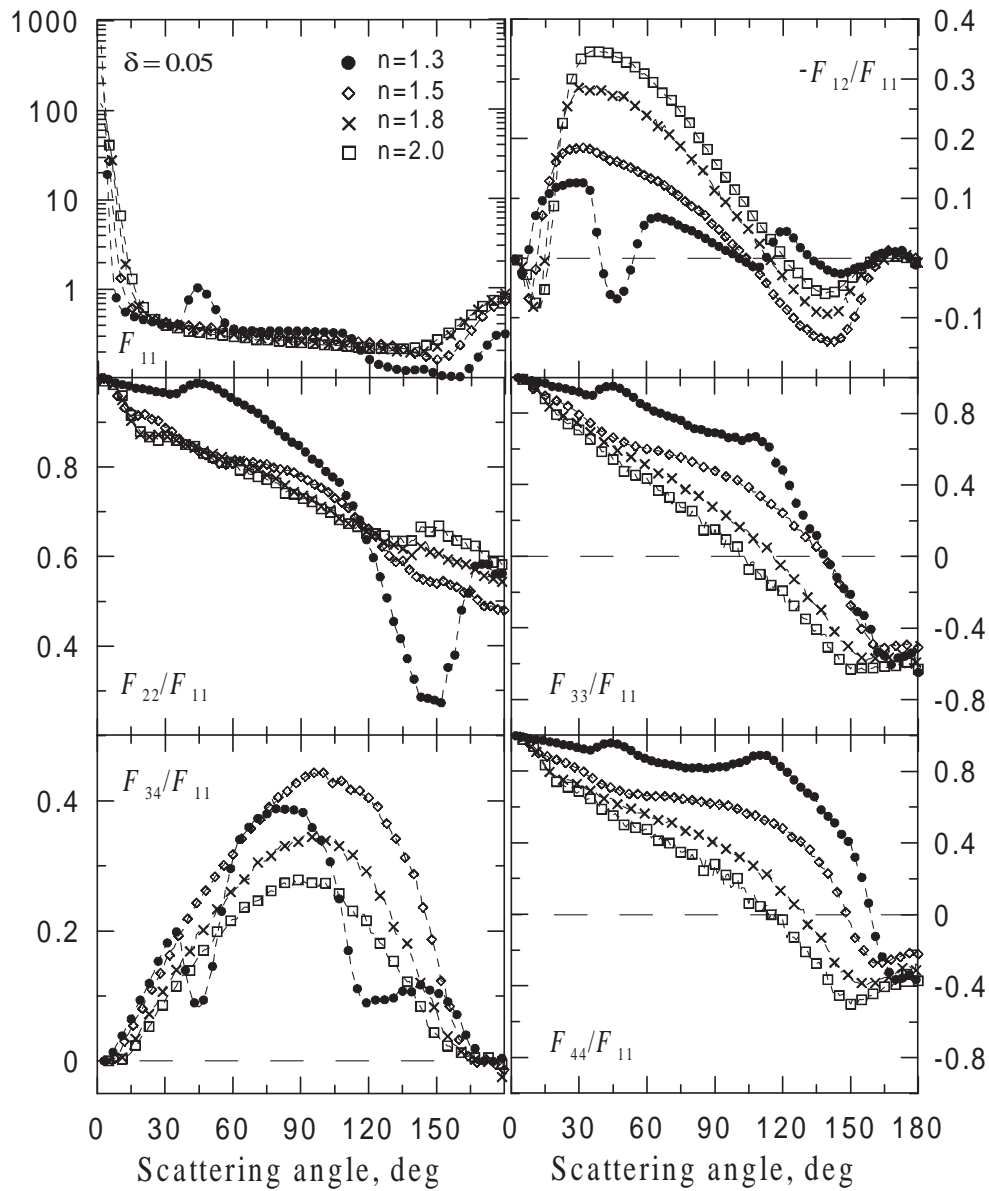


Figure 2.24: The scattering matrix element  $F_{11}$  and ratios  $-F_{12}/F_{11}$ ,  $F_{22}/F_{11}$ ,  $F_{33}/F_{11}$ ,  $F_{34}/F_{11}$ ,  $F_{44}/F_{11}$  versus scattering angle for irregular cubes with different  $n$  at  $k = 0$  and  $\delta = 0.05$ .

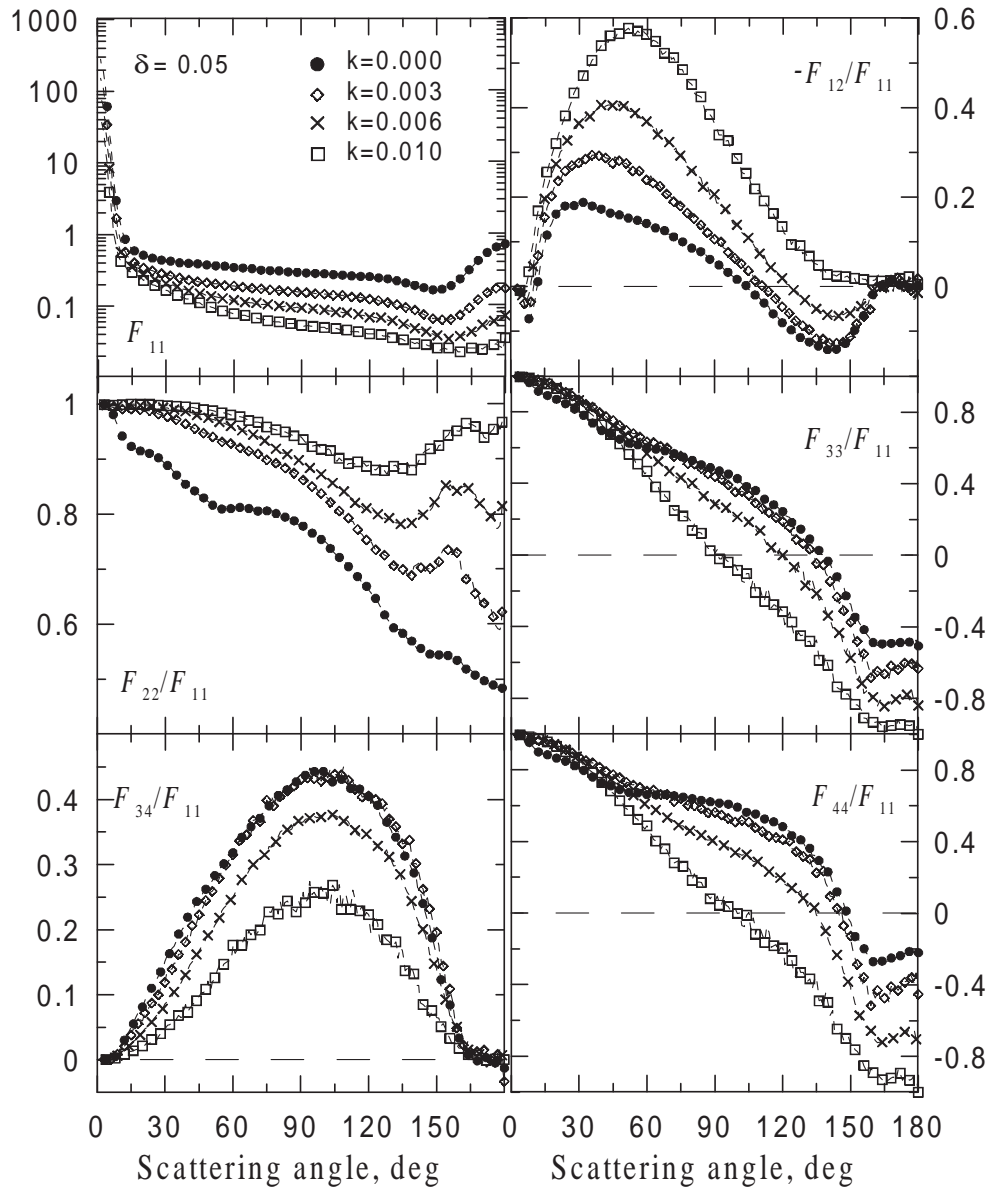


Figure 2.25: The scattering matrix element  $F_{11}$  and ratios  $-F_{12}/F_{11}$ ,  $F_{22}/F_{11}$ ,  $F_{33}/F_{11}$ ,  $F_{34}/F_{11}$ ,  $F_{44}/F_{11}$  versus scattering angle for irregular cubes with different  $k$  at  $n = 1.5$  and  $\delta = 0.05$ . Ratio of the mean ray path length within the particle to the wavelength  $L/\lambda = 20$ .

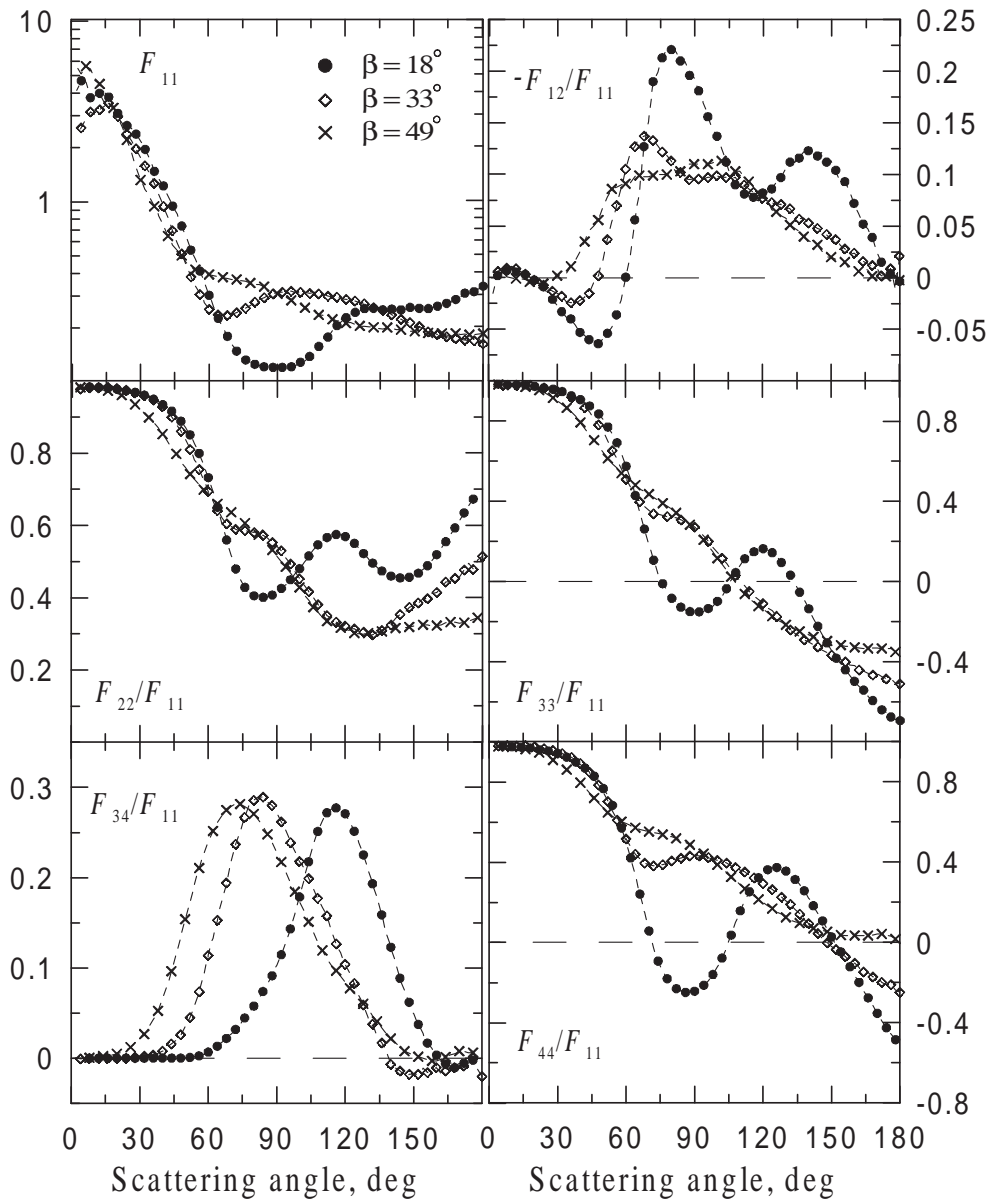


Figure 2.26: The scattering matrix element  $F_{11}$  and ratios  $-F_{12}/F_{11}$ ,  $F_{22}/F_{11}$ ,  $F_{33}/F_{11}$ ,  $F_{34}/F_{11}$ ,  $F_{44}/F_{11}$  versus scattering angle (sums over all significant orders of scattering) for RGF particles with different degree of irregularity  $\beta$  at  $n = 1.5$  and  $k = 0$ .

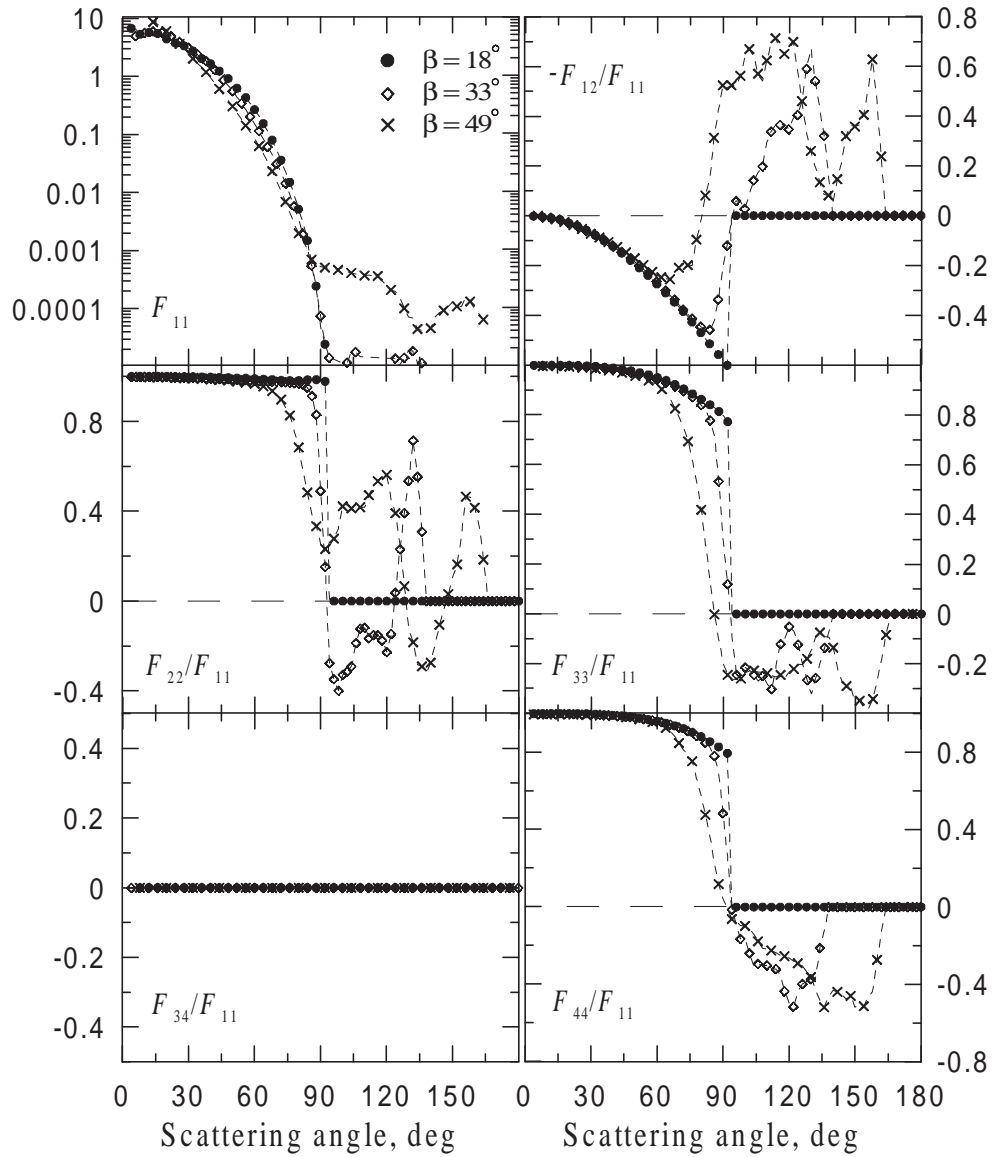


Figure 2.27: The scattering matrix element  $F_{11}$  and ratios  $-F_{12}/F_{11}$ ,  $F_{22}/F_{11}$ ,  $F_{33}/F_{11}$ ,  $F_{34}/F_{11}$ ,  $F_{44}/F_{11}$  versus scattering angle for the refracted component for RGF particles with different degree of irregularity  $\beta$  at  $n = 1.5$  and  $k = 0$ .

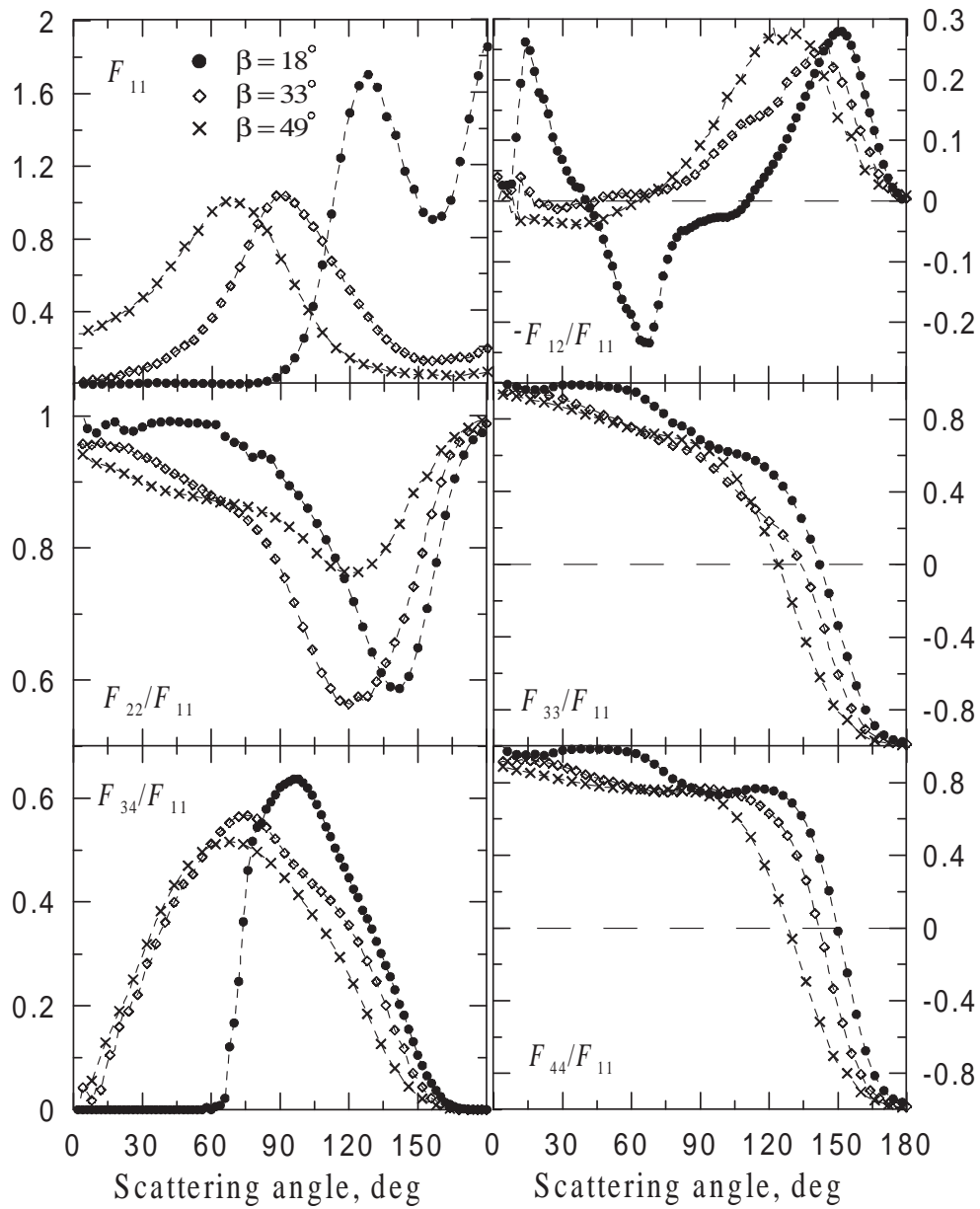


Figure 2.28: The scattering matrix element  $F_{11}$  and ratios  $-F_{12}/F_{11}$ ,  $F_{22}/F_{11}$ ,  $F_{33}/F_{11}$ ,  $F_{34}/F_{11}$ ,  $F_{44}/F_{11}$  versus scattering angle for the component corresponding to single internal reflection for RGF particles with different degree of irregularity  $\beta$  at  $n = 1.5$  and  $k = 0$ .

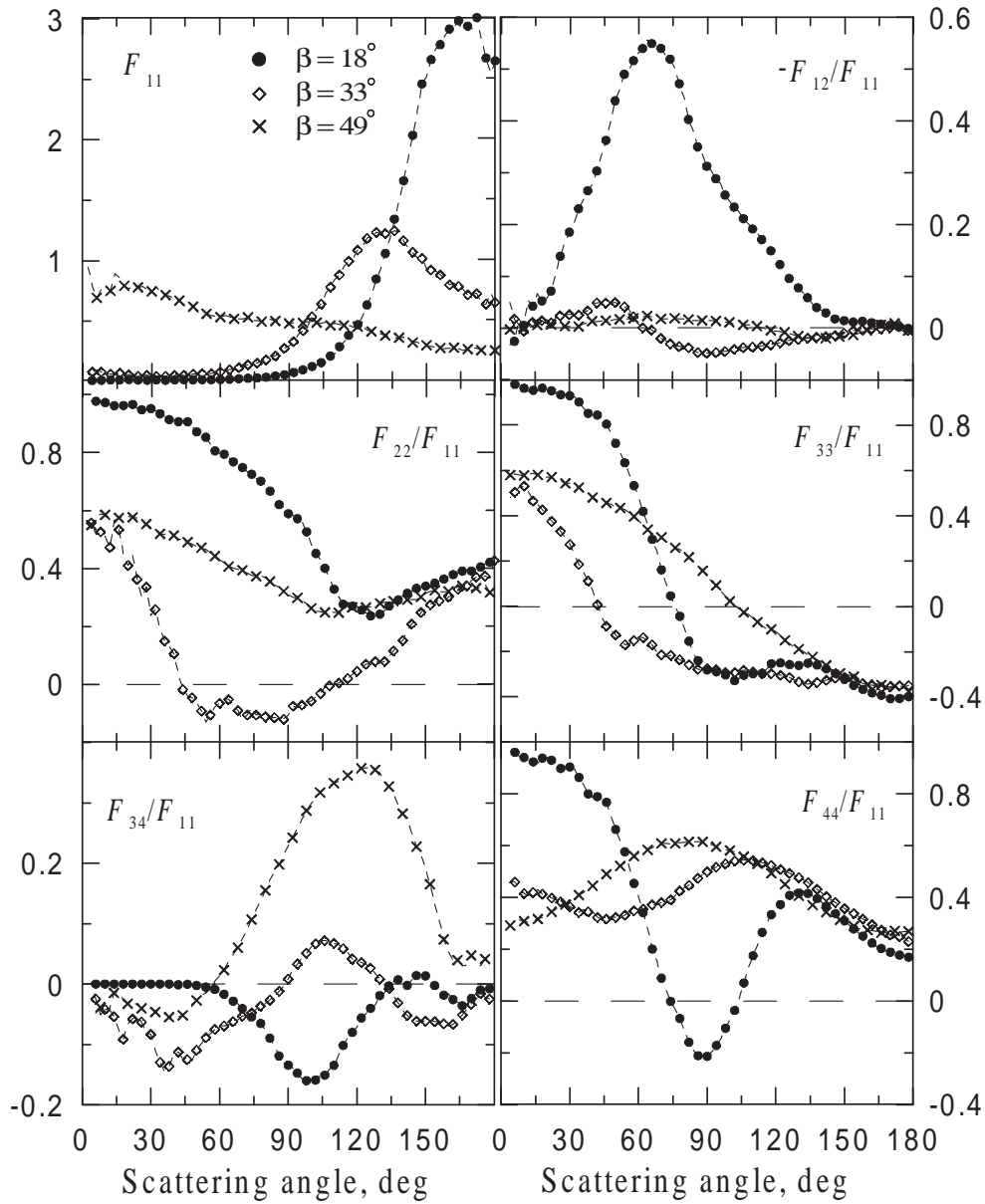


Figure 2.29: The scattering matrix element  $F_{11}$  and ratios  $-F_{12}/F_{11}$ ,  $F_{22}/F_{11}$ ,  $F_{33}/F_{11}$ ,  $F_{34}/F_{11}$ ,  $F_{44}/F_{11}$  versus scattering angle for the component corresponding to double internal reflection for RGF particles with different degree of irregularity  $\beta$  at  $n = 1.5$  and  $k = 0$ .

$F_{33}/F_{11}$ ,  $F_{34}/F_{11}$ ,  $F_{44}/F_{11}$  as functions of scattering angle for RGF particles with different  $n$  and  $k$ . These results were averaged over particle shapes. Growth of  $n$  increases the total reflection of the particle surface. The forwardly refracted rays dominate the forward-reflecting lobe of the intensity indicatrix, which progressively widens and diminishes with growing  $n$ . Decreasing  $n$  produces not only more forward scattering, but also deeper negative polarization branch at scattering angles  $< 50^\circ$ . The effect of absorption is more evident. The intensity of forward-scattered light decreases more slightly with increasing  $k$ , than that for other directions. This is due to the same reason, which was mentioned before: rays transmitted without internal reflections dominate the forward scattering. These rays have the shortest path lengths and hence the highest probability not to be absorbed. Because  $k$  does not equal to zero, the degree of positive polarization grows and the negative polarization branch at small  $\Theta$  disappears (see curves  $-F_{12}/F_{11}$ ). This is explained by the fact that the light externally reflected from the particle becomes a larger fraction of the total scattered light. This is a manifestation of the familiar Umov effect. The same effect we have observed for the faceted spheres (Fig. 2.14) and cubes (Fig. 2.25). It is interesting to note qualitative similarity of all investigated characteristics of the RGF particles and of the roughly faceted spheres (ellipsoids) and irregular cubes with  $\delta = 0.2$ .

### 2.3.5 Spectral properties of particles with different shapes

With our model we can also calculate the spectral characteristics of irregular particles, such as, for example, the wavelength dependence of integral albedo or the asymmetry parameter of the scattering indicatrix.

Integral albedo is defined in the model as the number of rays that emerge from a particle at a given  $\tau = 4\pi lk/\lambda$  divided by the number of rays left the particle at  $\tau = 0$ . Similarly, the asymmetry parameter is the ratio of the numbers of rays scattered by the "average" particle into the forward and backward hemispheres at a given  $\tau$ . All calculations presented in this subsection are averaged over the particle orientations. For the RGF particles additional averaging over samples was carried out. Spherical particles are approximated by two different numbers of facets  $N = 100$  (rough spheres) and  $N = 30000$  (perfect spheres). We consider spheres, cubes, and RGF particles with almost the same characteristic pathlength  $L$ .

In Fig. 2.32 the integral albedo for spheres, cubes and RGF particles calculated by the computer modeling is given as a function of absorption  $\exp(-\tau)$  at  $n = 1.5$  is presented. Although, albedo is a very general parameter, the difference between different shapes is clearly seen. Perfect spheres are brighter than other shapes and RGF particles have the lowest albedo in the whole range of  $\exp(-\tau)$ . The solid line is given for comparison and corresponds to albedo calculated with analytical theory of spectral albedo (Shkuratov et al. 1999). It is a one-dimensional (1-D) light scattering model initially developed for analyzing spectrophotometric properties of the powder-like surfaces (media) consisting of particles large compared with the wavelength. Ray optics approach can be used in this case (see also e.g., Melamed (1963), Hapke (1981, 1993)). The model provides means for estimating the spectral dependence of the absorption coefficient of particles from albedo measurements. As an intermediate result of this theory there is a possibility to calculate absorption dependences of single scattering albedo of large particles. Here we show for comparison 1-D albedo calculated by means of formulas (9a) and (9b) of

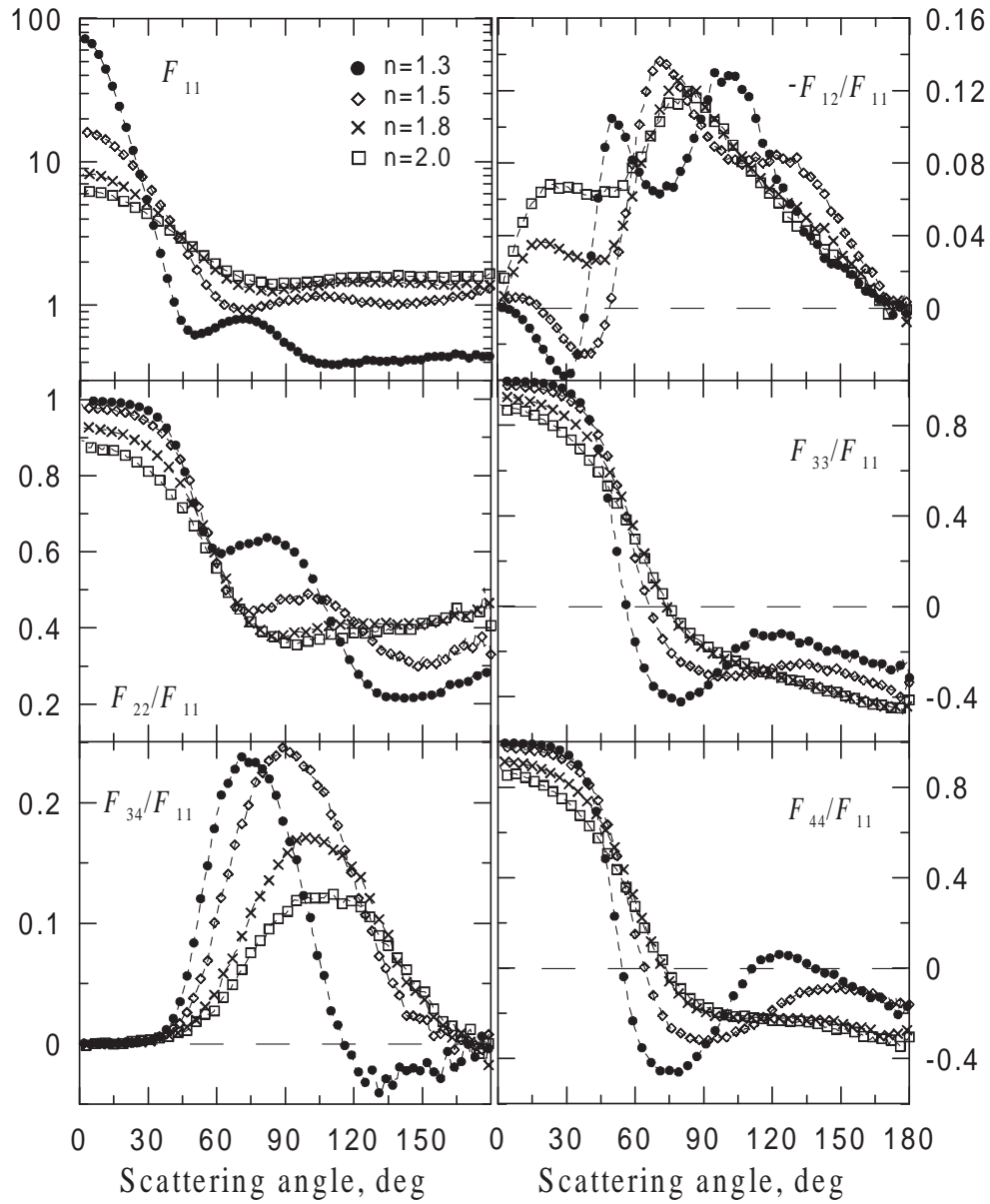


Figure 2.30: The scattering matrix element  $F_{11}$  and ratios  $-F_{12}/F_{11}$ ,  $F_{22}/F_{11}$ ,  $F_{33}/F_{11}$ ,  $F_{34}/F_{11}$ ,  $F_{44}/F_{11}$  versus scattering angle for RGF particles with different  $n$  at  $k = 0$ . Averaging over particle shapes was made.

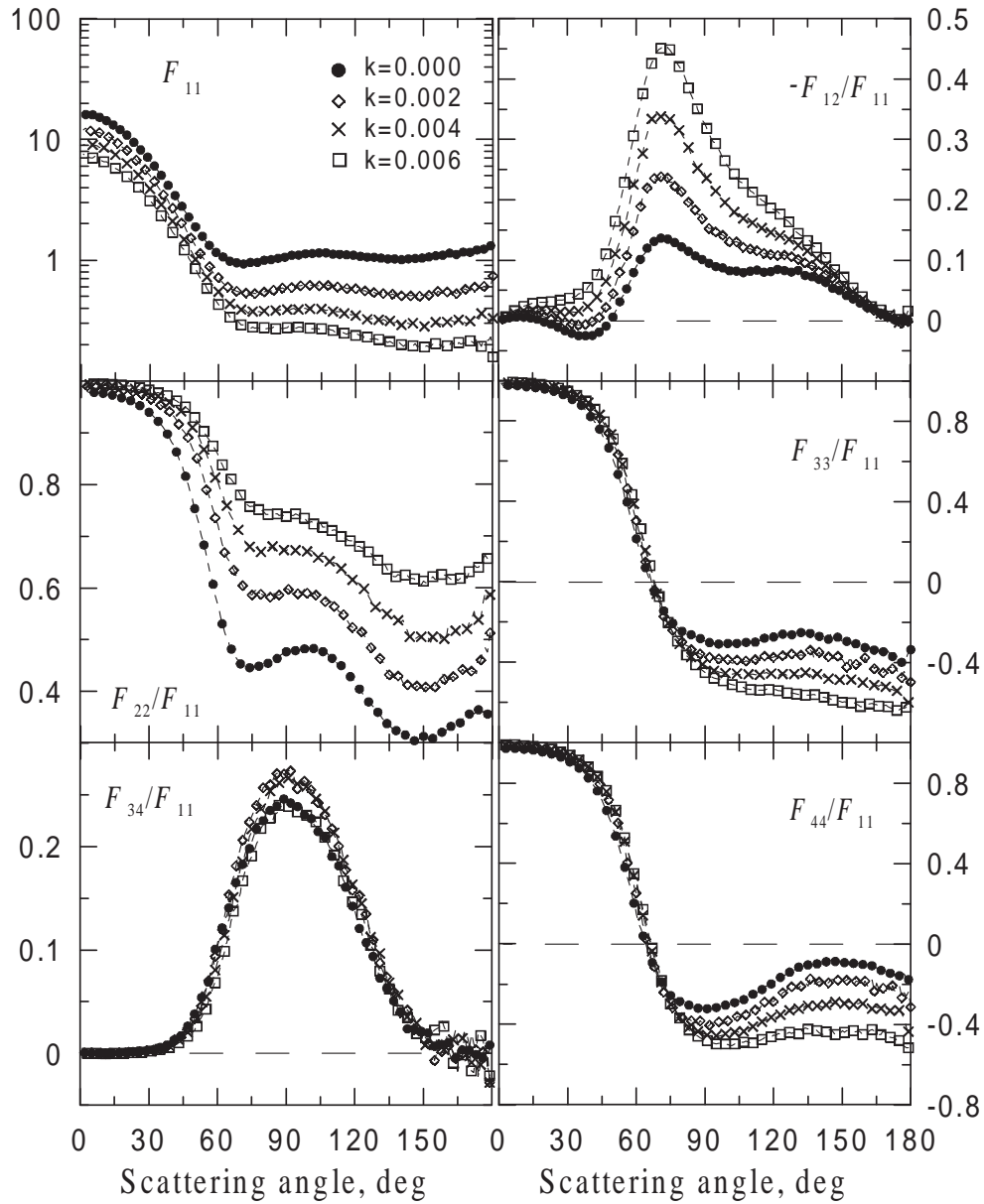


Figure 2.31: The scattering matrix element  $F_{11}$  and ratios  $-F_{12}/F_{11}$ ,  $F_{22}/F_{11}$ ,  $F_{33}/F_{11}$ ,  $F_{34}/F_{11}$ ,  $F_{44}/F_{11}$  versus scattering angle for RGF particles with different  $k$  at  $n = 1.5$ . Ratio of the mean ray path length within the particle to the wavelength  $L/\lambda = 17$ . Averaging over particle shapes was made.

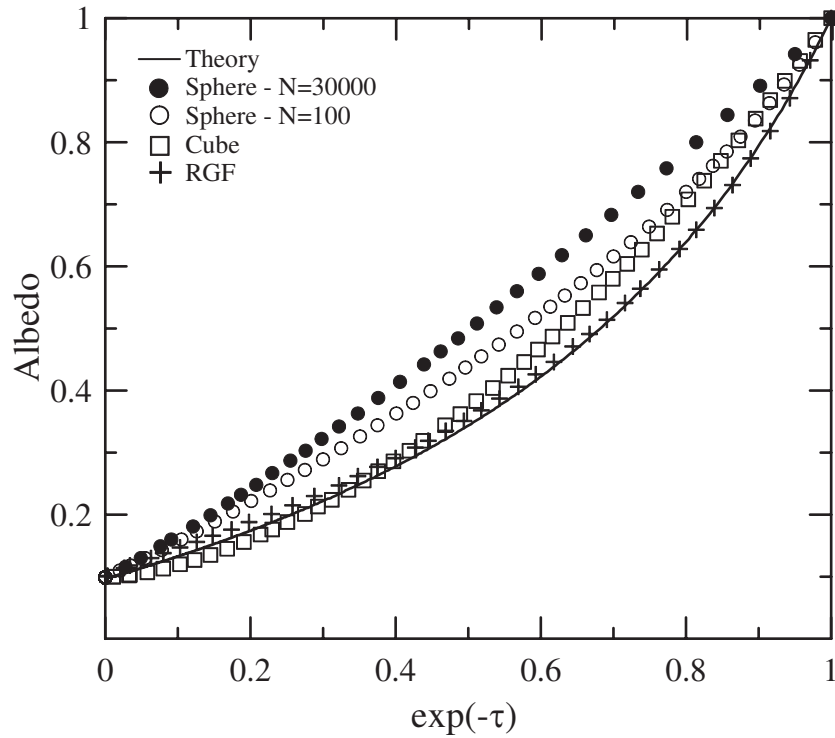


Figure 2.32: The integral albedo of particles with different shapes vs. absorption at  $n = 1.5$ . Comparison with theoretical model Shkuratov et al. (1999) (solid curve).

Shkuratov et al. (1999) (sum of light fractions scattered into forward and backward hemisphere  $r_f + r_b$ ). The analytical curve is most close to the dependence corresponding to RGF particles.

Fig. 2.33 displays the asymmetry parameter of the average indicatrix as a function of  $\exp(-\tau)$ . The curves demonstrate the oblongness of such 1-D indicatrices in forward direction for particles of different shapes. This oblongness is the highest for perfect spheres. Solid curve represents analytical calculation of the asymmetry parameter  $r_f/r_b$  (Shkuratov et al. 1999) and it is closer to the curve corresponding to random irregular particles.

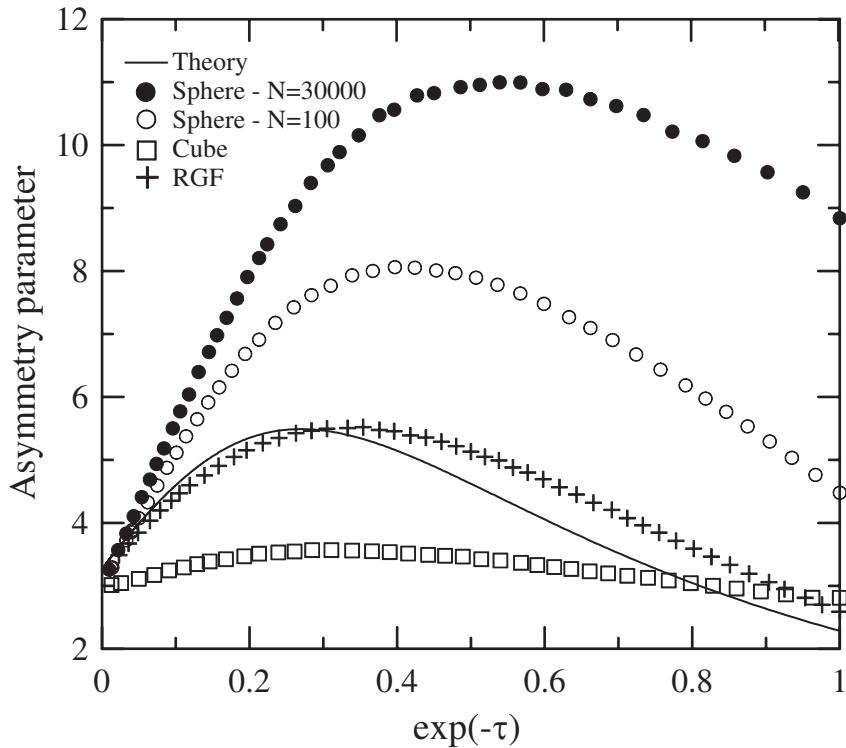


Figure 2.33: The asymmetry parameter of particles with different shapes vs. absorption at  $n = 1.5$ . Comparison with theoretical model Shkuratov et al. (1999) (solid curve).

## 2.4 Conclusions

1. Scattering properties of faceted spheres with number of the facets less than 10000 distinct significantly from those of the perfect spherical particles. The scattering angle dependences of all studied parameters, the element  $F_{11}$  and ratios  $-F_{12}/F_{11}$ ,  $F_{22}/F_{11}$ ,  $F_{33}/F_{11}$ ,  $F_{34}/F_{11}$ ,  $F_{44}/F_{11}$  of roughly faceted spherical particles, e.g., with  $N = 100$ , diverge very much from those of perfect sphere. The irregular particles show, as a rule, smoother curves.

2. For binary contacting spheres the optical properties of individual spheres dominate total scattering, excluding the ratio  $F_{22}/F_{11}$ , when two contiguous spheres due to prominent asymmetry of the aggregate depolarize incident light very noticeably, especially at large  $\Theta$ . Unlike binary spheres, ellipsoids reveal more deviations in scattering properties being compared with spheres.

3. The ideal cube gives forward and backward scattering brightness spikes as well as a strong negative polarization branch at large  $\Theta$ . When the cubes are deformed the spikes are reduced and become wider. The negative polarization branch vanishes. Regardless of the parameter  $\delta$  the cubes are able to effectively transform linear polarization in circular and vice versa at mediate angles of scattering. Near backscattering direction particles with any  $\delta$  can very significantly depolarize light initially being polarized circularly.

4. The RGF particles with high  $\beta$  do not reveal backscattering at all. As  $\beta$  grows the maximum of the polarization curve diminishes; all irregularities are smoothed; the negative branch of polarization in the forward scatter direction almost disappears. The

RGF particles are able to provide strong depolarization.

5. For all classes of particles the degree of positive polarization (actually  $-F_{12}/F_{11}$ ) grows at small  $\Theta$ , if  $k$  increases. This is a manifestation of the Umov effect.

6. There is qualitative similarity of the scattering angle dependences of all investigated characteristics, the element  $F_{11}$  and ratios  $-F_{12}/F_{11}$ ,  $F_{22}/F_{11}$ ,  $F_{33}/F_{11}$ ,  $F_{34}/F_{11}$ ,  $F_{44}/F_{11}$ , of the roughly faceted spheres and ellipsoids, RGF particles, and irregular cubes with  $\delta = 0.2$ . Thus strongly irregular particles of all studied classes reveal much more resemblance in scattering properties, than their perfect representatives.



# 3 SOHO LASCO C3 observations of comets 96P/Machholz 1 and C/2004 F4 Bradfield

Observations of comets 96P/Machholz 1 and Bradfield C/2004 F4 conducted with LASCO C3 coronagraph are presented in this chapter. We determine brightness and polarization from the images of the comets obtained at large phase angles, up to  $167^\circ$  and  $164.5^\circ$  for 96P/Machholz 1 and Bradfield C/2004 F4, respectively. We study the scattering phase functions and dynamics of the dust particles in order to derive their physical properties such as composition and size.

## 3.1 The SOHO spacecraft and LASCO C3 telescope

The Large Angle and Spectrometric Coronagraph (LASCO) instrument is one of 11 instruments operating on the joint ESA/NASA SOHO (Solar and Heliospheric Observatory) spacecraft. The spacecraft was launched in 1995 and was placed in an orbit about the first Lagrangian, or L1, libration point, on the Earth-Sun line where the gravitational attraction of the spacecraft to the Earth is balanced by its attraction to the Sun.

The three coronagraphs comprising LASCO are designated C1, C2 and C3. C1 covers a field from 1.1 to 3.0  $R_\odot$  (solar radii from Sun center), C3 spans the outer corona from about 3.7 to 32  $R_\odot$ , and C2 extends from 2.0 to 6.0  $R_\odot$ , i. e. overlaps with both, C1 and C3 (Brueckner et al. 1995). In this work we have used only C3 data as the comets did not enter the field of view of the other instruments.

Fig. 3.1 illustrates the optical scheme of the C3 telescope. Light enters the front aperture A0. The external occulter D1 shadows the small entrance aperture A1 from direct sunlight. The design of D1 implies decrease of diffraction and reduction of the scattered light falling into the entrance aperture A1.

The primary image is formed by the objective lens O1 in its rear focal plane. The field limit of 32  $R_\odot$  is defined by the field stop. The small internal occulter D2 intercepts the image of the D1 occulter and the light diffracted by D1. This is followed by the large field lens O2 to keep up the field limit. The lens has high relative aperture and therefore consists of a number of elements to minimize aberrations.

The residual aberrations of the O1 lens are controlled by the relay lens O3. It also provides a long working distance in which to install the shutter and the filter and polarizer wheels, while still maintaining a small image that will fit onto the CCD detector. The opaque Lyot spot in front of O3 is meant to intercept a small ghost image of D1 and its

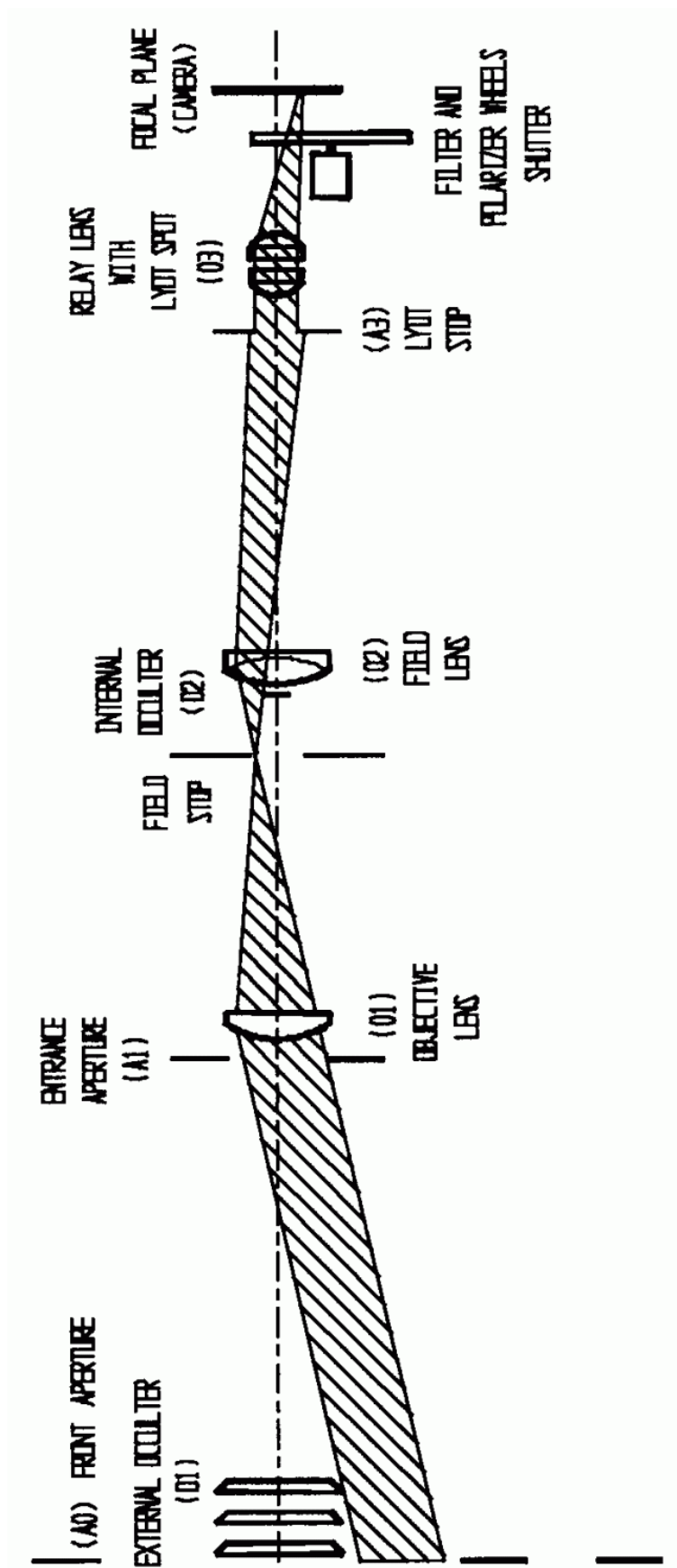


Figure 3.1: Optical scheme of the LASCO C3 coronagraph.

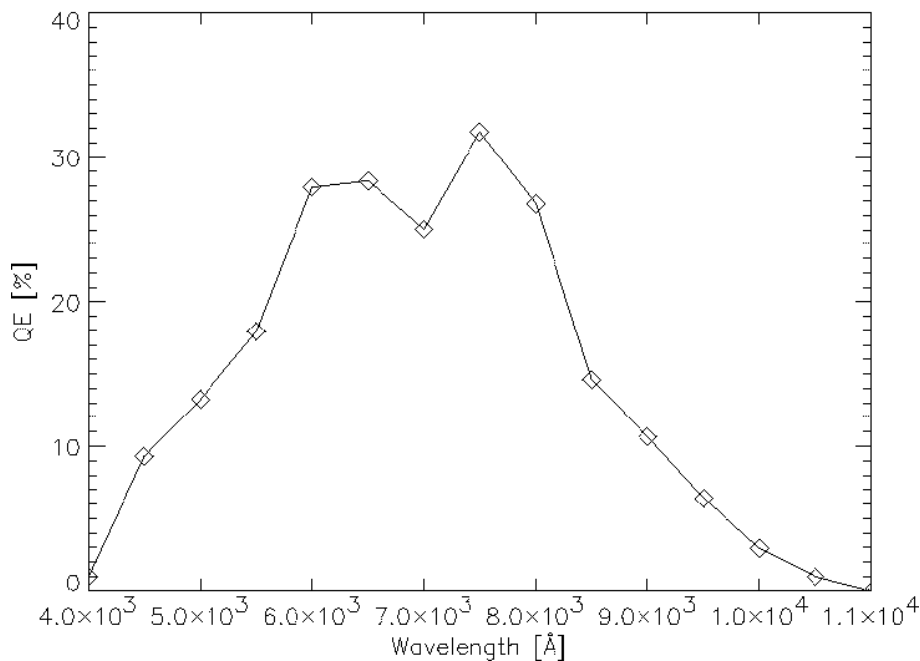


Figure 3.2: LASCO C3 CCD detector quantum efficiency (Cook 1994).

diffraction halo produced by interreflections in the O1 objective lens, a non-negligible potential source of stray light.

The diameter of the entrance aperture is 9.6 mm, the effective focal length of the coronagraph is 77.6 mm and effective f-number is f/9.3. The filter and polarizer wheels are installed in front of the 21.5 mm square 1024x1024 pixel CCD detector. The 21  $\mu\text{m}$  CCD pixel size subtends an angle of 56 arcseconds. The quantum efficiency of the CCD is about 0.1-0.3 in the 500 to 700 nm spectral region (Fig. 3.2). The analog-to-digital converter digitizes analog signal to 14 bits with a quantization step of about 15-20 electrons. The noise of the entire process is less than 10 electrons, so that the entire dynamic range of the system is the full 14 bits, or about 16,000 (Cook 1994).

The CCD square accommodates a  $30 R_{\odot}$  radius image, so that portions of the  $32 R_{\odot}$  optical field of view are lost off the top, bottom, left, and right edges of the CCD surface. The image becomes unvignetted beyond  $10 R_{\odot}$ .

C3 was not designed for narrowband observations and therefore does not have narrowband, spectroscopic quality filters. It has broadband color filters for the purpose of separation of the F from the K corona and polarizers for polarization analysis. The filter wheel contains the blue, orange, deep red, and infrared filters, and a clear glass position. Their bandwidths are indicated in Fig. 3.3. The polarizer wheel contains three polarizers at 120 degrees (their positions are designated as "-60°", "0°", and "+60°"), the H-alpha filter, and a clear glass position. The SOHO mission was interrupted in June 1998, and due to excessive cold the "0°" polarizing filter was damaged. After that the only thing we could do was to use the clear filter to calculate a synthetic "0°" image, according to the technique applied in the polarization routines of the LASCO IDL software library.

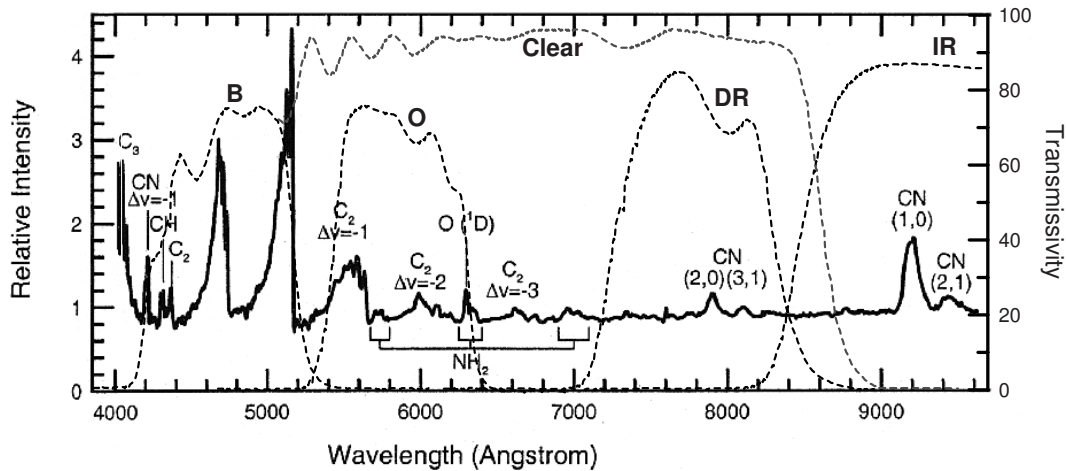


Figure 3.3: C3 color filter data (dashed lines) and a cometary spectrum (solid line). Spectrum of comet 109P/Swift-Tuttle courtesy A. Cochran, Univ. of Texas.

## 3.2 Available SOHO data and the orbits of the two comets

### 3.2.1 96P/Machholz 1

Between January 5 and 10, 2002, comet 96P/Machholz 1 passed through the field of view of the C3 coronagraph (Fig. 3.4). Several sequences of images were obtained at different positions of the filter and polarizer wheels. Four sets of them were suitable for further processing and only two sets could be used to determine the degree of polarization. There is also a long set of images taken with clear glass filter and short exposure where the comet is not oversaturated. The part of the comet orbit covered by the C3 coronagraph is shown in Fig. 3.5. Although the projection of the cometary orbit in the plane of vision appears to be very close to the Sun, the comet is not a sungrazer. Its highly inclined ( $i = 60.18^\circ$ ) orbit has a perihelion distance  $q = 0.1241$  AU, and an eccentricity  $e = 0.96$ . The orbital period is 5.34 years. The comet went through perihelion on January 8, 15 UT. During the period of useful observations from Jan. 8, 08 UT to Jan. 10, 11 UT the phase angle  $\alpha$  of the comet decreased from  $167^\circ$  to  $112^\circ$  and the heliocentric distance increased from 0.124 to 0.152 AU.

For the polarization measurements we also used C3 images of the comet from its apparition in October 1996. At that time the maximum phase angle was  $113^\circ$ . As at that time the corresponding polarizing filter was not yet damaged we had an opportunity to test the  $0^\circ$  image reconstruction procedure.

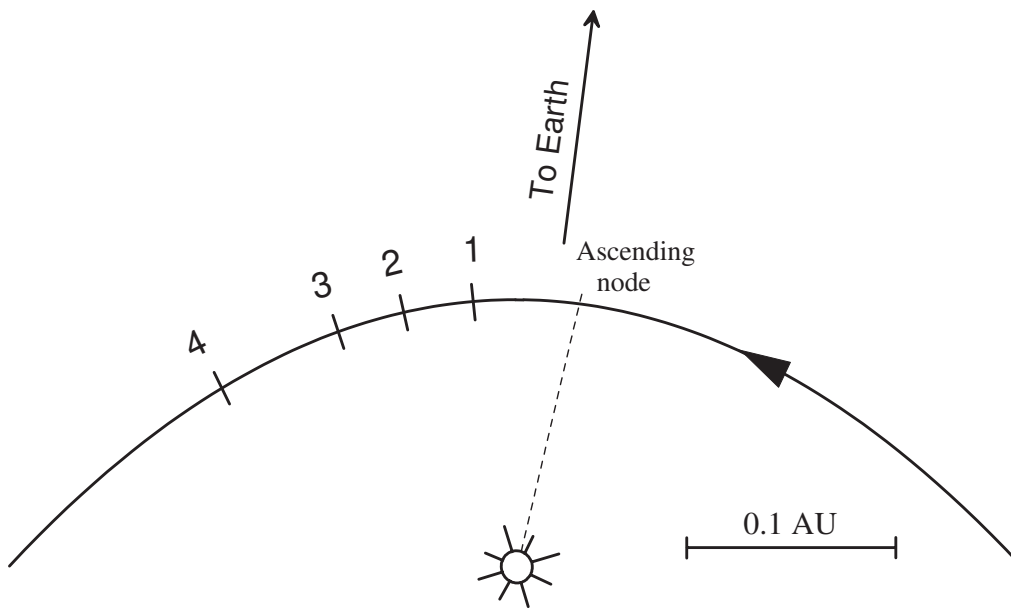
The position of the comet at the time of the exposures is shown in Fig. 3.5.

### 3.2.2 C/2004 F4 Bradfield

Comet C/2004 F4 Bradfield entered the field of the C3 images on April 15, 2004. Its head was followed by a dust tail that ultimately extended fully across the C3 field of view (Fig. 3.6). The comet reached perihelion on April 17, 02 UT and peaked in brightness one day



Figure 3.4: LASCO C3 images of comet 96P/Machholz 1 near perihelion.



**Filter observations:**

1. 2002/01/08 22:00  $\alpha = 157^\circ$
2. 2002/01/09 10:00  $\alpha = 141^\circ$  only intensity
3. 2002/01/09 22:00  $\alpha = 127^\circ$
4. 2002/01/10 10:00  $\alpha = 114^\circ$  only intensity

**Clear glass observations:**

40 images from 2002/01/08  $\alpha = 167^\circ$   
to 2002/01/10  $\alpha = 112^\circ$

Figure 3.5: Comet 69P/Machholz1 orbit near perihelion in 2002.

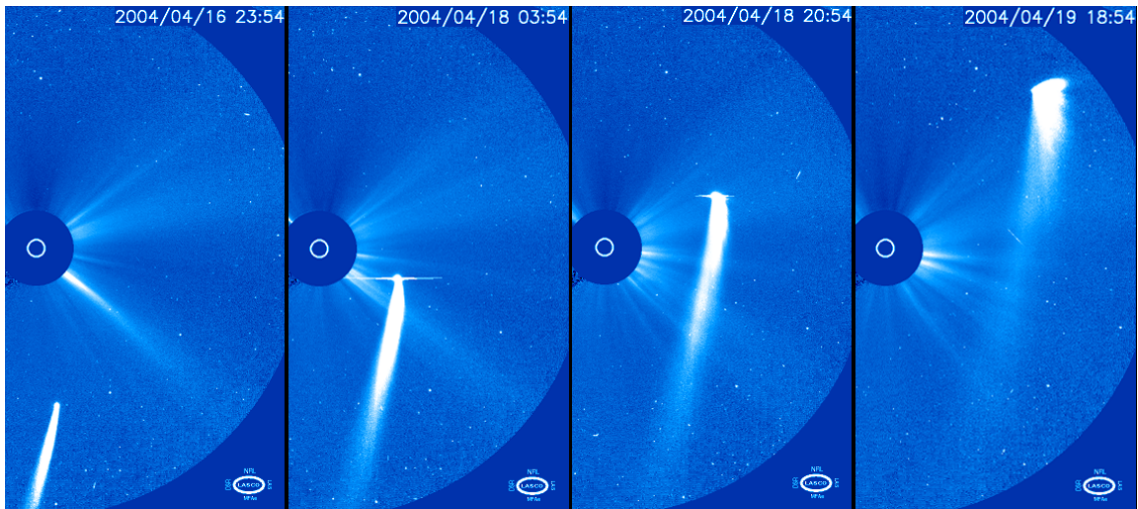


Figure 3.6: LASCO C3 images of comet C/2004 F4 Bradfield near perihelion.

later. On April 20 comet C/2004 F4 left the field of view of C3. During this period more than 700 images were taken in all the filters. The strong increase of brightness of the comet due to forward scattering was expected and the LASCO team corrected the usual exposures taking this into account. Nevertheless on a significant number of image, when the comet approached to its maximum phase angle, the cometary coma was overexposed. The largest number of useful images (around 100, including the moment of maximum brightness) was taken with the blue filter. The least favorable exposures were chosen for the clear glass filter: on most of the images the cometary coma is oversaturated and only 12 images are suitable for measurements. On the few polarization sequences taken the comet appeared to be close to the point of oversaturation. This made polarization measurements impossible as they are very sensitive to the quality of data.

Like the orbit of comet 96P the orbit of this comet is highly inclined ( $i = 63.16^\circ$ ) and has a similar with the perihelion distance of  $q = 0.1683$  AU. But the eccentricity is almost unity  $e = 0.999$  which makes the orbit close to parabolic with a period of 3729 years.

During the observational period the phase angle of the comet changed from  $130^\circ$  to the maximum value  $164.5^\circ$  (April 18, 04 UT) and then decreased down to  $137^\circ$ . The change of geocentric and heliocentric distances versus corresponding phase angles is shown in Fig. 3.7. Arrows indicate the direction of change with time.

### 3.3 Data reduction

We had so-called Level 0.5 images at our disposal (Cook 1994). This is raw data with brightness expressed as CCD detector counts. The database is available at <http://ares.nrl.navy.mil/database.html>. Following the steps realized in the data reduction routines of the LASCO IDL library we subtracted the bias value, corrected for vignetting, and multiplied with the calibration factors (different for different color filters) to translate the data into physical units (mean solar disk brightness). No flatfields were applied to the data. Unfortunately no information about the level of instrumental polarization is available. Thus we do not make such a correction in our analysis, which in principle can give

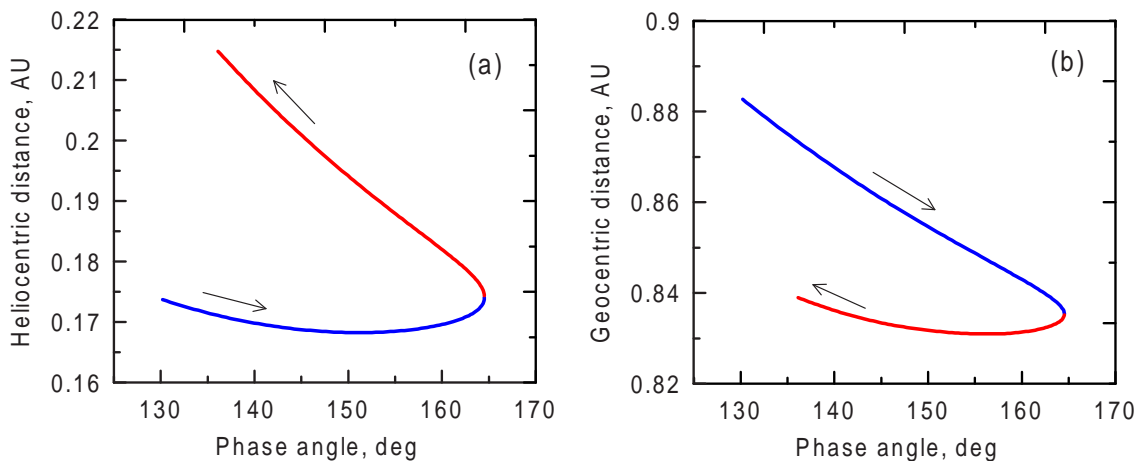


Figure 3.7: The change of the heliocentric (a) and geocentric (b) distances of comet C/2004 F4 Bradfield with phase angle during the period of observations. Arrows indicate the direction of change with time.

noticeable errors.

On some images comet 96P/Machholz 1 appeared very close to the Sun and the bright solar corona was superimposed on the image of the comet. The irradiance of the corona could affect the result of the measurements. In a first step the influence of background was reduced by subtracting two images taken close in time. As the comet moves in the field, if the corona does not change between the two exposures the background would be fully eliminated in this step. To take into account possible changes of the corona between the two exposures, in a second step we marked an area around the comet and constructed an artificial background in this area by means of radial interpolation between the outer and inner sides of the marked area. We decided on radial interpolation because the structures of the solar corona are oriented mainly radially. This artificial background was then subtracted from the image. The remaining unevenness of the background field was of the order of 1% of maximum cometary brightness. Then, in the third step, common for both comets, the comet photometric center (maximum brightness in the cometary image) was searched in each frame and the values of the integrated flux were extracted within a square window of  $3 \times 3$  pixels ( $168 \times 168$  arcsec) centered on the photometric center. We made one measurement of the flux from the comet and 5 additional measurements of the background flux close to the comet. Then we calculated the average value for the background and subtracted it from the comet count. In this way the background subtraction was further improved and, from the standard deviation of the 5 measurements, an estimate of the error in the background determination was obtained. The errors connected with the uncertainty of the background are smaller than the plotting symbols. The main error shown in Figs. 3.8-3.12, 3.16 is caused by the statistical uncertainty of the CCD detector counts. The proximity of some images to oversaturation also introduced uncertainty and provided additional scattering in the data. Unfortunately it is difficult to take this into account or correct. For each data point this error is equal to the square root of the corresponding number of counts multiplied by the CCD quantization step (i.e. the number of electrons per count) expressed in mean solar flux units. We note, however, that the absence of a useful flat field may cause systematic errors.

Up to here the described data reduction applies to photometry as well as polarimetry. Two additional steps were taken to obtain polarization values.

A synthesized image  $I_{0^\circ}$  was calculated with the following formula:

$$I_{0^\circ} = 3 \cdot K \cdot I_{\text{clear}} - I_{-60^\circ} - I_{+60^\circ}, \quad (3.1)$$

where  $K$  is the factor connected with the absorption of light by the polarizing filter ( $K = 0.2526$ ),  $I_{\text{clear}}$  is the clear image, and  $I_{-60^\circ}$  and  $I_{+60^\circ}$  are the images at the corresponding positions of the polarizer wheel.

After calculation of  $I_{0^\circ}$  we had 3 measurements of brightness  $I_{-60^\circ}$ ,  $I_{0^\circ}$ ,  $I_{+60^\circ}$  at 3 polarizer positions. Then the linear polarization  $P$  was deduced by applying the following formula:

$$P = \frac{2 \left[ I_{-60^\circ}(I_{-60^\circ} - I_{0^\circ}) + I_{0^\circ}(I_{0^\circ} - I_{+60^\circ}) + I_{+60^\circ}(I_{+60^\circ} - I_{-60^\circ}) \right]^{1/2}}{(I_{-60^\circ} + I_{0^\circ} + I_{+60^\circ})}. \quad (3.2)$$

In order to test the accuracy of the synthesis procedure one can compare  $I_{0^\circ}$  values measured in 1996 with the ones derived from clear images. We found that the difference in the counts is within the limits of the measurement errors.

## 3.4 Results and discussion

Here we present the results and interpret the measurements of the degree of polarization (96P/Machholz 1 only) and phase function of brightness for both comets. In addition we analyze the dynamics of the dust particles in the tail of C/2004 F4 Bradfield. At first the possible contribution of gas and plasma emissions to the intensity is discussed.

### 3.4.1 Contribution of gas and plasma to our images

In this work we are interested in the optical properties of cometary dust. However, the LASCO C3 filters transmit emissions of cometary gas and plasma as well. Therefore, before we draw conclusions on the optical properties of cometary dust we must discuss the possible presence of cometary gas and plasma. A faint plasma tail is visible on the images of 96P/Machholz 1 taken shortly after minimum elongation of the comet from the Sun where it forms a large angle with the dust tail. Later in the observations the plasma tail merges into the dust tail and therefore cannot be clearly recognized. Close to the cometary nucleus the plasma intensity is nearly constant while the dust intensity is strongly peaked (Bonev and Jockers 1994). Therefore close to the nucleus the plasma contribution can safely be neglected. The radiative lifetimes of the neutral coma molecules scale with the square of the heliocentric distance, i. e. at 0.15 AU the scale length of the  $C_2$  coma,  $\approx 10^5$  km at 1 AU, is reduced to 3000 km, i. e. the gas coma size is  $\approx 6000$  km, much less than the size of 1 pixel of the C3 camera, which amounts to 56 arcsec, i. e. about 35,000 km at the geocentric distance of both studied comets. As the cometary molecules emit fluorescence radiation their scattered radiation is isotropic while the dust scattering is expected to be peaked in the forward scattering direction. Therefore the

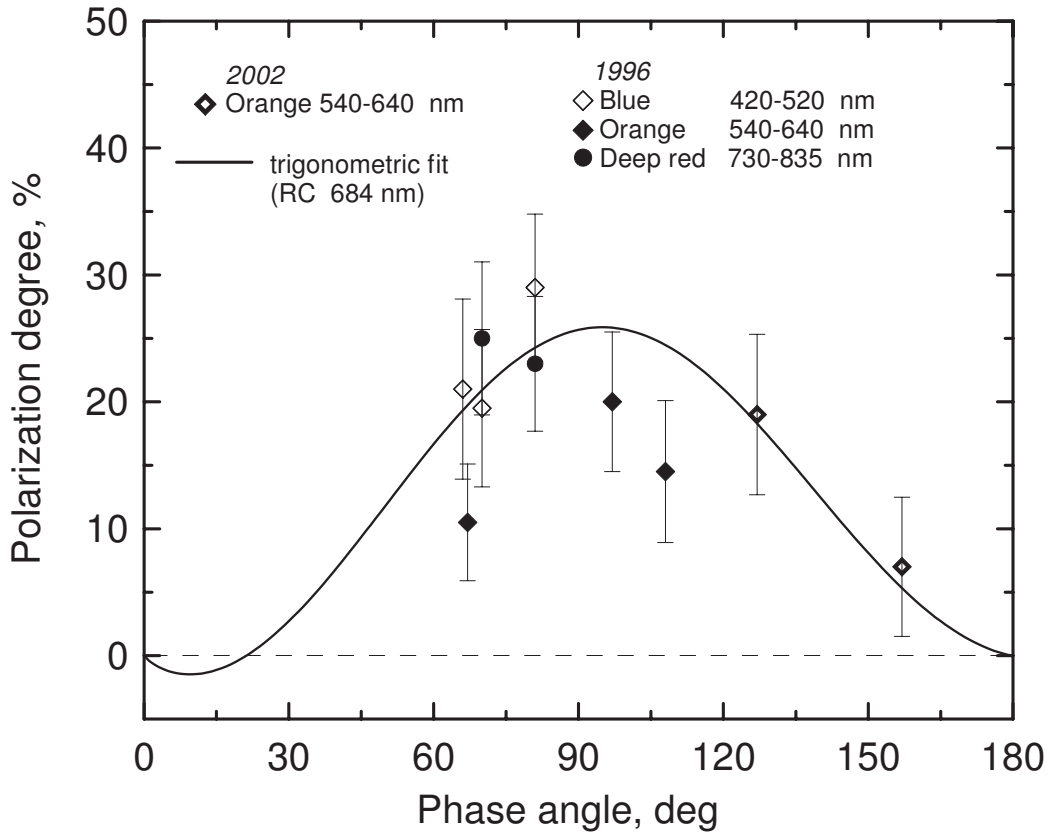


Figure 3.8: Polarization observations of comet 96P/Machholz 1 with different color filters vs. phase angle. The solid curve is a trigonometric fit to the typical cometary dust polarization phase dependence observed at 684 nm.

relative contribution of radiation of the molecules will increase at smaller phase angles. As the very small size of the gas coma fills only a very small fraction of one pixel the measured brightness is most likely dominated by the scattered light from cometary dust.

### 3.4.2 Polarization of comet 96P/Machholz 1

In Fig. 3.8 the results of the polarization measurements for three different filters at two apparitions (1996 and 2002) of comet 96P/Machholz 1 are presented. The error bars in these measurements are mostly due to the uncertainty in the background determination. The solid line represents a trigonometric fit to standard cometary polarimetric data. The curve is computed using the following analytic function:

$$P(\alpha) = b(\sin \alpha)^{c_1} (\cos(\alpha/2))^{c_2} \sin(\alpha - \alpha_0), \quad (3.3)$$

where the free coefficients  $b = 31.72$ ,  $c_1 = 0.815$ ,  $c_2 = 0.408$  and the inversion angle  $\alpha_0 = 21.2^\circ$  are chosen for a typical dusty comet and the red continuum filter RC centered at 684 nm (Kiselev, private communication; for the curve see Kiselev and Velichko (1998)). As one can see, the accuracy of the polarization measurements is unsatisfactory, which

makes further interpretation difficult. In general the measured values follow the standard curve of dust-rich comets, but the orange filter points from 1996, which actually should be of better quality as all three polaroids were functional at that time, deviate noticeably from this trend.

### 3.4.3 Phase function of intensity. 96P/Machholz 1

The cometary brightness depends on heliocentric distance  $r$  and on phase angle. Gehrz and Ney (1992) have presented albedo values  $A$  of comets derived from a comparison of observations in the visual and thermal infrared wavelength ranges. As the phase dependence of the thermal emission of cometary dust grains is expected to be small, the thermal emission of cometary dust is a measure of the dust production and  $f(\alpha) = f_{vis}/f_{IR} = A/(1 - A)$  is proportional to the phase dependence of the brightness. There are no brightness measurements of the studied comets in the thermal infrared during the time of the SOHO observations. Fortunately, during these observations the heliocentric distance changed very little. The difference between the first and the last observation of Machholz 1 is about 0.031 AU. To correct for the small changes in  $r$  we have used observations of comet Machholz 1 from 1986 (Sekanina 1990) and extrapolated Eq. (1) of Sekanina's paper

$$H_{\Delta}(r) = 12.20 + 12.91 \log r + 6.3(\log r)^2,$$

describing the brightness (normalized magnitude) variation of the comet with heliocentric distance, to our near-perihelion case. Note that at the phase angles where the photometric measurements quoted by Sekanina were taken the phase dependence can be neglected. Normalizing Eq. (1) of Sekanina (1990) to 1 at perihelion passage, at the largest heliocentric distance of our data of 0.152 AU we get a correction of the observed brightness by a factor of 1.03. Compared to the large brightness gradient in our data the correction is almost negligible.

In Fig. 3.9 the resulting phase dependence of the flux of 96P/Machholz 1, with the dependence on heliocentric distance reduced to perihelion, is shown in mean solar flux units for the different wavelength bands. The curve for the clear glass filter is presented in Figs. 3.11-3.13. They are calculated from the nominal calibrations of the C3 coronagraph and may not be sufficiently accurate to allow the determination of reddening (i.e. the increase of brightness with wavelength). In what follows we will only make use of the gradient of brightness with respect to phase angle. The curves are compared with a measurement of comets C/1980 Y1 Bradfield (Gehrz and Ney 1992) and C/1975 V1 West (Ney and Merrill 1976), which are the only two comets known to us which were observed at phase angles larger than  $120^{\circ}$ . The quantity  $f_{vis}/f_{IR}$  given in Gehrz and Ney (1992) and Ney and Merrill (1976) was multiplied with arbitrary scale factors to produce a curve close to our measurements of comet 96P. All the curves show a steep decrease of total brightness at large phase angles. At moderate angles the brightness of comet C/1975 V1 continues decreasing with smaller gradient. Whereas the brightness of comet C/1980 Y1 becomes almost constant.

Cometary dust particles have irregular shapes and, probably, complex structures. So one should apply a proper light scattering model, which takes into account the complex structure of the particles. In the forward scattering part of the phase curve the light scattering of particles comparable to the wavelength is dominated by diffraction. However,

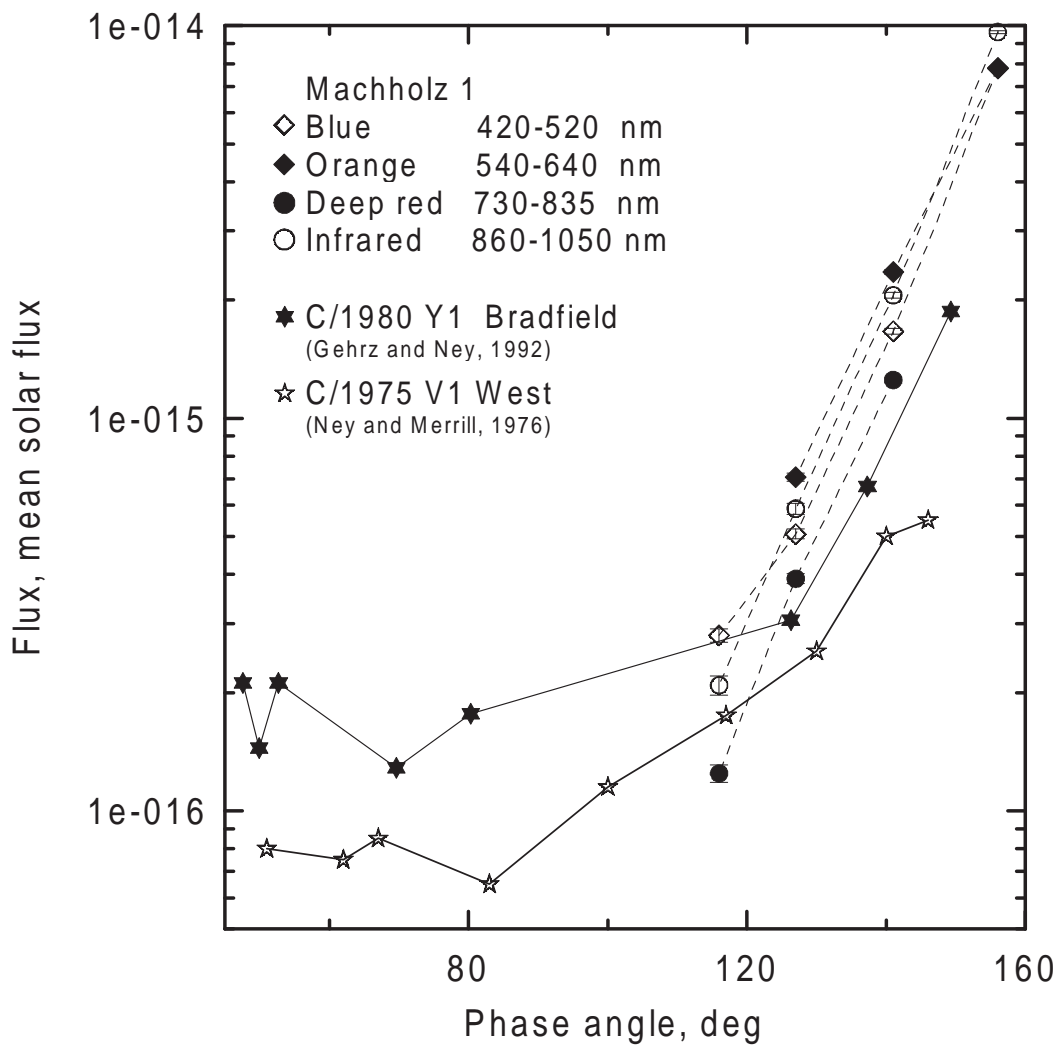


Figure 3.9: Phase curves for comets 69P/Machholz 1 (circles and diamonds) for corresponding color filters, C/1980 Y1 Bradfield (black stars) and C/1975 V1 West (open stars). The values of comets C/1980 Y1 and C/1975 V1 have been adjusted by multiplication with a constant to fit the measurements of comet Machholz 1.

we do not see any evidence for the diffraction spike in the obtained phase curves. The absence of a diffraction spike can be used to obtain a lower limit for the size of the particles, as for particles having a size parameter  $x_{min}$  larger than  $\approx 20$  the first forward scattering diffraction minimum is already  $\geq 167^\circ$ , i. e. beyond the range of the observed phase angles. We can therefore conclude that the particles predominantly contributing to the observed scattered radiation must have a size parameter larger than  $x \approx 20$ , i. e. have a radius larger than  $1 \mu\text{m}$ .

Phase curves of particles with sizes larger than  $1 \mu\text{m}$  have been measured by Weiss-Wrana (1983), Volten et al. (2001) and Rossi et al. (2004). Calculations have been performed by many authors including our ray tracing simulations in chapter 2. Up to now particles larger than the wavelength can only be studied with the T-matrix method and the geometric optics approximation. The first method is more accurate but applicable only to rotationally symmetric particles and has upper size limitations. The second is

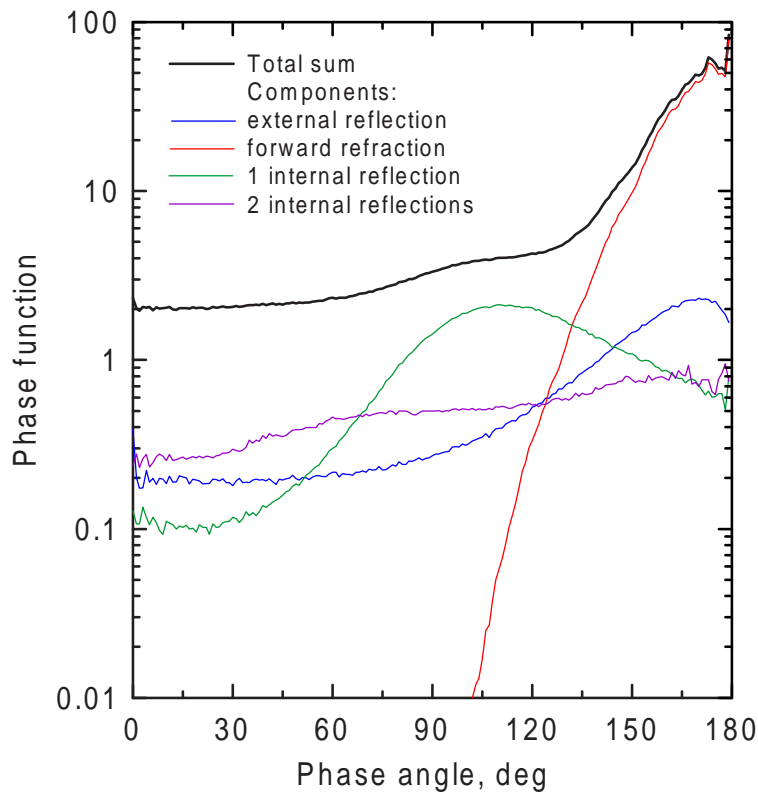


Figure 3.10: Scattering indicatrix calculated for an ensemble of large irregular particles at  $m = 1.5 + 0.0i$  and phase curves for the main components of scattering.

more approximate but can be used for arbitrary sizes and shapes. For particles where both methods can be applied the results agree for size parameters  $x \geq 30 - 60$  (see section 2.2 of this thesis). Calculations using the geometric optics approximation are independent of particle size if the particles are nonabsorbing. The gradient of the phase curves of such particles strongly increases with decreasing real part of the refractive index (Figs. 2.13, 2.30). A weaker dependence exists for rising imaginary part of the refractive index (Fig. 2.31). According to the results of our light scattering simulations, as compared to the backscattering part, the forward scattering part of the phase function is much less dependent on particle shape. In Nousiainen et al. (2003) the data of experimental measurements of an ensemble of irregular particles with broad size distribution are compared with Mie theory. The theoretical phase curve fits well the experimental one at phase angles  $> 120^\circ$ . This is because the forward scattering slope, at least for larger particle sizes, is formed mostly by rays transmitted by the particle without any further interaction. Fig. 3.10 demonstrates this. Therefore in this phase angle domain phase functions for spheres and irregular particles behave in a similar way (see also Weiss-Wrana (1983)). Thus we can apply Mie theory to extract the complex refractive index  $m = n + ik$  from the measured brightness gradient. We note that many experimental and theoretical papers prove that Mie theory is not applicable at backscattering and it cannot adequately reproduce the angular dependence of polarization of light scattered by irregular particles.

Presently the size distribution of dust grains in comets is a matter of debate (see e.g. Jockers (1997)). Space observations of Halley's comet (Mazets et al. 1986) have revealed

particle size distributions of the particle fluences  $dn = r^{-a} dr$ , where  $dn$  is the number of dust grains in a small interval around radius  $r$ , and  $a$  is the power index. For the small submicron particles the space observations power indices  $a \approx 2$  which increase to  $\approx 3$  and more with increasing size. But for the large particles of interest here the statistics are poor and, worse, because of the high encounter speed at comet Halley no good calibrations of the measuring device were available. Also it is not clear if comet Halley is representative for all comets or at least for comet Machholz 1. Additional information comes from models (mostly by Fulle and coworkers) of dust tails of a number of comets based on the radiation pressure force. Power indices of dust production are provided in Table II of Jockers (1997). In a more recent paper (Fulle et al. 2000) the particle data as well as the optical data on comet Halley obtained by the Giotto probe are combined into a similar radiation pressure model and a power index of 2.7 is derived. Because we are interested here in fluences along the line of sight we must correct the power indices of dust production for the fact that smaller particles have larger emission speeds. After correction these power indices are lowered by a number between 0 and 0.5, i. e. become significantly less than 3.

Using Mie theory we have performed calculations of the phase functions for  $a = 2.5$ . In our calculations we restricted the range of size parameter  $x$  between 10 and 400, since the presence of smaller and larger particles influences the result very little. The number of large particles decreases according to the distribution law. On the other hand, small particles do not have a high enough scattering efficiency to make a significant contribution to the phase function behavior at  $a = 2.5$ . Besides, they introduce a noticeable wavelength dependence of the scattering, which is absent in our data (see Fig. 3.9).

In order to determine the real and imaginary part of the refractive index  $m = n + ik$  we proceeded as follows. For four fixed values of  $n$  we determined the best fit absorption indices  $k$ . In Fig. 3.11 one can see that the best fit refractive indices  $m$  produce gradients close to the observed phase curve (clear glass filter). Higher refraction is coupled with lower absorption and vice versa. The best coincidence corresponds to  $m = 1.2 + i0.004$ . Higher and lower values of  $n$  give certain deviations from the measurements at all  $k$ . Then we tried to find the maximum possible  $k$  at  $n = 1.2$ . Fig. 3.12 shows that the increase of the absorption index in the very wide range from  $k = 0.001$  to 0.1 leads to small changes in the phase dependence, keeping the same gradient in the given limits of the phase angles.

To make the calculations more adequate we applied our GO model and took into account the irregular shape of particles for large size parameters. In Fig. 3.13 we present fit curves calculated in the following way. Taking the same limits of the size distribution we used Mie theory for size parameters  $x < 50$  and geometric optics approximation with RGF particles for  $x > 50$ . Then Mie and GO phase functions were summed with weighting coefficients corresponding to the integral projected areas of small and large particles. The figure shows that even with improved modeling we remain in the same domain of complex refractive indices.

Theoretical consideration of particles with homogeneous structure gives unrealistically low values for the real part of refractive index. As all conceivable constituent minerals of cometary dust have higher refractive indices we assume that the particles are not single homogeneous grains, but porous aggregates of smaller grains. The calculated values of the complex refractive index are considered as an “effective” refractive index  $m_{eff} = n_{eff} + ik_{eff}$  in terms of effective medium theory and the porosity  $P$  is introduced as an

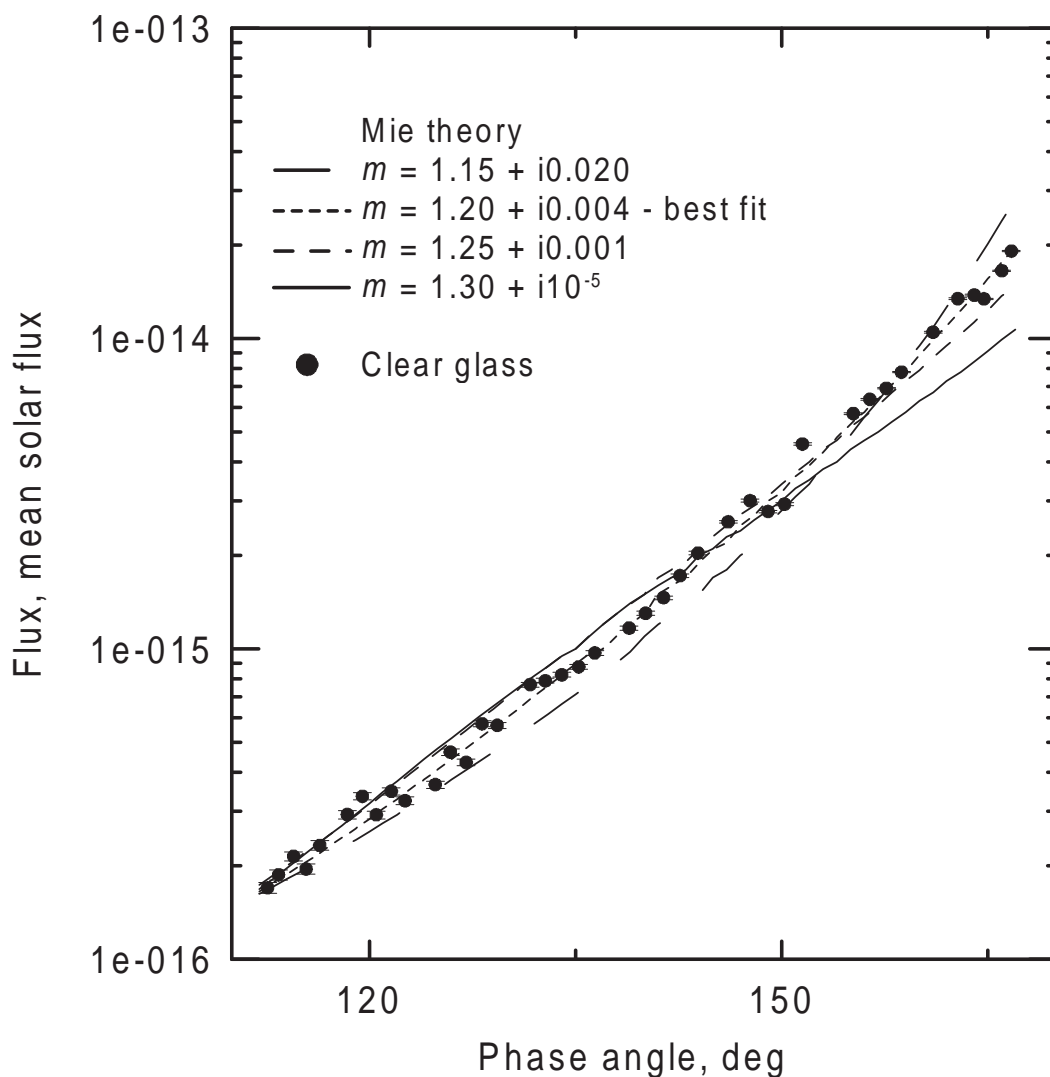


Figure 3.11: Theoretical best fit curves for the clear glass measurements at four combinations of  $n$  and  $k$ .

additional free parameter. The case of grains composed of a single porous material can be treated with the Maxwell-Garnett (Bohren and Huffman 1983) and Bruggeman (Bruggeman 1935) formulae taking vacuum ( $m = 1$ ) as the "host" material and filled subvolumes as the "inclusion". Both formulae provide practically equal results. For example, a porosity rate  $P = 0.5$  changes the value of the complex refractive index from  $m = 1.2 + i0.004$  to  $m = 1.43 + i0.009$ .

Corrigan et al. (1997) found that interplanetary dust particles, which can perhaps serve as examples for cometary particles, have a porosity which very rarely exceeds  $P = 0.3$ . The maximum real part of the complex refractive index that we can obtain with  $P \leq 0.5$  using a mixing rule is around  $n = 1.65$ , but in this case the particles must be very transparent. The derived range of possible values of  $n$  together with conditions of transparency and porosity corresponds to porous glassy silicates (Padmavati and Hanner 1999). In order to fit the data using higher absorption of the dust particles one must assume either a higher porosity rate, which seems to be unlikely, or an unrealistically low

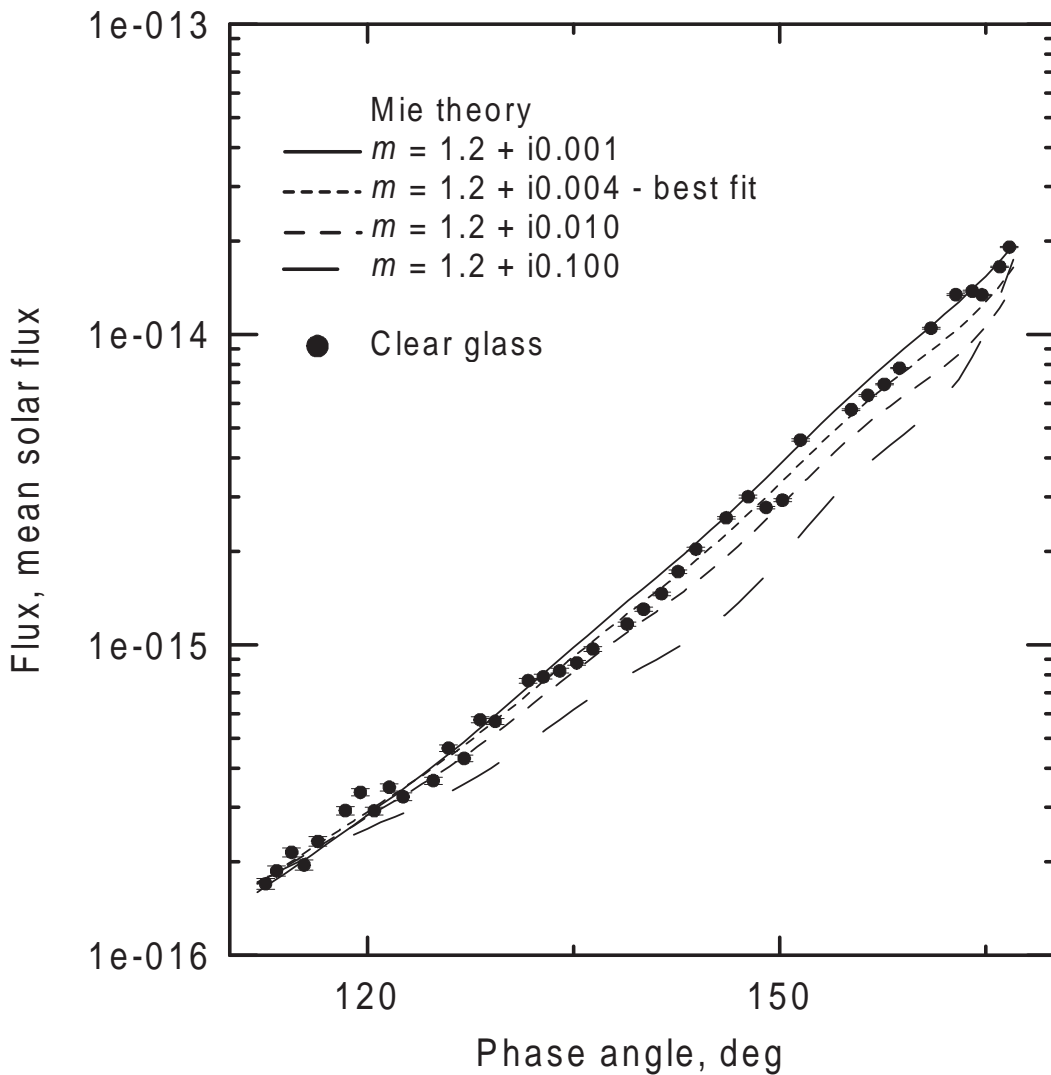


Figure 3.12: Dependence of the phase function on the absorption index at  $n = 1.2$ .

real part of the refractive index.

Water ice has a refractive index  $n$  of  $\approx 1.3$  and therefore may seem well suited to explain the refractive index derived in our models. Water ice has been detected by the ISO spacecraft in comet C/1995 O1 (Hale-Bopp) at heliocentric distances  $r \geq 2.9$  AU by Lellouch et al. (1998) but is very unlikely to be present at  $r \leq 0.16$  AU (Hanner (1981)).

#### 3.4.4 Phase function of intensity. C/2004 F4 Bradfield

At first, we will consider the light curve of comet C/2004 F4 Bradfield which is shown in Fig. 3.14. We present in this figure the measurements made in two filters blue and orange only, as they cover the period of observations better than the measurements in other filters. The brightness of the comet rapidly grows with time reaching maximum at maximal phase angle and then decreases a bit slower. This fact proves once more that the brightness behavior is determined mostly by the angular dependence of light scattering by the dust particles. There is also a small local maximum, which took place on Apr. 16.

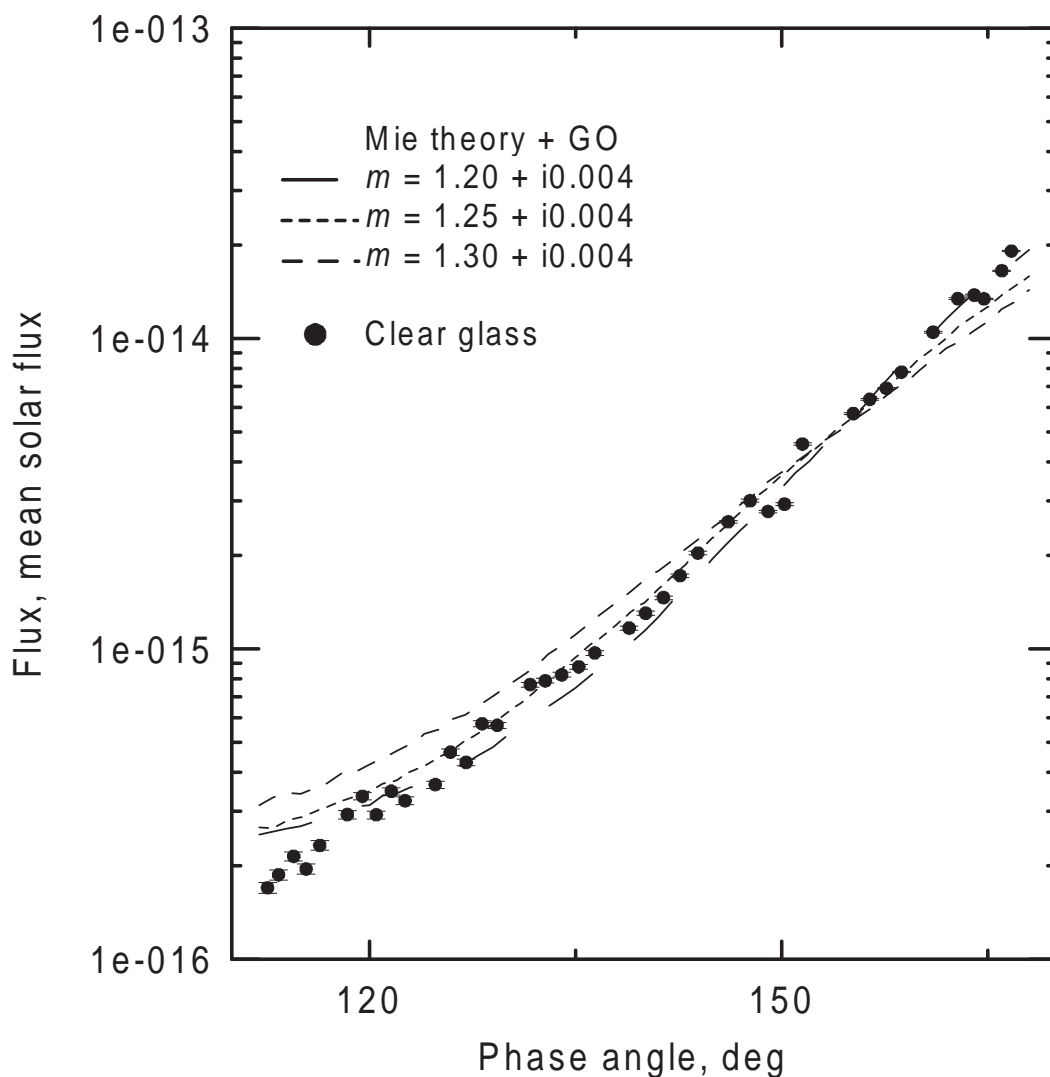


Figure 3.13: Theoretical fit curves for the clear glass measurements at different values of  $n$  and  $k = 0.004$ . Mie theory calculations for particles with size parameters  $x < 50$  are combined with GO calculations for irregular (RGF) particles with  $x > 50$ .

A possible reason for its appearance we will discuss below. After the moment of global maximum the brightness of the comet monotonously decreases.

The LASCO team probably did not expect such a growth of brightness. Between Apr. 17 and Apr. 18 almost all images taken at that time are overexposed. After this, corrections were made and the situation improved. Measurements on Apr. 18 give reasonable values of brightness, although a detailed analysis shows that the brightest part of the cometary images appears to be near the point of oversaturation. This makes the reliability of these measurements doubtful. Only after the middle of Apr. 18 the exposure time is appropriate.

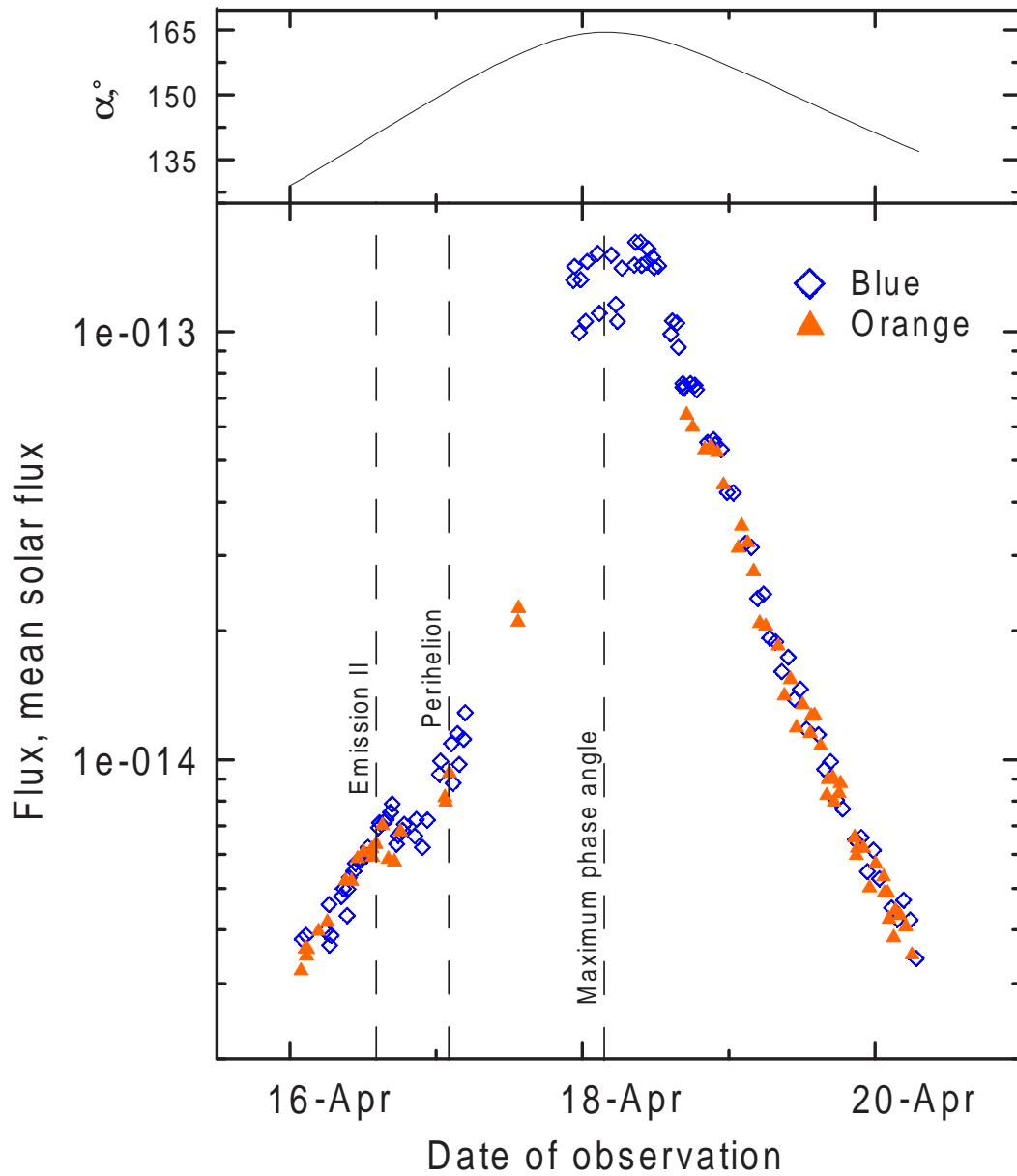


Figure 3.14: Light curve of comet C/2004 F4 Bradfield for two color filters. The values of comet's phase angles are shown for the corresponding dates of observation.

### Synchrone analysis

As the comet moved in the field of view of C3 the structure of its tail progressively changed. In Fig. 3.6 one can see that the fine rays gradually appear. This gives evidence that during the period of observations the dust emission was varying. This indicates that the observed brightness change is not only caused by the phase effect. As we are interested in the phase effect we must estimate how the production rate changes affect the brightness of the comet. To study the time dynamics of the dust emissions we use the method of syndyne-synchrone analysis.

This analysis goes back to works of Bessel (1835) and Bredikhin (1900). It is based on the analytical calculation of the motion of the cometary dust grains in the gravitation field of the Sun under its radiation pressure.

Finson and Probst (1968) developed a simple formalism which we shall use in our work. The strength of the radiation pressure is often measured by the ratio of the radiation force to that of gravity

$$\beta = F_{rad}/F_{grav}. \quad (3.4)$$

The radiation force is proportional to the solar intensity and the the cross-sectional area of the particle. Assuming spherical shape of the particle with diameter  $d$

$$F_{rad} = \frac{Q_{pr}}{c} \left( \frac{E_s}{4\pi r^2} \right) \frac{\pi d^2}{4}. \quad (3.5)$$

Here  $E_s$  is the mean total solar radiation ( $3.93 \times 10^{26}$  W) and  $c$  is the speed of light,  $r$  is heliocentric distance. Parameter  $Q_{pr}$  is the radiation pressure efficiency of the particle. It is connected with the particle physical properties such as size, shape and optical constants. For cometary dust it is usually taken of the order of unity. Note that  $Q_{pr}$  does not participate in the calculations directly. It becomes important when reducing the derived values of  $\beta$  to particle size.

The gravity force is proportional to the mass of the particle with density  $\rho$

$$F_{grav} = \frac{GM_{\odot}}{r^2} \left( \frac{\rho \pi d^3}{6} \right), \quad (3.6)$$

where  $G$  is the universal gravitational constant and  $M_{\odot}$  is the solar mass.

Finally

$$\beta = C(\rho d)^{-1}, \quad (3.7)$$

where

$$C = \frac{3Q_{pr}E_s}{8\pi cGM_{\odot}} = 1.19 \times 10^{-4} Q_{pr} \text{ g cm}^{-2}.$$

Both forces depend on the distance from the Sun like  $r^{-2}$ . The force of the radiation pressure is directed radially outward. Hence, in order to determine the trajectories of particles one can solve the equation of motion for the resulting force, which is the difference between gravity and radiation pressure. In this way for a given moment of time one can calculate the distribution of particles in a cometary tail with different emission times expressed in the number of days before observation  $\tau$  and different values of  $\beta$ . Usually two kinds of trajectories are distinguished, syndynes and synchrones. A *syndyne* is the locus of all particles with the same values of  $\beta$  emitted continuously with zero relative velocity

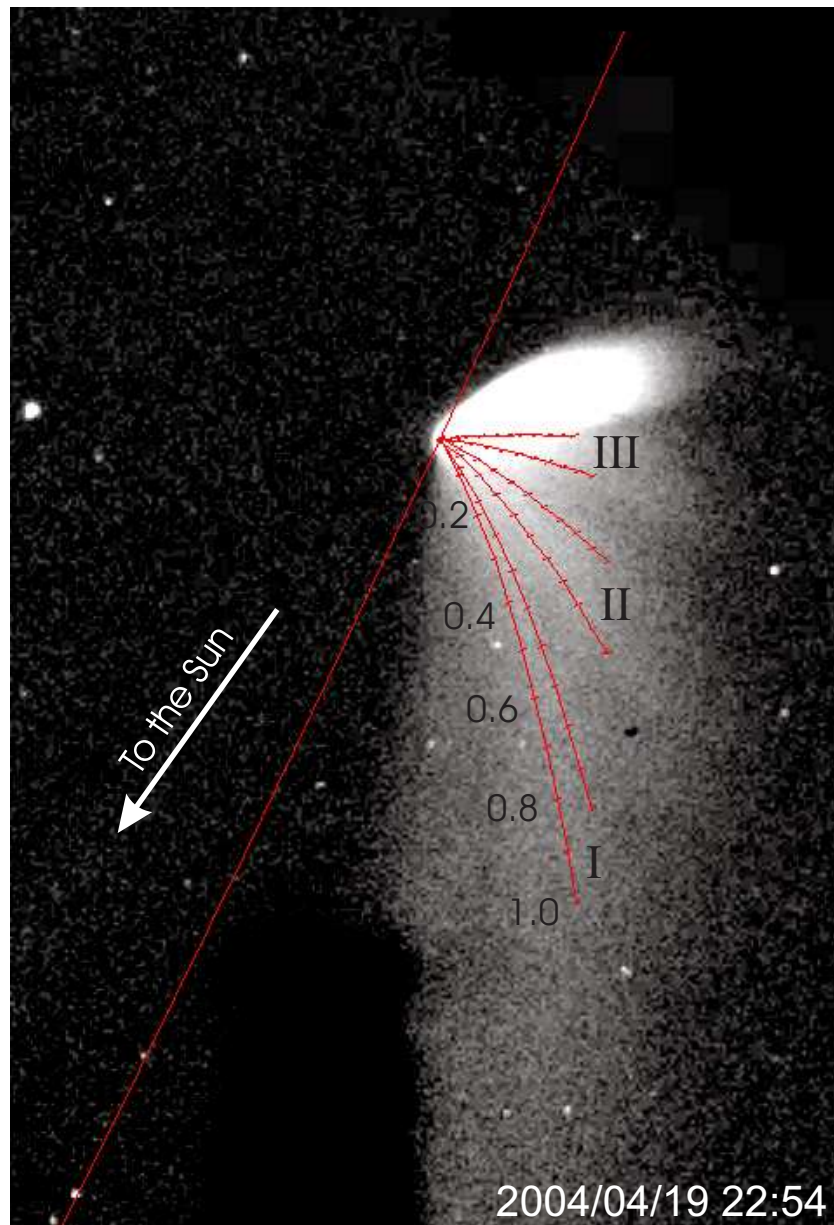


Figure 3.15: Computed synchrones superposed on the image of the C/2004 F4 Bradfield tail. The numbers show values of  $\beta$ . Roman numerals correspond to three emission periods: particles are ejected 3.9-4.1 (I), 3.2-3.5 (II) and 2.5-2.8 (III) days from the moment of observation.

from the nucleus; and a *synchrone*, is the locus of particles emitted at the same time  $\tau$ . Note that particles with  $\beta > 1$  experience a repulsive force.

As a final step the calculated heliocentric coordinates of particles must be transformed into geocentric equatorial coordinates in order to project the result of simulation in the picture plane and superimpose it with the actual image of the cometary tail.

Using orbital elements of comet C/2004 F4 we calculated synchrones for one of the last images taken before the comet left the field of view of C3 telescope. At the beginning of observations the comet had long narrow tail which progressively broadened and ac-

quired more complicated structure (Fig. 3.6). So the last images contain the record of the comet's activity during the observations. Fine ejection features, standing out against the less bright background caused by continuous emissions of dust, evolved then into three broad ones by the end of observational period. In Fig. 3.15 we present the calculated synchrones which match best to the observed structure of the tail. The numbers in Fig. 3.15 shown on one side of the synchrones indicate the corresponding values of  $\beta$ . Roman numerals correspond to three emission periods: 3.9-4.1 (I), 3.2-3.5 (II) and 2.5-2.8 (III) days back from the moment of observation.

Emission I occurred before the start of our observations. Note that the time of emission II exactly corresponds to the local maximum of brightness seen on the light curve. During the emission III approximately the same quantity of dust was ejected. Hence emission III can give a noticeable contribution to the brightness in addition to the phase dependence of the light scattering and partly cause the unexpected brightness increase. Unfortunately almost all images of the comet taken at that time appeared to be overexposed. It is interesting to note that these discontinuous emissions have periodic nature. The periods of emissions and intervals between them are approximately equal. This can possibly be explained by the presence of an active region on the surface of the rotating nucleus, which gets heated and becomes active being periodically illuminated in daytime. In this case the synodic rotation period of the comet would be  $\approx 0.7$  day. If it is the case, one could expect that other outbursts occurred later on, after emission III. Later emission maxima, which could be attributed to the nucleus rotation, cannot be distinguished in the bright glare of the dust tail in Fig. 3.15.

Parameter  $\beta$  continuously varies from nearly zero to greater than 1.5, which means that the ejected particles have broad size distribution. High  $\beta$  particles leave the window in which we measure brightness very quickly, at the same time larger particles with  $\beta < 0.1$  are accumulated in the area close to the nucleus. This concerns the broad synchrones as well as the less bright dust background. Note that for the particles of the background, which are continuously emitted,  $\beta_{max}$  is somewhat smaller than that for the particles ejected during outbursts. This can indicate different particle properties of the particles emitted during outbursts as compared to the continuously emitted particles.

As we mentioned above the radiation pressure efficiency  $Q_{pr}$  depends on many factors. To make a definite reduction of parameter  $\beta$  to the size of particles a priori information about the density and scattering properties is needed. But we can make some general conclusions. Using of Mie theory Burns et al. (1979) considered the variations of the relative radiation force  $\beta$  for a set of materials. Examples of dielectrics, conductors, opaque and transparent particles were investigated. The presented results show that only for graphite or conducting particles with sizes less than  $1 \mu\text{m}$  the radiation pressure can exceed the attraction of gravity (see also Mukai and Mukai (1973)). In addition to graphite, glassy carbon grains also have  $\beta_{max}$  exceeding unity (Kimura et al. 1997). The reason is that metals strongly backscatter incident radiation and graphite has a large imaginary part of the refractive index, i.e. high absorption. Therefore the observed large values of  $\beta$  can be an evidence for submicron-sized carbon or metal-rich grains. For all kinds of materials the condition of the low value of  $\beta < 0.1$  is a large particle size. The size must be larger than at least several microns and most probably be of the order of  $10 \mu\text{m}$ . We cannot say anything about the material in this case.

In the subsequent calculations of  $\beta$  particles with more complicated structure like

irregular compact and fluffy aggregates with different porosity rates were considered using Discrete Dipole Approximation (DDA) method (e.g. Mukai et al. (1992), Kimura et al. (2002)). Comparison of the Mie theory combined with Maxwell-Garnett effective medium theory shows good agreement with DDA results when dust aggregates have compact structure and/or the constituent grains consist of absorbing materials. In general, porosity can significantly reduce the  $\beta$  ratio for a particle. This does not influence the above conclusions, since even if the absorbing particles with  $\beta > 1.0$  are porous they must be still in the sub-micron size domain.

There is one more type of particles, a possible candidate to cometary dust, which is characterized by high radiation pressure. Theoretical calculations for a model of compact grains with a silicate core and an organic refractory mantle show  $\beta_{max} \approx 2.5$  (Mann and Kimura 2001). But their presence in the tail of C/2004 F4 is doubtful because any organic component quickly sublimates at heliocentric distances of 0.17 AU (Mukai and Schwehm 1981)

### Phase function

The observed phase function of comet C/2004 F4 consists of two branches, one when the phase angle increased to its maximum, and the other, when it decreased again. Two phase curves can be plotted respectively. In the first case the comet passes its perihelion and heliocentric distance  $r$  varies very little between 0.168 and 0.174 AU, which can hardly influence on the phase dependence.

During the second period  $r$  changes in a wider range, it grows from 0.174 to 0.215 AU, which requires correction. For this purpose we used the law of the heliocentric distance dependence derived from ground based observations made by amateur astronomers. They observed the comet since its first appearance in the morning sky after it left C3's field of view until June. In this period the phase angle  $\alpha$  changed from  $110^\circ$  to  $30^\circ$ . In this range the phase dependence of light scattering by irregular dust-like particles is weak and the particle scattering indicatrix is close to isotropic. Therefore the main cause of the further brightness decrease was the decrease in activity caused by increasing heliocentric distance. The light curve derived from these observations can be well represented by the formula (Kammerer 2004)

$$m = 8.1^m + 5 \log \Delta + 7.7 \log r. \quad (3.8)$$

Extrapolating this law to the period of the SOHO observations we can take into account the effects of changing heliocentric and geocentric distances.  $\Delta$  is also included in this approximation, although the geocentric distance of the comet was nearly constant at that time. Besides, a correction for the changing geocentric distance may not be appropriate because the comet is much larger than the diaphragm of  $3 \times 3$  pixels around the nucleus used for the brightness determination.

In Fig. 3.16 the two branches of the phase curves are presented for the four different filters. The error bars are smaller or comparable to the size of plotting symbols, so we do not show them in other figures. On the curves corresponding to growing phase angle a local maximum of brightness is present. Its range of phase angles ( $138^\circ - 144^\circ$ ) exactly corresponds to the dates of the beginning and the end of emission II. The maximum is more pronounced for the blue filter. Later the comet returns to the regular dust production

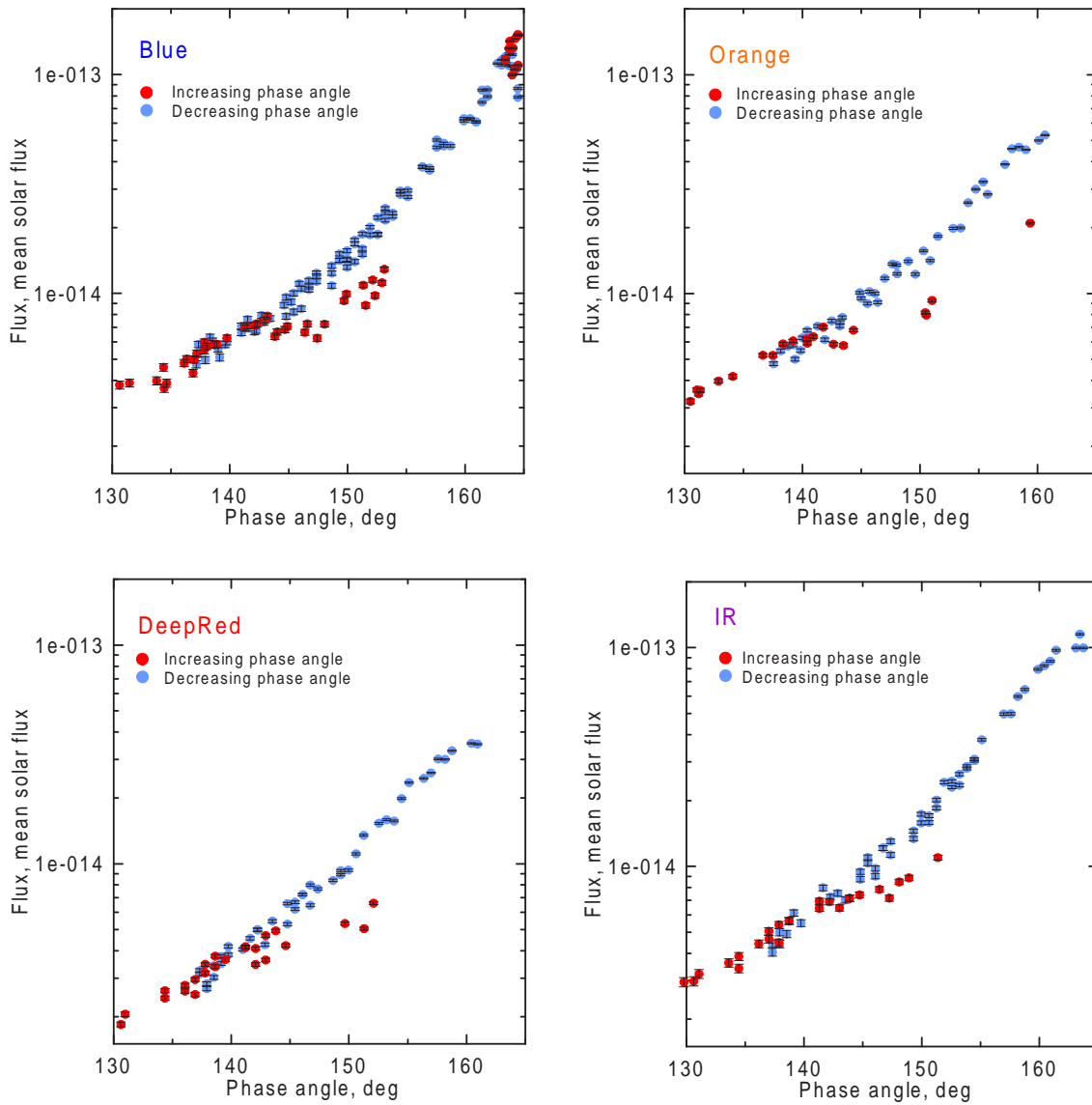


Figure 3.16: Phase curves for comet C/2004 F4 Bradfield for corresponding color filters. Red and blue dots represent the periods before and after the comet reached maximum phase angle.

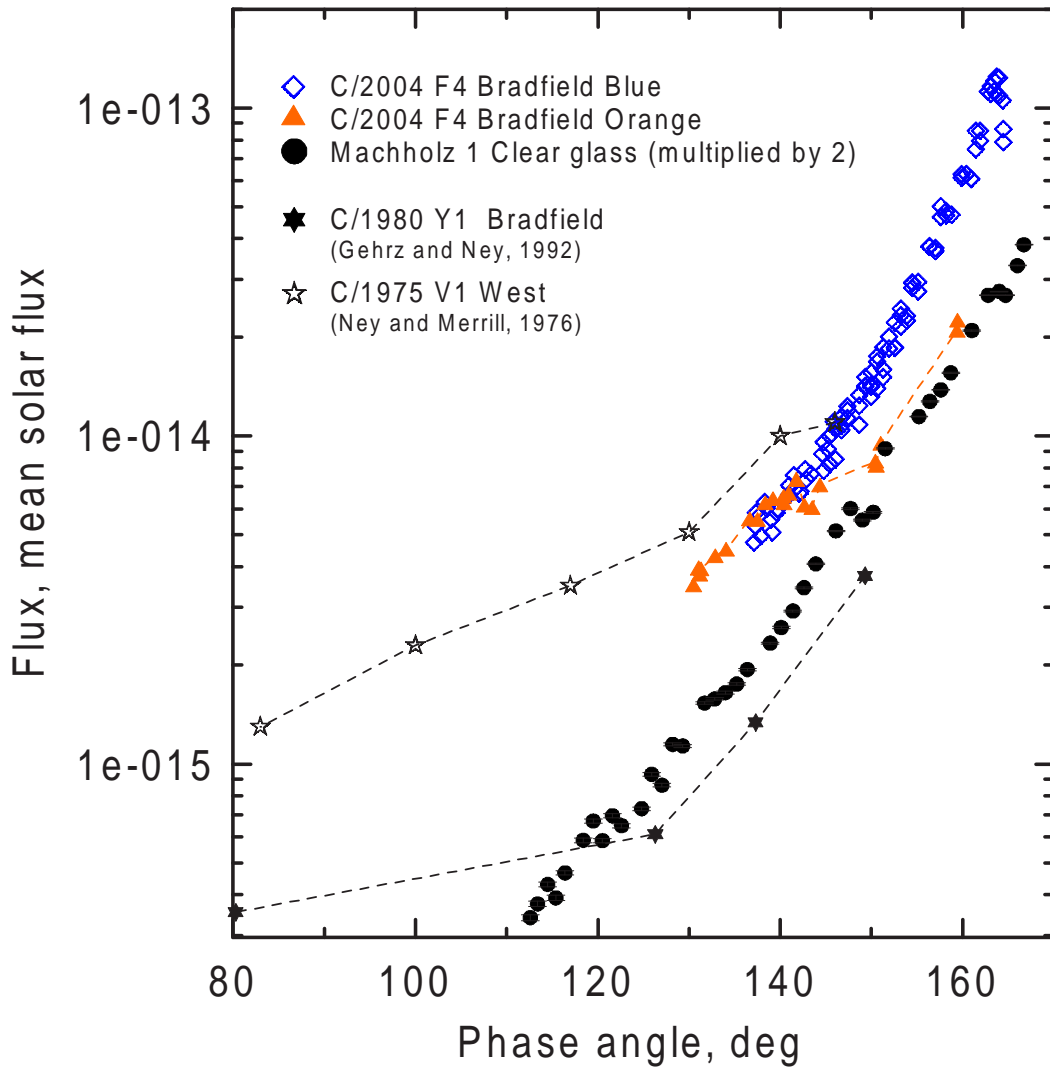


Figure 3.17: Phase curves for comets C/2004 F4 Bradfield (orange filter before, and blue filter after maximum brightness), Machholz 1, C/1980 Y1 Bradfield, and C/1975 V1 West. The values of comets C/2004 F4 and C/1975 V1 have been adjusted by multiplication with a constant to fit our measurements.

regime, although the population of dust particles in the coma may have changed. So emission II produced noticeable contribution to the brightness but did not change the general trend of the phase function dramatically. Then we have a data gap. Only observations with the orange filter show that the brightness was increasing in a normal way at least till  $\alpha = 160^\circ$ . After the maximum phase angle the brightness gradually dropped to the initial value with a gradient slightly larger than that of comet 96/P Machholz 1 (Fig. 3.17). At moderate phase angles the gradient becomes smaller, however, this branch of the phase curve remains to be different from the first one. Unfortunately there are no C3 data on comet C/2004 F4 for  $110^\circ < \alpha < 130^\circ$ , which would be helpful for a direct comparison with comet 96/P. In this phase angle range comet C/1975 V1 West, a long-period comet similar to C/2004 F4, showed a smaller brightness gradient. It is comparable to the gradient of C/2004 F4, corresponding to the increasing brightness.

If we had only observed and measured the outgoing branch of C/2004 F4, the possible conclusion would be similar to that we made for comet 96/P. But in case of C/2004 F4 the difference between the two branches of the phase curve and the synchro analysis points to the presence of qualitative and/or quantitative changes in the population of the coma. These changes are difficult to be taken into account and unambiguous interpretation is impossible. Nevertheless we will try to restrict the possible complex refractive index values using best fits to our data.

We use Mie theory again, as we did it for comet 96/P. According to the conclusion from the synchro analysis about the size range of ejected particles we take a submicron minimum and large maximum sizes: 0.1 - 50  $\mu m$ . The adopted power index is  $a = 2.5$ . Under such conditions the forward scattering lobe at  $\alpha < 164^\circ$  is formed by diffraction and forward scattering from particles comparable with the wavelength and forward scattering by larger particles. The diffraction oscillations from smaller particles are averaged over different sizes. Therefore they are smoothed out and not obvious. Only if the distribution is narrow with  $x_{max} \approx 1$  (i.e. if it is limited to sizes comparable with the wavelength) the first diffraction minimum appears at  $\alpha < 164^\circ$  and, in principle, could be detected. In addition we would get a noticeable divergence of the phase curves for the blue and IR filters at large  $\alpha$ , which is not observed for the incoming branch of the phase curve. Therefore large particles must be present and give a significant contribution to scattering. However we cannot analyze diffraction with confidence as in the first period there is a data gap at large phase angles and the second phase curve is possibly subjected to dust emissions which may influence the angular scattering effects.

Fitting the outgoing branch of the phase curve requires the real part of refractive index similar or even lower than was derived for 96/P, which is unlikely. The curves in Fig. 3.18 demonstrate this. The incoming branch of the phase dependence for C/2004 F4 is less steep than that for comet 96/P and we are less restricted with the range of possible values of the real and imaginary parts of the complex refractive index. Although the main discrete ejections of dust took place in this period of observations, we have some understanding how they can influence the phase dependence of brightness. Theoretical Mie calculations made for  $\lambda = 0.48\mu m$  (an approximate center of the blue filter bandwidth) show that equally good fits can be made with imaginary part  $0.05 \lesssim k \lesssim 0.5$ . At such a high absorption the phase curve appears to be little sensitive to  $n$ , which can be varied between 1.4 and 1.7. Lower absorption, typical for crystal silicates, leads to a big discrepancy at very large phase angles (Fig. 3.19a). Lower real part of the refractive index can improve the agreement, but the nonlinear behavior of the observational curve cannot be reproduced well enough.

Note also that for opaque particles Mie theory appears to be more correct, than for transparent ones. In Fig. 3.20 we compare the phase curve calculated with Mie theory for the full range of sizes and the phase curve calculated with Mie theory (for  $x < 50$ ) combined with our GO model (for  $x > 50$ ). In the GO case irregular RGF particles were used. The curves are in a good agreement. The explanation is that for opaque particles only the rays reflected from the particle surface can scatter. All the rays inside a particle are absorbed due to high absorption. The shape of a particle does not play role in this case. The figure shows also that absorbing particles larger than the wavelength produce less steep phase dependence than smaller ones.

A set of points at  $\alpha \approx 164^\circ$  in Fig. 3.19 are more than two times higher than the

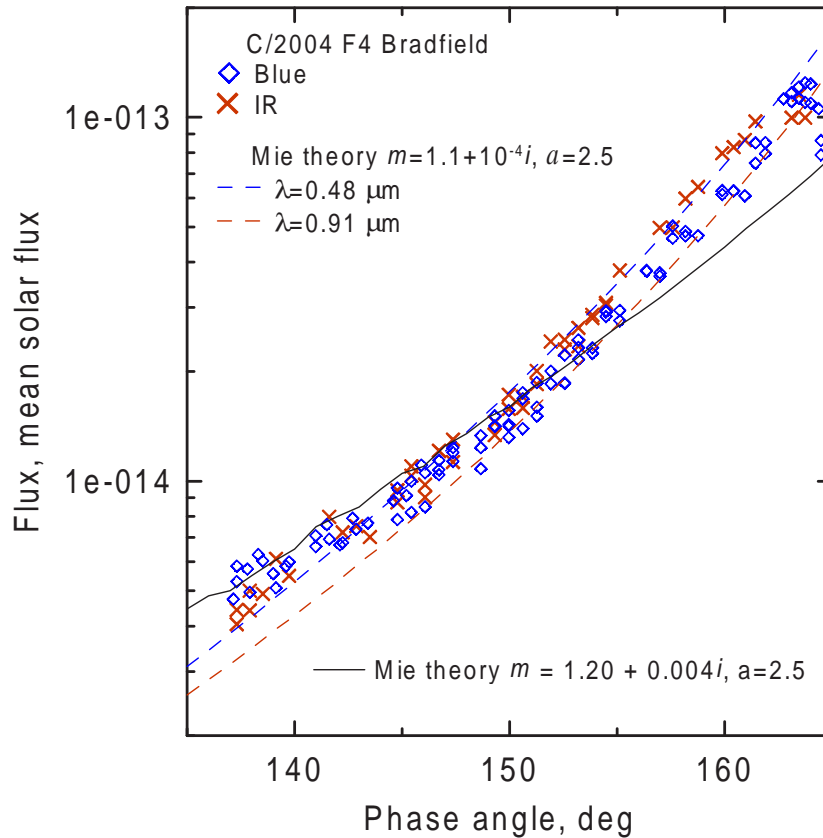


Figure 3.18: Theoretical best fit curves for the phase function branch of decreasing phase angle of comet C/2004 F4 ( $m = 1.1 + i10^{-4}$ ) and best fit for comet 96/P ( $m = 1.2 + i0.004$ ).

prediction of the theoretical fit curve. It is likely that the reason is a dust outburst, which could be related to the very bright young dust tail (Fig. 3.15). But this hypothetical outburst must have been quite strong. Nevertheless, such events are possible. Biesecker et al. (2002) reported about an outburst of comet 2P/Encke, which was observed with the LASCO telescopes near perihelion at heliocentric distance  $r \approx 0.36$  AU and at phase angles  $2^\circ \lesssim \alpha \lesssim 25^\circ$ . The almost constant lightcurve of this comet reveals a sudden increase of brightness 4.9 days after perihelion. At that moment the brightness increased by 1.5 mag in a few hours. The authors explain this by the presence of an active region with blown-off mantle on the surface of the nucleus of 2P/Encke. Comet 2P/Encke, however, is the most processed comet known, and in this respect strongly differs from young comet C/2004 F4. At the branch of decreasing brightness the phase dependence of C/2004 F4 gets much steeper. This may be caused by a decrease of the amount of particles freshly ejected during the outburst, which progressively escape from the window where we measure brightness. Another possible reason, for the high gradient, is the following. One can assume the presence of a fraction of transparent particles with real part of the refractive index smaller than 1.5. This fraction could have quickly increased during the short outburst and make the coma of C/2004 F4 more forward scattering, similar to that of comet 96/P.

Among the absorbing materials corresponding to the obtained refractive indices are

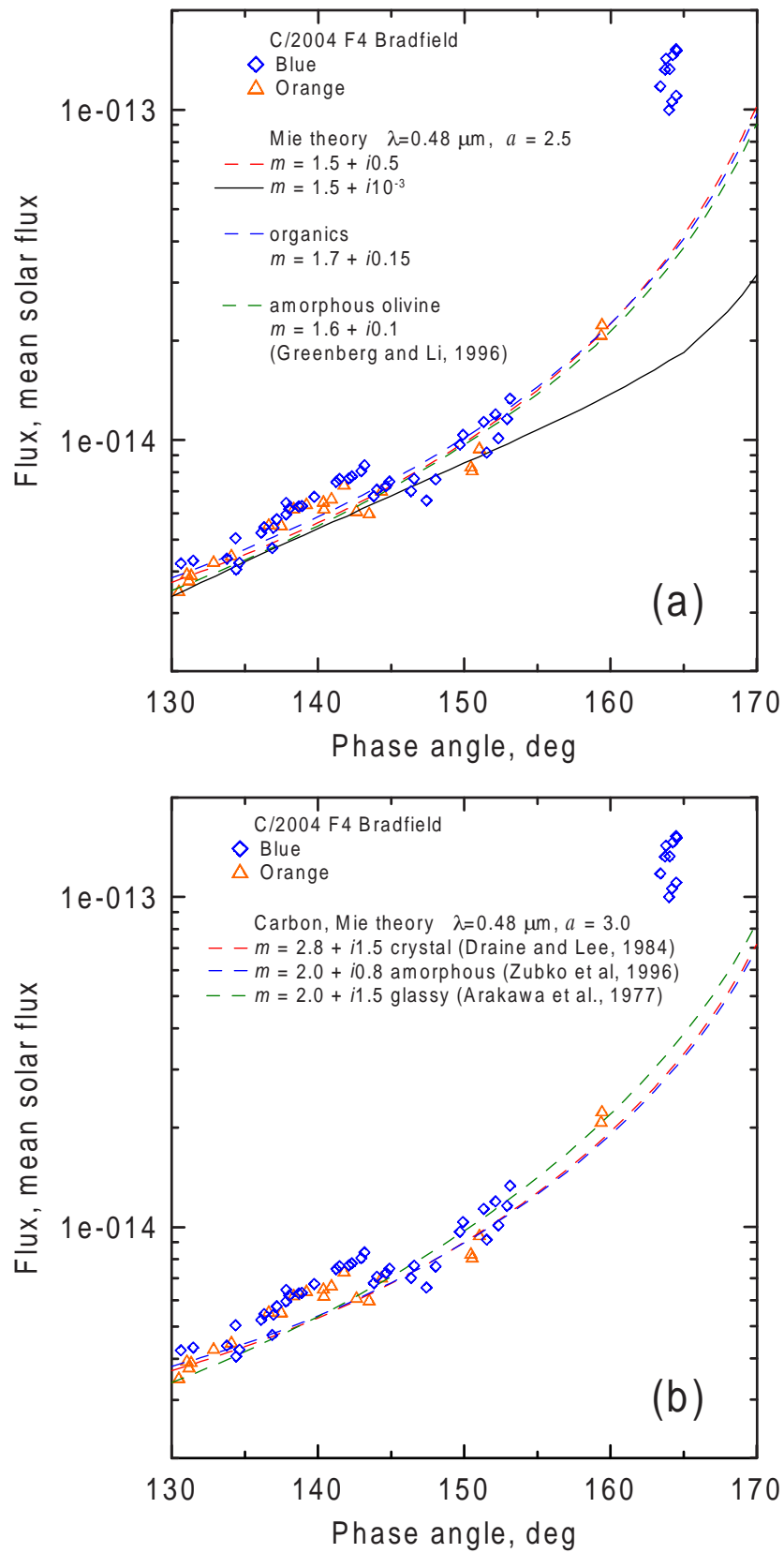


Figure 3.19: Theoretical best fit curves for blue and orange filter measurements. Mie calculations are made for two values of power index of the size distribution law  $a = 2.5$  (a) and  $a = 3.0$  (b). Measured points belong to the branch of rising brightness.

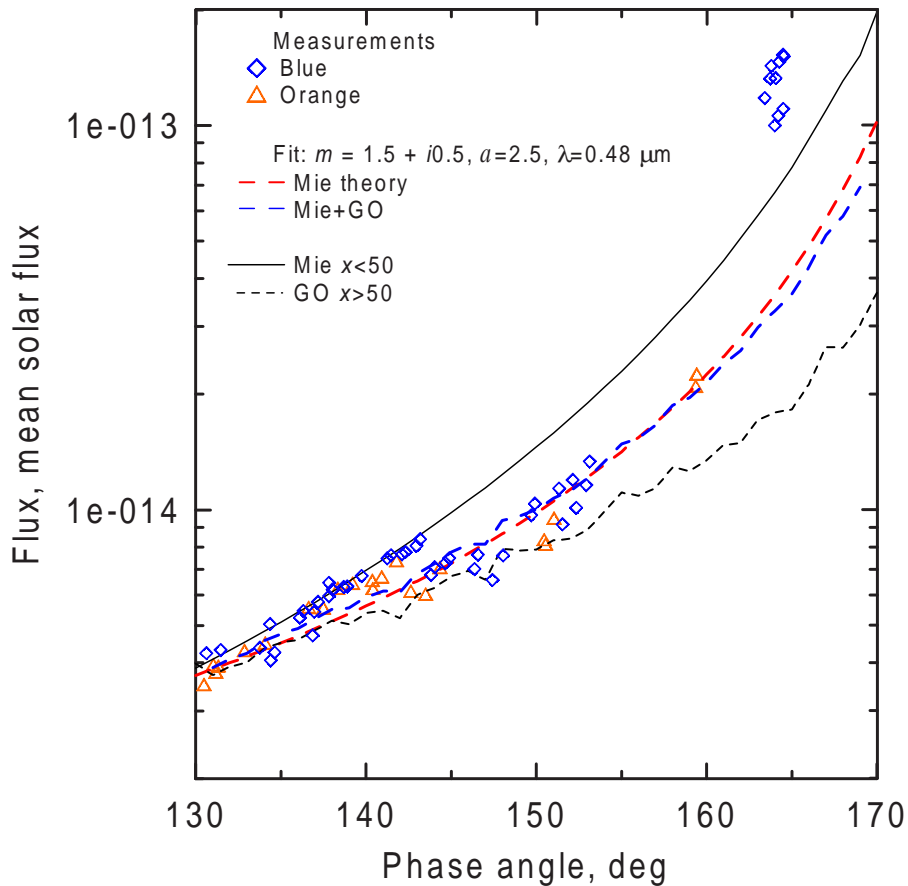


Figure 3.20: Comparison of a pure Mie theory phase curve and the combination of Mie theory with geometric optics. GO calculations were made for irregular RGF particles.

organic refractories and absorbing silicates like amorphous olivine (Greenberg and Li 1996). The existence of organics at such small heliocentric distances is doubtful. Ney and Merrill (1976) presented the phase function of comet C/1975 V1 West together with its energy distribution at wavelengths from 0.5 to 20  $\mu m$ . The brightness gradient of this comet is similar to that of C/2004 F4 (Fig. 3.17) and its spectrum reveals the silicate feature at  $\lambda = 10 \mu m$ , which is an evidence for small silicate grains.

We discussed before the possible presence of carbon-rich grains. Almost all kinds of carbon materials have real and imaginary parts of refractive index higher than those of our best fits. Only pure polycrystalline graphite has  $m = 1.7 + i0.1$  at  $\lambda = 0.48$  (Papoular et al. 1993). To reconcile this high value with the values obtained in our fits, one can either assume non-zero porosity of particles, which makes them more forward scattering, or take higher power index of the size distribution. Indeed, if we assume, for example,  $a = 3.0$ , then the measured curve can be fitted well with refractive indices characteristic for many carbonaceous materials. In Fig. 3.19b we demonstrate the fits calculated for graphite, amorphous and glassy carbon. Their refractive indices are taken from Draine and Lee (1984), Zubko et al. (1996), Arakawa et al. (1977), respectively.

Unlike for Machholz 1 here we have a lot of data for all color filters, which allows to investigate the connection between the population of particles and dependence of the phase function on the wavelength. In Fig. 3.21a there is no or weak wavelength depen-

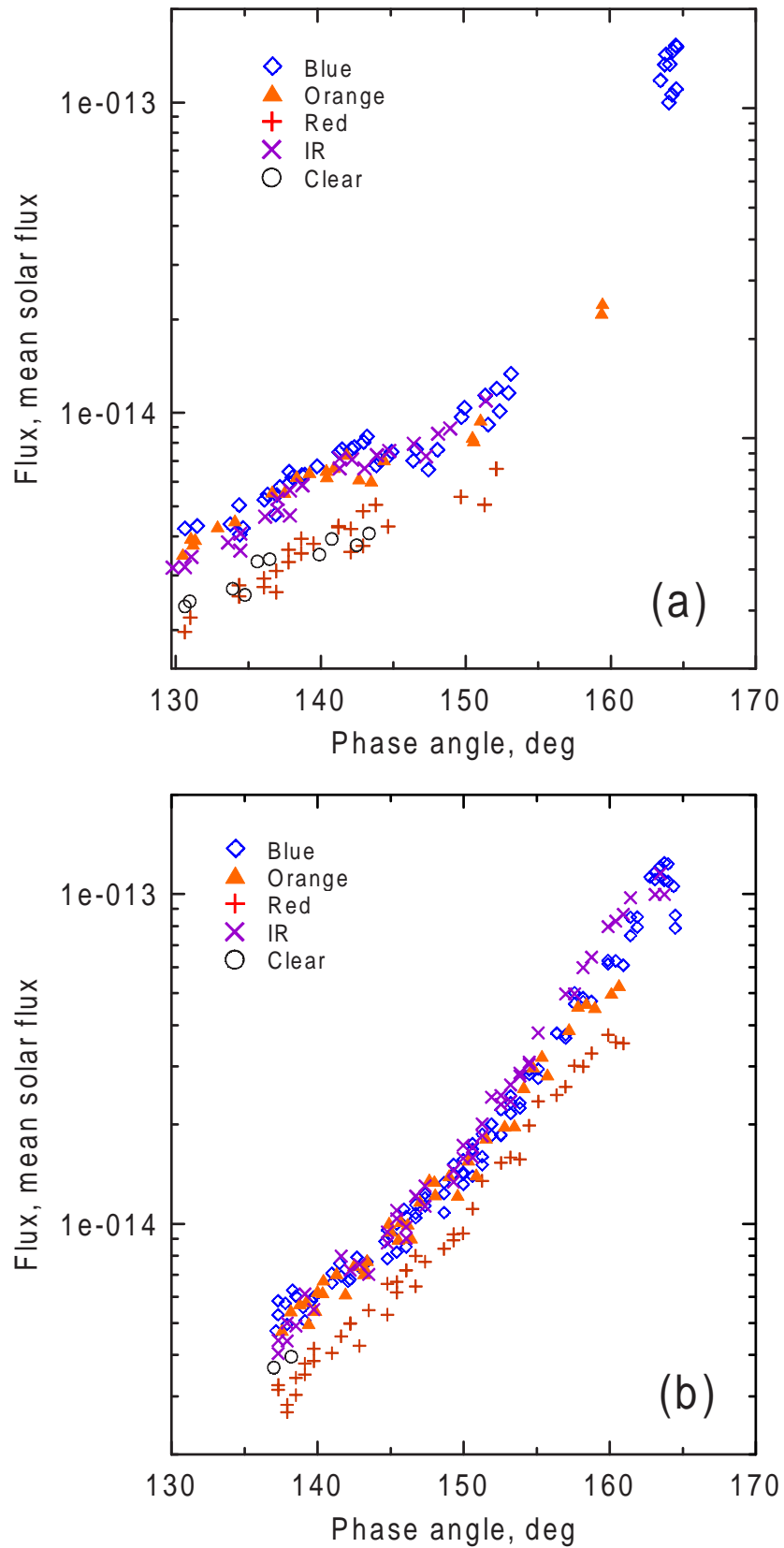


Figure 3.21: Comparison of phase curves for comet C/2004 F4 Bradfield for five filters.

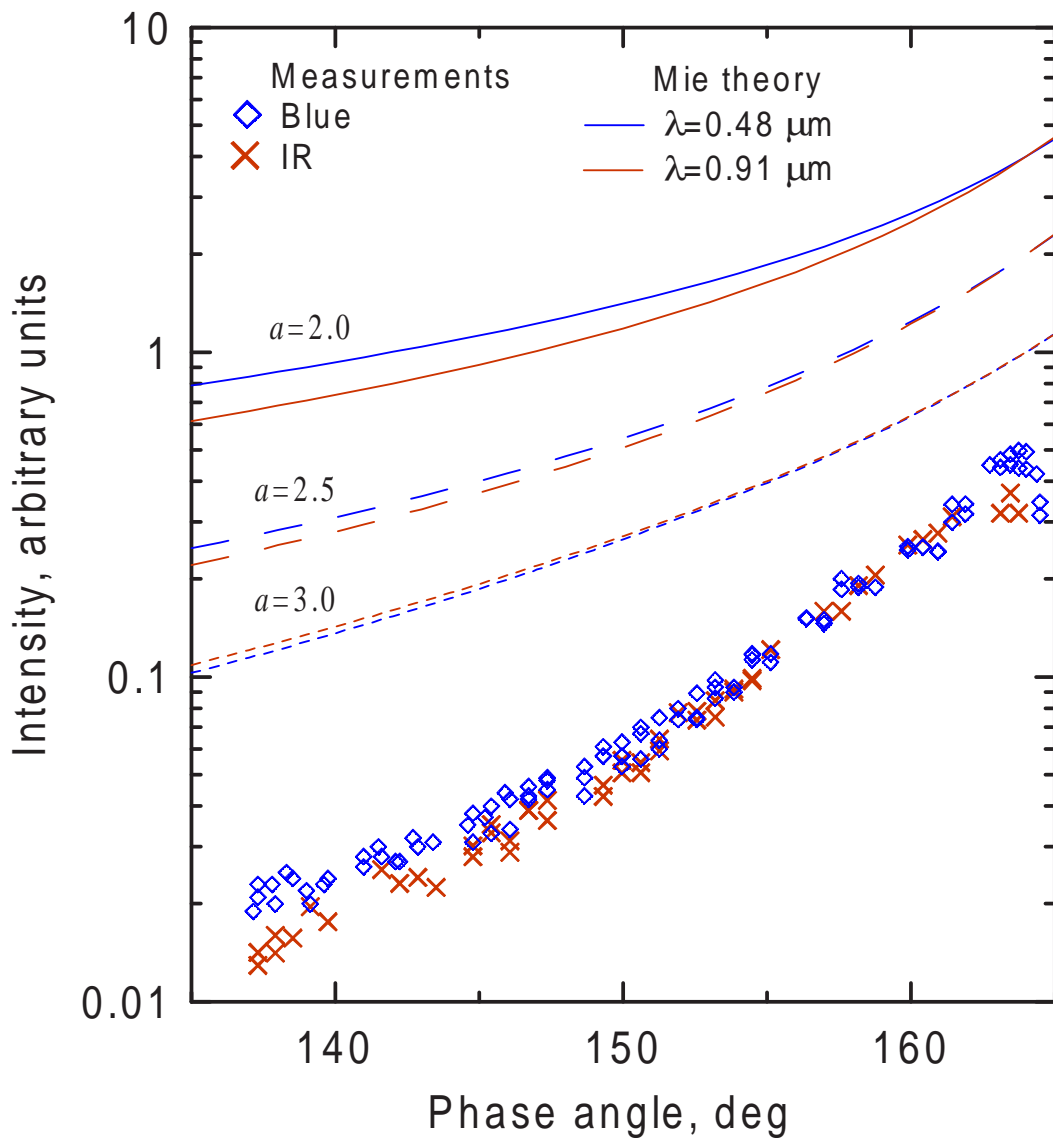


Figure 3.22: Qualitative illustration of the wavelength dependence of the phase functions at different power indices  $a$  of the size distribution. Mie calculations were made for size  $0.1\text{--}50\ \mu\text{m}$  at  $m = 1.5 + i0.5$ . Measurements of C/2004 F4 Bradfield with blue and IR filters are given for comparison and refer to the branch of decreasing phase angle. All the curves are normalized at  $164^\circ$  and multiplied by arbitrary factors.

dence of the brightness gradient before C/2004 F4 passed maximum phase angle. After that the gradient for blue (filter band centered approximately at  $0.48\ \mu\text{m}$ ) and IR (centered at  $0.91\ \mu\text{m}$ ) filter curves became noticeably different (Fig. 3.21b). The effect can be easily reproduced with numerical calculations, which show that for a given range of refractive indices particles larger than the wavelength are responsible for this phenomenon. Therefore, we can assume that the fraction of large particles increased during the observations. This is also indirectly confirmed by the synchro analysis. This increase can be expressed as a decrease of the power index  $a$  of the size distribution law. A qualitative illustration of this is presented in Fig. 3.22. Thus, according to our measurements, as a result of the dust

emission activity the power index was decreasing during the observations in the range between approximately 3.0 and 2.0.

### 3.5 Conclusions

From measurements of brightness and polarization of comet 96P/Machholz 1 photographed with the SOHO-LASCO C3 coronagraph at phase angles up to  $167^\circ$  and  $157^\circ$ , respectively, we found the following:

The accuracy of the polarization measurements proved to be low. In general the polarization data follow the phase law  $P(\alpha) = 31.72 \sin(\alpha)^{0.815} \cos(\alpha/2)^{0.408} \sin(\alpha - 21.2^\circ)$  characteristic of a typical dusty comet, derived from measurements of polarization at smaller phase angles.

The brightness increases linearly by almost two orders of magnitude in the given range of phase angles. The gradient is independent of wavelength.

The forward scattering diffraction spike is absent on the phase curve. Therefore we conclude that the contributing grains must have a size parameter larger than  $x \approx 20$ , i. e. have a radius larger than  $1 \mu\text{m}$ . The best fit refractive index of the data is  $m = 1.2 + i0.004$  according to Mie calculations of particles having a power law distribution of power index  $\approx 2.5$ . On the assumption of a particle porosity  $P = 0.5$  application of the mixing rules gives a complex refractive index of particles  $m = 1.43 + i0.009$ . At lower porosity particles must either be very transparent or have an unrealistically low real part of the refractive index.

The brightness of comet C/2004 F4 Bradfield was measured in the range of phase angles  $130^\circ - 164^\circ.5$ . During the decrease of the phase angle from  $164^\circ.5$  to  $135^\circ$  the brightness changed by a factor of 30. The synchro analysis revealed a broad distribution of the particle sizes with a large number of sub-micron particles and a ratio of radiation pressure to gravity  $\beta$  exceeding unity, which quickly escaped from the near nucleus region. These particles probably are highly absorbing carbon-rich grains and they are ejected during both regular and discontinuous dust emissions. The emissions noticeably influenced the brightness phase curve and produced a difference between the branches of the curve corresponding to the growing and decreasing phase angle. The direct reasons of such a difference can be a strongly variable amount of dust particles in the coma and a qualitative change of the dust population. A fraction of transparent particles may be emitted during the outbursts as well a fraction of absorbing ones. These changes are difficult to quantify, therefore an unambiguous interpretation is impossible. The gradient of the brightness decrease points to the similarity of the dust of the comet C/2004 F4 Bradfield to that of 96P. On the other hand theoretical fitting of the phase curve corresponding to the growing phase angle gives the complex refractive index of the dust particles corresponding to absorbing silicates (e.g. amorphous olivine) or carbonaceous materials.

The outbursts that the comet experienced when it passed around the Sun led to the change of the size distribution of particles in its coma. The power index  $a$  of the distribution law decreased from approximately 3.0 to 2.0.

# Outlook

We presented in this work the results of the LASCO C3 photometric observations of comets 96P/Machholz 1 and Bradfield C/2004 F4 at large phase angles and general theoretical study of light scattering by cometary dust particles with sizes large as compared to the wavelength of light.

We developed a computer ray tracing model, which allows calculation of the full scattering matrix  $F_{ik}$  for semitransparent particles with arbitrary shape. The studies of several classes of shape, including a special class of irregular particles generated with an auxiliary random gaussian field (RGF) lead to the following results:

- The scattering properties of faceted spheres with number of the facets less than 10000 differ significantly from those of perfectly spherical particles. The scattering angle dependences of all studied parameters, the element  $F_{11}$  and ratios  $-F_{12}/F_{11}$ ,  $F_{22}/F_{11}$ ,  $F_{33}/F_{11}$ ,  $F_{34}/F_{11}$ ,  $F_{44}/F_{11}$  of roughly faceted spherical particles, e.g., with  $N = 100$ , diverge very much from those of perfect sphere. The optical properties of individual spheres strongly dominate the scattering characteristics of binary touching spheres. Unlike binary spheres, ellipsoids reveal more deviations in scattering properties as compared to spheres.
- The ideal cube gives forward and backward scattering brightness spikes as well as a strong negative polarization branch at large scattering angles. When the cubes are deformed the spikes are reduced and become wider. The negative polarization branch vanishes.
- Highly irregular random gaussian field particles do not reveal backscattering at all, if only incoherent scattering is taken into account. As the degree of non-sphericity grows the maximum of the polarization curve decreases. The RGF particles are able to provide strong depolarization.
- For all classes of particles the degree of positive polarization ( $-F_{12}/F_{11}$ ) grows, if  $k$  increases, which is a manifestation of the Umov effect.
- In general, strongly irregular particles of all studied classes reveal a qualitative similarity of the dependence of all scattering matrix elements on scattering angle. Their scattering properties are similar in contrast to those of their perfect representatives.

During the observations of comet 96P/Machholz its brightness increases linearly by almost two orders of magnitude in the range of phase angles  $112^\circ$ - $167^\circ$ . The gradient is independent of wavelength. The forward scattering diffraction spike is absent on the phase curve, therefore the grains mainly contributing to the scattered light must have a

size parameter larger than  $x \approx 20$ , i. e. have a radius larger than  $1 \mu\text{m}$ . The best fit refractive index of the data is  $m = 1.2 + i0.004$ . If a particle porosity  $P = 0.5$  is assumed and the mixing rules are applied a complex refractive index of particles  $m = 1.43 + i0.009$  is obtained.

The brightness of comet C/2004 F4 Bradfield was measured in the range of phase angles  $130^\circ$ - $164^\circ$ .5. The synchro analysis reveals a broad size distribution of the particle sizes with a large number of sub-micron particles, which are likely to be highly absorbing carbon-rich grains. The size distribution of particles in the coma varies during the observations. The emissions noticeably influenced the brightness phase curve and led to a difference between the branches of the curve corresponding to the growing and decreasing phase angle. This made unambiguous interpretation impossible. The gradient of the brightness decrease points to the similarity of the dust of the comet C/2004 F4 to that of 96/P. On the other hand theoretical fitting of the phase curve corresponding to the increasing brightness gives the complex refractive index values of the dust particles typical for absorbing silicates (e.g. amorphous olivine) or carbonaceous materials.

# Bibliography

- A'Hearn, M. F., Millis, R. L., Schleicher, D. G., Osip, D. J., Birch, P. V., 1995, The ensemble properties of comets: Results from narrowband photometry of 85 comets, 1976-1992, *Icarus*, 118, 223-270
- Arakawa, E. T., Williams, M. W., Inagaki, T., 1977, Optical properties of arc-evaporated carbon films between 0.6 and 3.8 eV, *J. Appl. Phys.*, 48, 3176-3177
- Asano, S., and Saito, M., 1980, Light scattering by randomly oriented spheroidal particles, *Appl. Opt.*, 19, 962-974
- Bessel, F.W., 1835, *A.N.*, 13, 186
- Biesecker, D. A., Lamy, P., St. Cyr, O. C., Llebaria, A., Howard, R. A., 2002, Sungrazing comets discovered with the SOHO/LASCO coronagraphs 1996-1998, *Icarus*, 157, 323-348
- Bohren, C.F., Huffman, D.R., 1983, Absorption and scattering of light by small particles, New York: Wiley
- Bonev, T., Jockers, K., 1994, H<sub>2</sub>O(+) ions in the inner plasma tail of Comet Austin 1990 V, *Icarus*, 107, 335-357
- Bonev, T., Jockers, K., Petrova, E., Delva, M., Borisov, G., Ivanova, A., 2002, The dust in comet C/1994 S4 (LINEAR) during its disintegration: narrow-band images, color maps, and dynamical models, *Icarus*, 160, 419-436
- Born, M., Wolf, E., 1964, Principles of optics, New York: Pergamon
- Brueckner, G.E., Howard, R. A., Koomen, M. J., Korendyke, C. M., Michels, D. J., Moses, J. D., Socker, D. G., Dere, K. P., Lamy, P. L., Llebaria, A., Bout, M. V., Schwenn, R., Simnett, G. M., Bedford, D. K., Eyles, C. J., 1995, The Large Angle Spectroscopic Coronagraph (LASCO), *Sol. Phys.*, 162, 357-402
- Bruggeman, D., 1935, Berechnung der verschiedenen physikalischen Konstanten von heterogenen Substanzen, *Annalen der Physik*, 24, 636-664
- Bruning, J.H., and Lo, Y.T., 1971, Multiple scattering of EM waves by spheres. Part I - multiple expansion and ray-optical solutions, *IEEE Transactions on Antennas and Propagation*, AP-19, 378-390

- Burns, J. A., Lamy, P. L., Soter, S., 1979, Radiation forces on small particles in the solar system, *Icarus*, 40, 1-48
- Cai, Q., Liou, K., 1982, Polarized light scattering by hexagonal ice crystals: theory, *Appl. Opt.*, 21, 3569-3580
- Chernova, G. P., Kiselev, N. N., Jockers, K., 1993, Polarimetric characteristics of dust particles as observed in 13 comets - Comparisons with asteroids, *Icarus*, 103, 144-158
- Cook, J.W., editor, 1994, LASCO handbook for scientific investigators, <http://lasco-www.nrl.navy.mil/handbook/hndbk.html>
- Corrigan, C. M., Zolensky, M. E., Dahl, J., Long, M., Weir, J., Sapp, C., Burkett, P., 1997, The porosity and permeability of chondritic meteorites and interplanetary dust particles, *Meteoritics&Planet. Sci.*, 32, 509-515
- Draine, B. T., and Lee, H. M., 1984, Optical properties of interstellar graphite and silicate grains, *Astrophys. J.*, 285, 89-108
- Festou M.C., Rickman, H., West, R.M., 1994, Comets. II. Models, Evolution, Origin and Outlook, *Astron. Astroph. Rev.*, 5, 37-163.
- Finson, M., Probst, R., 1968, A theory of dust comets. I. Model equations, *Astrophys. J.*, 154, 327-380
- Fulle, M., Lévassieur-Regourd, A.C., McBride, N., Hadamcik, E., 2000, In Situ Dust Measurements From within the Coma of 1P/Halley: First-Order Approximation with a Dust Dynamical Model, *Astron. J.* 119, 1968-1977
- Gehrz, R., Ney, E., 1992, 0.7- to 23-micron photometric observations of P/Halley 2986 III and six recent bright comets, *Icarus*, 100, 162-186
- Greenberg J. M., and Li A., 1996, What are the true astronomical silicates?, *Astron. Astrophys.*, 309, 258-266
- Grundy, W., Doute, S., Schmitt, B., 2000, A Monte-Carlo ray-tracing model for scattering and polarization by large particles with complex shapes, *J. Geophys. Res.*, 105(E12), 29,291-29,314
- Grynko, Ye., Stankevich, D., Shkuratov, Yu., 2001, Light scattering by large particles with random shape and applications to cometary dust and planetary regoliths, NATO Advanced Research Workshop on the Optics of Cosmic Dust, Bratislava, 22-23
- Grynko, Ye., Stankevich, D., Shkuratov, Yu., 2001, The shadowing effect for regolith-like surfaces, *Solar System Research*, 35, 444-451
- Grynko, Ye., and Yu. Shkuratov, 2002, Scattering matrix of randomly shaped transparent particles in the geometric optics approximation, *Optics and Spectrosc.*, 93, 885-893
- Grynko, Ye., and Shkuratov Yu., 2003, Scattering matrix calculated in geometric optics approximation faceted with various shapes, *J. Quant. Spectrosc. Radiat. Transfer*, 78, 319-340

- Grynko, Ye., Jockers, K., Schwenn, R., 2004, The phase curve of cometary dust: Observations of comet 96P/Machholz 1 at large phase angle with the SOHO LASCO C3 coronagraph, *Astron. Astrophys.*, 427, 755-761
- Hadamcik, E., Levasseur-Regourd A. -C., 2003, Dust coma of Comet C/1999 S4 (LINEAR): imaging polarimetry during nucleus disruption, *Icarus* 166, 188
- Hadamcik, E., and Levasseur-Regourd, A. C., 2003, Dust evolution of comet C/1995 O1 (Hale-Bopp) by imaging polarimetric observations, *Astron. Astrophys.*, 403, 757-768
- Hanner, M.S., 1981, On the detectability of icy grains in the comae of comets, *Icarus*, 47, 342-350
- Hanner, M. S., Gehrz, R. D., Harker, D. E., Hayward, T. L., Lynch, D. K., Mason, C. C., Russell, R. W., Williams, D. M., Wooden, D. H., Woodward, C. E., 1999 Thermal Emission from the Dust Coma of Comet Hale-Bopp and the Composition of the Silicate Grains, *Earth, Moon, and Planets*, 79, 247-264
- Hansen, J., E, Travis, L. D., 1974, Light scattering in planetary atmospheres, *Space Sci. Rev.*, 16, 527-610
- Hapke, B., 1981, Bidirectional reflectance spectroscopy. I. Theory. *J. Geophys. Res.*, 86 B4, 3039-3054
- Hapke, B., 1993, *Theory of reflectance and emittance spectroscopy*, Cambridge: Cambridge University Press, 450 pp.
- Hovenier, J.W., Volten, H., Munoz, O., van der Zande, W.J., Waters, L.B.F.M., 2003, *J. Quant. Spectrosc. Radiat. Transfer*, 79-80C, 741 - 755
- Van de Hulst, H. C., 1957, *Light Scattering by small Particles*, New York: Wiley
- Jacobowitz, H.J., 1971, A method for computing the transfer of solar radiation through clouds of hexagonal ice crystals. *J. Quant. Spectrosc. Radiat. Transfer*, 11, 691-695
- Jockers, K. 1997, Observations of scattered light from cometary dust and their interpretation, *Earth, Moon and Planets*, 79, 221-245
- Jockers, K., Rosenbush, V. K., Bonev, T., Credner, T., 1997, Images of polarization and colour in the inner coma of comet HaleBopp, *Earth, Moon, and Planets*, 78, 373-379
- Kammerer, A., 2004, *Schweifstern*, 107, 12-13
- Kimura, H., Ishimoto, I., Mukai, T., 1997, A study on solar dust ring formation based on fractal dust models, *Astron. Astrophys.*, 326, 263-270
- Kimura, H., Mann, I, Biesecker, D. A., Jessberger, E. K., 2002, Dust Grains in the Comae and Tails of Sungrazing Comets: Modeling of Their Mineralogical and Morphological Properties, *Icarus*, 159, 529-541

- Kimura, H., Kolokolova, L., Mann, I., 2003, Optical properties of cometary dust. Constraints from numerical studies on light scattering by aggregate particles, *Astron. Astrophys.*, 407, L5-L8
- Kimura, H., and Mann, I., 2004, Light scattering by large clusters of dipoles as an analog for cometary dust aggregates, *J. Quant. Spectrosc. Radiat. Transfer*, 89, 155-164
- Kiselev, N., Jockers, K., Rosenbush V., 2002, Comparative Study Of The Dust Polarimetric Properties In Split And Normal Comets, *Earth, Moon and Planets* 90, 167-176
- Kiselev, N., Velichko, F., 1998, Polarimetry and Photometry of Comet C/1996 B2 Hyakutake, *Icarus*, 133, 286-292
- Kiselev, N., Velichko, F., 1997, Aperture Polarimetry And Photometry Of Comet Hale-Bopp, *Earth, Moon and Planets*, 78, 347-352
- Kiselev, N., Rosenbush, V., 2004, Polarimetry of comets: progress and problems, In *Photopolarimetry in Remote Sensing* (G. Videen et al., eds.), Kluwer Academic Publishers, 411-430
- Kiselev, N., Jockers, K., Bonev, T., 2004, CCD imaging polarimetry of Comet 2P/Encke, *Icarus*, 168, 385-391
- Kolokolova, L., O., 1990, Dependence of polarization on optical and structural properties of the surface of atmosphereless bodies, *Icarus*, 84, 305-314
- Krasnopolsky, V. A., Moroz, V. I., Krysko, A. A., Tkachuk, A. Y., Moreels, G., 1987, Properties of dust in comet P/Halley measured by the Vega-2 three-channel spectrometer, *Astron. Astrophys.*, 187, 707-711
- Lamy, P., Biesecker, D. A., Groussin, O., 2003, SOHO/LASCO observation of an outburst of Comet 2P/Encke at its 2000 perihelion passage, *Icarus*, 163, 142-149
- Lellouch E., Crovisier J., Lim, T., Bockelée-Morvan, D., Leech, K., Hanner, M.S., Altieri, B., Schmitt, B., Trotta, F., Keller, H.U., 1998, Evidence for water ice and estimate of dust production rate in comet Hale-Bopp at 2.9 AU from the Sun, *Astron. Astrophys.*, 339, L9-L12
- Liou, K.N., 1980, An introduction to atmospheric radiation, New York: Academic Press
- Liou, K., Cai, Q., Barber, P., Hill, S., 1983, Scattering phase matrix comparison for randomly oriented hexagonal cylinders and spheroids, *Appl. Opt.*, 22, 1684-1687
- Liou, K., Cai, Q., Pollack, J., Cuzzi, J., 1983, Light scattering by randomly oriented cubes and parallelepipeds, *Appl. Opt.*, 22, 3001-3008
- Lumme, K., and Rahola, J., 1994, Light scattering by porous dust particles in the discrete-dipole approximation, *Astrophys. J.*, 425, 653-667
- Macke, A., Mishchenko, M., I., Muinonen, K., Carlson, B., E., 1995, Scattering of light by nonspherical particles: ray-tracing approximation versus T-matrix method, *Opt. Letters*, 20, 1934-1936

- Macke, A., Mishchenko, M., Cairns, B., 1996, The influence of inclusions on light scattering by large ice particles, *J. Geophys. Res.*, 101, 23311-23316
- Macke, A., Mueller, J., Raschke, E., 1996, Single scattering properties of atmospheric ice crystals, *J. Atm. Sci.*, 53, 2813-2825
- Mackowski D.W., 1991, Analysis of radiative scattering for multiple sphere configurations, *Proc. R. Soc.Lond. A.*, 433, 599-614
- Mann, I., and Kimura, H., 2001, Dust properties in the local interstellar medium, *Space Sci. Rev.*, 97, 389-392
- Mazets, E.P., Aptekar, R.L., Golenetskii, S. V., Guryan, Yu. A., Dyachov, A.V., Ilynskii, V.N., Panov, V.N., Petrov, G.G., Savvin, A.V., Sagneev, R.Z., Sokolov, I.A., Khavenson, N.G., Shapiro, V.D., Shevchenko, V.I., 1986, Comet Halley dust environment from SP-2 detector measurements, *Nature*, 321, 276-278
- Meech, K. J., and Jewitt, D. C., 1987, Observations of comet P/Halley at minimum phase angle, *Astron. Astrophys.*, 187, 585-593
- Melamed, N., 1963, Optical properties of powders. 1. Optical absorption coefficients and the absolute value of the diffuse reflectance, *J. Appl. Phys.*, 34, 560-570
- Mie, G., 1908, Beiträge zur Optik trüber Medien, speziell kolloidaler Metallösungen, *Ann. Phys.*, 25, 377-445
- Mishchenko, M. I., Macke, A., 1997, Asymmetry parameters of the phase function for isolated and densely packed spherical particles with multiple internal inclusions in the geometric optics limit, *J. Quant. Spectr. Radiat. Transfer*, 57, 767-794
- Mishchenko, M., Hovenier, J., Travis, L., editors, 2000, *Light scattering by non-spherical particles*, San Diego: Academic Press
- Mishchenko, M., Travis, L., Lacis, A., 2002, *Scattering, Absorption, and Emission of Light by Small Particles*, Cambridge: Cambridge Univ. Press
- Muinonen, K., Lumme, K., Peltoniemi, J., Irvine, W., 1989, Light scattering by randomly oriented crystals. *Appl. Opt.*, 28, 3051-3060
- Muinonen, K., Ray optics approximation for random clusters of Gaussian spheres. In: Verstraete M et al., editors, 2000, *Advances in Global Change Research*, vol. 4, The Netherlands: Kluwer Academic Publishers, p. 209-217.
- Muinonen, K., Stankevich, D., Shkuratov, Yu., Kaasalainen, S., Piironen, J., 2001, Shadowing effect in clusters of opaque spherical particles, *J. Quant. Spectrosc. Radiat. Transfer*, 70, 787-810
- Mukai, T., and Schwehm, G., 1981, Interaction of grains with the solar energetic particles, *Astron. Astrophys.*, 95, 373-382

- Mukai, T., and Mukai, S., 1973, Temperature and motion of the grains in Interplanetary space, *Publ. astron. Soc. Japan*, 25, 481-488
- Mukai, T., 1977, Dust grains in the cometary coma - Interpretation of the infrared continuum, *Astron. Astrophys.*, 61, 69-74
- Mukai, S., Mukai, T., Weiss, K., Zerull, R., 1982, Scattering radiation by a large particle with a random rough surface, *Moon and Planets*, 26, 197-208
- Mukai, T., Ishimoto, H., Kozasa, T., Blum, J., Greenberg, J. M., 1992, Radiation pressure forces of fluffy porous grains, *Astron. Astrophys.*, 262, 315-320
- Muñoz, O., Volten, H., de Haan, J.F., Vassen, W., Hovenier, J.W., 2000, Experimental determination of scattering matrices of olivine and Allende meteorite particles, *Astron. Astrophys.*, 360, 777-788
- Muñoz, O., Volten, H., de Haan, J.F., Vassen, W., Hovenier, J.W., 2001, Experimental determination of scattering matrices of olivine and Allende meteorite particles, *J. Geophys. Res.*, 106, 22,833-22,844
- Muñoz, O., Volten, H., de Haan, J.F., Vassen, W., Hovenier, J.W., 2002, Experimental determination of the phase function and degree of linear polarization of El Chichón and Pinatubo volcanic ashes, *J. Geophys. Res.*, 107, 10.1029/2001JD000983
- Ney, E.P., and Merrill, K.M., 1976, Comet West and the scattering function of cometary dust, *Science*, 194, 1051-1053
- Nousiainen, T., Muinonen, K., Raisanen, P., 2003, Scattering of light by large Saharan dust particles in a modified ray optics approximation, *J. Geophys. Res.*, 108, 12-1 - 12-17
- Padmavati, A. Y.-F., and Hanner, M. S., 1999, Optical properties of nonspherical particles of size comparable to the wavelength of light: application to comet dust, *Icarus*, 138, 107-128
- Papoular, R., Breton, J., Gensterblum, G., Nenner, I., Papoular, R. J., Pireaux, J.-J., 1993, The vis/UV spectrum of coals and the interstellar extinction curve, *Astron. Astrophys.*, 270, L5-L8
- Peltoniemi, J., Lumme, K., Muinonen, K., Irvine, W., 1989, Scattering of light by stochastically rough particles, *Appl. Opt.*, 28, 4088-4095
- Peltoniemi, J., 1992, Radiative transfer in stochastically inhomogeneous media, *J. Quant. Spectrosc. Radiat. Transfer*, 50, 655-671
- Petrova, E.V., Jockers, K., Kiselev, N.N., 2000, Light scattering by aggregates with sizes comparable to the wavelength: an application to cometary dust, *Icarus*, 148, 526-536
- Petrova, E.V., and Jockers, K., 2002, On the spectral dependence of intensity and polarization of light scattered by aggregated particles, In *Electromagnetic and Light Scattering by Nonspherical Particles* (B. Gustafson, L. Kolokolova, G. Videen, eds.), ARL, 263-266

- Purcell, E.M., and Pennypacker, C.R., 1973, Scattering and absorption of light by non-spherical dielectric grains, *Astrophys. J.*, 186, 705-714
- Rayleigh, L., 1871, On the light from the sky, its polarization and colour, *Philos. Mag.*, 41, 107-120, 274-279
- Renard, J.-B., Hadamcik, E., Lévassieur-Regourd, A.-C., 1996, Polarimetric CCD imaging of comet 47P/Ashbrook-Jackson and variability of polarization in the inner coma of comets, *Astron. Astrophys.*, 316, 263-269
- Rossi, A., Botti, L., Sasse, C., Tamme, R., 2004, Scattering phase function measurements on single particles and on particle ensembles functions, *Appl. Optics*, 43, 6673-6679
- Schiffer, R., and Thielheim, K., 1982, A scattering model for the zodiacal light particles, *Astron. Astrophys.*, 116, 1-9
- Sekanina, S., 1990, Periodic Comet Machholz and its idiosyncrasies, *Astron. J.*, 99, 1268-1277
- Sekanina, Z., 2002, Statistical investigation and modeling of sungrazing comets discovered with the solar and heliospheric observatory, *Astrophys. J.*, 566, 577-598
- Shkuratov, Yu.G., Stankevich, D.G., 1992, The shadow effect for planetary surfaces with Gaussian mesotopography, *Sol. Syst. Res.*, 26, 201-211
- Shkuratov, Yu.G., 1994, Light backscattering by the solid surfaces of celestial bodies: theoretical models of the opposition effect, *Sol. Syst. Res.*, 28, 418-431
- Shkuratov, Yu., L. Starukhina, H. Hoffmann, and G. Arnold, 1999, A model of spectral albedo of particulate surfaces: implication to optical properties of the Moon, *Icarus*, 137, 235-246
- Shkuratov, Yu., and Grynko, Ye., 2005, Light scattering by media composed of semi-transparent particles of different shapes in ray optics approximation: consequences for spectroscopy, photometry, and polarimetry of planetary regoliths, *Icarus*, 173, 16-28
- Stankevich, D., Shkuratov, Yu., Grynko, E., Muinonen, K., 2002, A computer simulation of multiple scattering of light rays in systems of opaque particles, *J. Quant. Spectrosc. Radiat. Transfer*, 76, 1-16
- Stankevich, D., Shkuratov, Yu., Grynko, Ye., Muinonen, K., 2003, Computer simulations for multiple scattering of light rays in systems of opaque particles, *J. Quant. Spectrosc. Radiat. Transfer*, 76, 1-16
- Steigmann, G., A., 1978, A polarimetric model for a dust covered planetary surface, *Mon. Not. Roy. Astr. Soc.*, 185, 877-888
- Takano, Y., and Jayaweera, K., 1985, Scattering phase matrix for hexagonal ice crystals computed from ray optics, *Appl. Opt.*, 24, 3254-3263

- Trowbridge, T., 1984, Rough-surface retroreflection by focusing and shadowing below a randomly undulating interface, *J. Opt. Soc. Am.*, A1(10), 1019-1027
- Volten, H., Muñoz, O., Rol, E., de Haan, J.F., Hovenier, J.W., Muinonen, K., Nousiainen, T., 2001, Scattering matrices of mineral aerosol particles at 441.6 nm and 632.8 nm, *J. Geophys. Res.*, 106, 17,375-17,402
- Voshchinnikov, N.V., 1996, Electromagnetic scattering by homogeneous and coated spheroids: calculations with the separation of variables method, *J. Quant. Spectr. Radiat. Transfer*, 55, 627-636
- Wait, J.R., 1955, Scattering of a plane wave from a circular dielectric cylinder at oblique incidence, *Can. J. Phys.*, 33, 189-195
- Waterman, P.C., 1971, Symmetry, unitarity, and geometry in electromagnetic scattering, *Phys. Rev. D.*, 3, 825-839
- Weiss-Wrana, K., 1983, Optical properties of interplanetary dust: comparison with light scattering by larger meteoritic and terrestrial grains, *Astron. Astrophys.*, 126, 240-250
- Wendling, P., Wendling, R., Weickman, K., 1979, Scattering of solar radiation by hexagonal ice crystals, *Appl. Opt.*, 18, 2663-2671
- Whalley, E., and McLaurin, G., 1984, Refraction halos in the Solar System: 1. Halos from cubic crystals that may occur in atmospheres in the Solar system, *J. Opt. Soc. Am.*, A12, 1166-1170
- Wielaard, D., J., Mishchenko, M., I., Macke, A., Carlson, B., E., 1997, Improved T-matrix computations for large nonabsorbing and weakly absorbing nonspherical particles and comparison with geometrical-optics approximation, *Appl. Optics*, 36, 4305-4313
- Wolff, M., 1975, The polarization of light reflected by rough planetary surface, *Appl. Opt.*, 14, 1395-1404
- Xing, Z., and Hanner, M. S., 1997, Light scattering by aggregate particles, *Astron. Astrophys.*, 324, 805-820
- Yanamandra-Fisher, P., and Hanner, M., 1999, Optical properties of nonspherical particles of size comparable to the wavelength of light: application to comet dust, *Icarus*, 138, 107-128
- Yang, P., Liou, K., N., 1995, Light scattering by hexagonal ice crystals: comparison of finite-difference time domain and geometric optics models, *J. Opt. Soc. Am.*, 12, 162-176
- Yang, P., Liou, K., N., 1996, Geometric-optics-integral-equation method for light scattering by nonspherical ice crystals, *Appl. Opt.*, 35, 6568-3584
- Zubko, V. G., Mennella, V., Colangeli, L., Bussoletti, E., 1996, Optical constants of cosmic carbon analogue grains - I. Simulation of clustering by a modified continuous distribution of ellipsoids, *MNRAS*, 282, 1321-1329

- Zubko, E.S., and Shkuratov, Yu.G., 2001, Simulation of polarization properties of comet Halley dust, *Meteoritics & Planet. Sci.*, 36 (Supplement), A233-A234
- Zubko, E., Shkuratov, Yu., Muinonen, K., 2001, Light scattering by composite particles comparable with wavelength and their approximation by systems of spheres, *Optics & Spectroscopy*, 91, 273-277
- Zubko, E., Shkuratov, Yu., Hart, M., Eversole, J., Videen, G., 2004, Backscatter of agglomerate particles, *J. Quant. Spectr. Radiat. Transfer*, 88, 163-171
- Zubko, E., Shkuratov, Yu., 2005, The negative polarization of light scattered by cosmic dust particles at small phase angles, *Icarus*, in press



# Acknowledgements

This thesis has been written in the Max Planck Institute for Solar System Research, Katlenburg-Lindau. I thank its directors for the possibility to study and work in the nice and creative atmosphere of the institute. Financial support of the Max Planck Society is gratefully acknowledged.

Many thanks to my supervisor in MPS, Prof. Dr. Klaus Jockers, for offering me the topics which I have been working on, for his help and discussions during my Ph.D. project. I thank my university supervisor, Prof. Dr. Ulrich Christensen, for accepting me as his Ph.D. student at the Physics Dep. of the University of Göttingen.

I am grateful to the Kharkov light scattering group and its chief Prof. Yuriy Shkuratov for invaluable help in theoretical studies of the light scattering problem. I would like to thank my office mates and colleagues Dr. Nikolai Kiselev and Dr. Tanyu Bonev for very fruitful discussions and consulting on cometary science.

I thank the whole LASCO team for making the data and software libraries used in the thesis available to me. In particular I thank Dr. Doug Biesecker and Dr. Borut Podlipnik for providing the required explanations.

I also would like to thank Dr. Dieter Schmitt, the coordinator of the International Max Planck Research School on Physical Processes in the Solar System and Beyond, for the organization of the school, a member of which I am, and taking care of all of us, students in Lindau.



# Lebenslauf

Name: Yevgen Grynko

Geburtsdatum: Juni 26, 1978

Geburtsort: Zaporozhye, Ukraine

Staatsbürgerschaft: ukrainisch

Schulbildung: 9/1985–6/1992 Grundschule N59, Zaporozhye  
9/1992–6/1995 Lyceum "Logos", Zaporozhye

Studium: 9/1995–7/2000 Physikstudium an der physikalischen  
Fakultät der Nationalen Universität Kharkiv, Ukraine  
Abteilung für Physik und Astronomie

9/1998–1/1999 Bachelorarbeit: "Computer model of a random multiple  
valued surface"

9/1999–7/2000 Diplomarbeit: "Shadowing effect in stochastic regolith-like  
media"

10/2000–2/2002 Wissenschaftlicher Mitarbeiter des Instituts  
für Astronomie der Nationalen Universität Kharkiv

2/2002–4/2005 Doktorarbeit am Max-Planck-Institut für  
Sonnensystemforschung, Katlenburg-Lindau